

**Monodisperse magnetic alloy nanocrystals  
and their superstructures**

**A dissertation  
submitted to the University of Hamburg for the degree of  
Doctor of Natural Sciences**

**Elena V. Shevchenko**

**from Korma (Belarus)**

**April 2003**

---

The work described in this thesis was carried out in the Intitute of Physical Chemistry,  
University of Hamburg in Prof. Dr. Horst Weller group.

1. Referee: Prof. Dr. Horst Weller
2. Referee:

## Acknowledgements

I want to thank my supervisor *Prof. Dr. Horst Weller* for a very interesting research topic, for providing excellent experimental facilities and for many useful discussions.

My special thank goes to *Dr. Dmitri Talapin* and *Priv.-Doz. Dr. Markus Haase* for their useful advises which helped significantly to improve my work in the lab. I would also like to acknowledge them and also *Dr. Andrey Rogach* for their help in writing and corrections of our manuscripts.

Another special thanks goes to *Sylvia Bartoldi-Nawrath* and *Dipl.-Ing. Andreas Kornowski* for excellent TEM, HRTEM and HRSEM images.

I am also very thankful to *Rosemarie Pakula* for her willingness to help us in all bureaucratic affairs.

Special appreciation goes to *Dr. Nikolai Gaponik* for interesting discussions and his help in the lab. He and *Uwe Borchert* I acknowledge for help with photography. I also thank *Holger Borchert* for the XPS investigations of my samples and useful discussions.

*Priv.-Doz. Dr. Alexander Eychmüller* is acknowledged for the literature seminars, stimulating discussions and organisation of the German language courses.

I thank *Prof. Dr. Jurgen Kötzler* and *Frank Wieckhorst* (University of Hamburg, Germany), *Prof. Dr. Peter Swendlith* and *Örjan Festin* (Uppsala University, Sweden), *Dr. Marina Spasova* (University of Duisburg, Germany) for their help in the investigation of magnetic properties. Additionally I want to thank *Dr. Marina Spasova* for the careful reading of the “Magnetic part” of my thesis. I thank *Dr. Leonid Govor* (University of Oldenburg, Germany) for the investigation of the self-assembly systems based in polymers and our magnetic nanocrystals and *Dr. Heimo Schnablegger* - for the SAXS measurements.

I thank *Frank Burli*, *Bernhard Seydak* and our glass-blowers: *Werner Gehring* and *Hilmar Zacharek* for their technical support.

I thank the *BIOAND project* for the possibility to become acquainted with a lot of beautiful European countries and meet a lot of excellent scientists. *Dr. Andrea Schroedter* and *Dr. Claudia Pacholski* are acknowledged for their inestimable contribution in the writing of all official project reports.

I am very grateful to **all my colleges from AK Weller** for the nice working atmosphere in the group. I wish you success in your further professional activity. Special thank goes to *Holger Borhert*, *Sandra Hirzberger* and *Dr. Kathrin Hoppe* for joint work in one office.

I thank my friends in Belarus and abroad who do not forget me and, of course, I thank my dear parents *Anastasia* and *Valery Shevchenko* and my husband *Dmitri Talapin* for their support, love and patience.

# Monodisperse magnetic alloy nanocrystals and their superstructures

## Content

Titel	i
Acknowledgements	iii
Content	v
Notations	vii
<b>1. Introduction</b>	<b>1</b>
<b>2. Organometallic synthesis and characterisation of monodisperse CoPt<sub>3</sub> nanocrystals</b>	<b>5</b>
2.1. Introduction	5
2.2. Synthesis of CoPt <sub>3</sub> nanocrystals	6
2.3. Structural characterisation of CoPt <sub>3</sub> nanocrystals	15
2.4. Conclusions	16
2.5. References	17
<b>3. The mechanism of nucleation and growth of CoPt<sub>3</sub> nanocrystals</b>	<b>19</b>
3.1. Introduction	19
3.2. Study of nucleation and growth of magnetic alloy nanocrystals	20
3.2.1. <i>Effect of the injection temperature and concentration of the stabilizing agent (1-adamantanecarboxylic acid)</i>	27
3.2.2. <i>Effect of the ratio between Co and Pt precursor</i>	28
3.2.3. <i>Size distribution of the CoPt<sub>3</sub> nanocrystals in growth</i>	30
3.2.4. <i>Faceting of CoPt<sub>3</sub> nanocrystals</i>	32
3.3. The role of nucleation rate in size control of CoPt <sub>3</sub> nanocrystals	34
3.4. Discussion of the nucleation mechanism	40
3.5. Temporal stability and thermostability of CoPt <sub>3</sub> nanocrystals	44
3.6. Conclusions	46
3.7. References	48
<b>4. Synthesis and characterisation of other magnetic alloy nanocrystals and phase transfer of magnetic nanocrystals into the water</b>	<b>51</b>
4.1. Introduction	51
4.2. FePt nanocrystals	52
4.2.1. <i>Oleic acid- oleyl amine approach</i>	52
4.2.2. <i>ACA-approach</i>	56
4.2.3. <i>Transfer of FePt and CoPt<sub>3</sub> nanocrystals from organic solvents into aqueous medium</i>	62
4.3. CoPd <sub>2</sub> nanocrystals	64
4.4. Conclusions	66
4.5. References	67

<b>5. Magnetic properties of CoPt<sub>3</sub> nanocrystals</b>	<b>69</b>
5.1. Introduction into magnetic properties of nanocrystals	69
5.2. Characterisation of magnetic properties of CoPt <sub>3</sub> nanocrystals	77
5.3. Conclusions	84
5.4. References	85
<b>6. Self-assembly of magnetic alloy nanocrystals</b>	<b>87</b>
6.1. Introduction	87
6.2. Formation of 2D and 3D superlattices from monodisperse magnetic nanocrystals	88
6.3. Template self-assembly of CoPt <sub>3</sub> nanocrystals	97
6.4. Colloidal crystals of the magnetic alloy nanocrystals	99
6.5. Self-assembly of magnetic nanocrystals in external magnetic fields	104
6.6. Inverse opals from FePt nanocrystals	118
6.7. Conclusions	119
6.8. References	120
<b>7. Summary</b>	<b>123</b>
<b>Experimental Section</b>	<b>125</b>
Chemicals	125
Apparatus	125
Synthesis of CoPt <sub>3</sub> nanocrystals	126
Additional injections of the precursors	127
Post-preparative procedures	127
Size histograms of different size fractions of as –prepared CoPt <sub>3</sub> nanocrystals	128
Post-preparative size selective fractionation	130
Investigation of the nucleation and growth of CoPt <sub>3</sub> nanocrystals	130
Synthesis of PtFe nanocrystal	132
Synthesis of CoPd <sub>2</sub> nanocrystals	133
Preparation of CoPt <sub>3</sub> nanocrystals – polylaurylmethacrylate composite	133
Growing the colloidal crystals of CoPt <sub>3</sub> and PtFe nanoparticles	133
References	134
<b>Safety precaution information on the used chemicals</b>	<b>135</b>
<b>CURRICULIM VITAE</b>	<b>141</b>

## Notations

ACA	Adamantanecarboxylic acid
AFM	Atomic Force Microscopy
DDA	Dodecylamine
EDX	Energy Dispersive X-ray analysis
FC	Field Cooled
H	Magnetic field strength
H <sub>c</sub>	Coercivity
HDA	Hexadecylamine
HRSEM	High Resolution Scanning Electron Microscopy
HRTEM	High Resolution Transmission Microscopy
ITO	Indium Tin Oxides
M	Magnetisation
M <sub>s</sub>	Saturation magnetisation
OA	Oleic Acid
PLMA	Polylaurylmetacrylate
SAXS	Small Angle X-Ray Scattering
SQUID	Super-Conductive Quantum Interference Device
TDPA	Tetradecylphosphonic Acid
TEM	Transmission Electron Microscopy
TEM-size	Nanoparticle size calculated by processing of the TEM images.
TOP	Tri-n-octylphosphine
TOPO	Tri-n-octylphosphine Oxide
SEM	Scanning Electron Microscopy
vol.	volume
wt.	weight
XRD	X-Ray Diffraction
XRD-size	Nanoparticle size calculated by Debye-Sherrer equation
ZFC	Zero Field Cooled



# 1. Introduction

Nanomaterials play the role of a bridge between the single elements and single crystalline bulk structures. The term “*nanocrystals*” was proposed to use for crystalline particles with a low concentration of defects of crystal lattice, while the more general term “nanoparticle” also involves particles containing gross internal grain boundaries, fractures, or internal disorder [1]. The finite size of the particles confines the spatial distribution of electrons, leading to the quantised energy levels due to size effect. The magnetic properties of nanoparticles significantly differ from those of the bulk. First of all, unlike bulk ferromagnetic materials consisting of multiple magnetic domains, each nanometer-sized particle can contain only one magnetic domain [2,3]. Moreover at room temperature magnetic nanoparticles, as a rule, exhibit superparamagnetic behaviour combining giant magnetic moment with zero remanence. Also the large surface-to-volume ratio leads to different local environments for the surface atoms in comparison with volume atoms and hence magnetic characteristics of nanocrystals are determined both by volume and surface contributions.

Further development of the technology requires the miniaturisation of the devices into nanometer sizes while their ultimate performance is drastically enhanced. This raises many issues regarding to new materials for achieving specific functionality and selectivity [4]. Spin-dependent tunnelling electron transport has been recently demonstrated in an array of close-packed cobalt nanoparticles [5]. Granular materials consisting of nanometer size magnetic particles in a dielectric or nonmagnetic metal matrix exhibit giant magnetoresistive properties [6-10]. Thin granular films of ferromagnetic nanocrystals are already the basis of conventional magnetic storage media (hard drivers). It is expected that the advanced magnetic media based on ordered arrays of monodisperse nanocrystals might reach magnetic recording densities between 100 Gb/in<sup>2</sup> and 1 Tb/in<sup>2</sup> [11]. Ultra-high density recording media require uniform particles ( $\sigma < 10\%$ ) with room-temperature coercivity  $H_c$  of  $\sim 3000 - 5000$  Oe.  $H_c$  close to this value can be achieved in intermetallic nanocrystals such as platinum – iron and platinum cobalt alloys [12,13].

Magnetic metal nanoparticles can find future applications as catalysts [4]. Metal functionality of magnetic alloy nanoparticles provides applications typical for metal nanoparticles, such as single electron devices [5,16]. Magnetic colloids, or ferrofluids, are based on magnetic nanoparticles coated with a layer of surfactant dispersed in a carrying solvent. The molecules of surfactant (further referred to as “stabilizing agents” or “stabilizers”) bind to the nanoparticle surface preventing coagulation and providing solubility

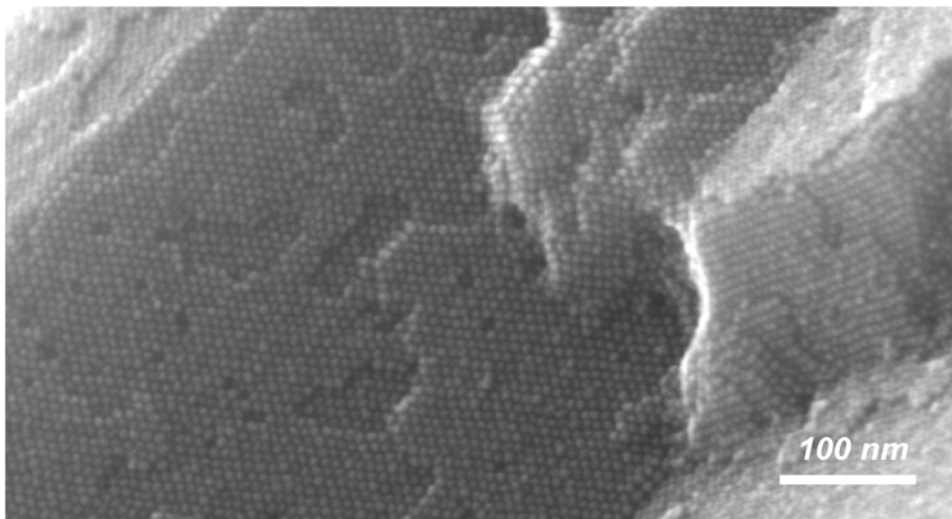
and desired surface properties. Moreover, stabilizers protect the particles from oxidation and can strongly affect the magnetic properties [17-19]. Ferrofluids have been extensively studied and harnessed in a variety of applications [3]. For example, the magnetoreological properties of magnetic colloids are exploited in high-performance bearings and seals.

Among various solution phase approaches, the recently developed *colloidal organometallic syntheses* seem to be the most promising routes for preparation of high quality magnetic nanocrystals. These methods are based on reducing metal salts or thermolysis of zero-valent organometallic precursors in the medium of a highly boiling solvent in the presence of special stabilizing agents which adsorb reversibly to the nanoparticle surface mediating the growth rate. The proper choice of surfactants, precursors, as well as the temperature regime allows successful preparation of monodisperse colloids of highly crystalline magnetic nanoparticles. The pioneer work by Sun et al. demonstrated the possibility of preparation of monodisperse platinum - iron magnetic alloy nanocrystals with controllable composition. The promising magnetic characteristics of platinum – iron nanocrystals initiated a great interest in the further investigation of this system and search for synthetic routes of other alloy systems. To date, the monodisperse nanocrystals of platinum - iron or cobalt – platinum magnetic alloys are the best candidates for the permanent magnetic applications because of their large uniaxial anisotropy [12,14] and high chemical stability [15]. The synthesis and characterization of various magnetic nanocrystals prepared via organometallic approaches are discussed in Chapters 2 and 4.

The synthesis of different monodisperse magnetic nanocrystals of desired size, shape and properties is first step being pre-requisite of their further investigation and use for practical applications. Narrow size distribution, or monodispersity, is strongly desired because magnetic properties become strongly size dependent in the nanometer size range. Despite the progress in the synthesis of nanocrystals of magnetic oxides, transition metals or magnetic alloys, there is still a lack of understanding of the processes occurring in colloidal solution during the synthesis of nanocrystals. The size control of a variety of magnetic nanocrystals is achieved by empirical variation of the precursors. Definitely, understanding of mechanism of the formation of magnetic alloy nanocrystals can provide clear approaches to their size, shape and size distribution control. The mechanism of nucleation and growth of magnetic alloy nanocrystals is discussed in Chapter 3.

Size-dependent magnetic properties of cobalt-platinum alloy nanoparticles are discussed in Chapter 5. A possibility to manipulate with nanoparticles across a distance by applying an external magnetic field opens a broad field for biomedical applications of magnetic

nanoparticles. Specific surface groups of the stabilizers can be used for linking different species to the nanoparticle surface. Drugs, antibodies, *etc.* can be attached to the surface of a colloidal magnetic nanoparticle and can be steered into regions of the body where they are required with applied magnetic field [3]. Functionalised magnetic nanoparticles can be specifically attached to cancer tumour and heated up by AC magnetic field resulting in the tumour thermoablation (magnetic fluid hyperthermia) [20]. Magnetic nanoparticles coupled with oligonucleotides were used as a nanosensor for the detection and separation of complimentary specific oligonucleotides [21]. The biological applications require the water-soluble magnetic particles, stable without loss of properties over large periods of time. In Chapter 4 the phase transfer of magnetic alloy nanocrystals from organic into aqueous media is reported.



*Monodisperse magnetic alloy nanocrystals can be used as "building blocks" to form highly ordered macroscopic objects.*

Size and shape selected nanocrystals are ideal building blocks for one-, two- and three dimensional superstructures. The electric, transport and magnetic properties depend not only on the characteristics of individual nanocrystals, but also on the interactions between neighbouring nanocrystals. Layers of controllable thickness of spatially separated nanoparticles that exhibit ferromagnetic behaviour at room temperature are considered as a promising way towards high density recording devices [12]. Chapter 6 describes the assembly of magnetic alloy nanocrystals in one-, two- and three dimensional structures.

**References:**

1. Murray, C.B.; Sun, S.; Doyle, H.; Betley, T. *MRS Bulletin* **2001**, 985.
2. Leslie-Pelecky, D.L.; Rieke, R.D. *Chem. Mater.* **1996**, 8, 1770.
3. Kenneth J. Klabunde, *Nanoscale Materials in Chemistry*, John Wiley & Sons, Inc. **2001** (Sorensen C.M. *Magnetism* pp.162-221).
4. Wang, Z.L. *Characterisation of Nanophase Materials*, 2000, Wiley-VCH Verlag GmbH. (Nanomagnetism, deHeer, W.A., 289-314).
5. Black, C.T.; Murray, C.B.; Sandstrom, R.L.; Sun, S. *Science* **2000**, 290, 1131.
6. Chien, C.L. *J. Appl. Phys.* **1991**, 69, 5267.
7. Berkowitz, A.E.; Mitchell, J.R.; Carey, M.J.; Young, A.P.; Zhang, S.; Spada, F.E.; Parker, F.T.; Hutten, A.; Thomas, G. *Phys. Rev. Lett.* **1992**, 68, 3745.
8. Xiao, J.Q.; Jiang, J.S.; Chien, C.L. *Phys. Rev. Lett.* **1992**, 68, 3749.
9. Lipkin, H.J. *Phys. Rev. Lett.* **1987**, 58, 425.
10. Takahashi, S.; Maekawa, S. *Phys. Rev. Lett.* **1998**, 80, 1758.
11. Sun, S.; Murray, C. B. *J. Appl. Phys.* **1999**, 85, 4325.
12. Sun, S.; Murray, C.B.; Weller, D.; Folks, L.; Moser, A. *Science* **2000**, 287,1989.
13. Park, J.; Cheon, J. *J. Am. Chem. Soc.* **2001**, 123, 5743.
14. Weller, D.; Brändle, H.; Chappert, C. *J. Magn. Magn. Mater.* **1993**, 121, 452.
15. Tyson, T.A.; Conradson, S.D.; Farrow, R.F.C.; Jones, B.A. *Phys. Rev. B* **1996**, 54, R3702.
16. Doty, R.C.; Yu, H.; Shih, C.K.; Korgel, B.A. *J. Phys. Chem. B* **2001**, 105, 8291.
17. Russier, V.; Petit, C.; Legrand, J.; Pileni M. P. *Phys. Rev. B* **2000**, 62, 3910.
18. van Leeuwen, D.A.; van Ruitenbeek, J.M.; de Jongh, L.J.; Ceriotti, A.; Pacchioni, G. *Phys. Rev. Lett.* **1994**, 73, 1432.
19. Bødker, F.; Mørup, S.; Linderøth, S. *Phys. Rev. Lett.* **1994**, 72, 282.
20. Jordan, A.; Scholz, R.; Wust, P.; Fähling, H.; Felix, R. *J. Magn. Magn. Mater.* **1999**, 201, 413.
21. Josephson, L.; Perz, J.M.; Weissleder, E. *Angew. Chem. Int. Ed.* **2001**, 40, 3204.

## 2. Organometallic synthesis and characterisation of monodisperse CoPt<sub>3</sub> nanocrystals.

---

*Reduction of platinum acetylacetonate and thermodecomposition of cobalt carbonyl in the presence of 1-adamantanecarboxylic acid were employed in different coordinating mixtures to produce monodisperse, highly crystalline CoPt<sub>3</sub> nanoparticles. The key point of the synthesis is the use of a novel efficient stabilizer – 1-adamantanecarboxylic acid. The mean particle size can be varied by controlling the reaction conditions and the type of coordinating mixture. As-synthesised CoPt<sub>3</sub> particles represent single crystal domains and have chemically disordered face-centered cubic (fcc) structure. CoPt<sub>3</sub> nanocrystals dissolved in the non-polar solvent (toluene, chloroform, hexane) form long term stable colloids.*

---

### 2.1. Introduction

Notwithstanding a great interest to any magnetic materials during last years, nowadays only a few synthetic works describing the preparation of high quality magnetic nanocrystals are known [1-10]. The term “high quality nanocrystals” means the follows: the achievement of desired particle sizes over the largest possible range, narrow size distributions, good crystallinity and desired surface properties [11]. The first high quality magnetic nanocrystals were obtained for cobalt [2,3,12] only few years ago. The possibility of control of size and crystalline structure provided the opportunities to monitor the size and structure dependent properties of magnetic materials [2]. The first receipt of preparation of a high quality magnetic alloy nanocrystals was demonstrated only in 2000. Sun et al. [8] succeeded in the synthesis of highly crystalline platinum – iron alloy nanoparticles with narrow size distribution and found the possibilities of size and composition control. This pioneer work showed the advantages of metal alloy nanocrystals (higher coercivity, relatively high stability against oxidation and *etc.*) in comparison with elemental magnetic metal nanocrystals and provoked the interests to the development of synthetic approaches for other alloy system. The difficulty of preparation of novel system originates from the impossibility of direct transferring of the reaction conditions developed and adopted, for example, for the synthesis of PtFe systems (or Co, or carefully studied semiconductors) to the synthesis of nanocrystals of another chemical composition.

## 2. Organometallic synthesis and characterisation of monodisperse CoPt<sub>3</sub> nanocrystals

Because of technological implication in high-density magneto-optical storage media, the magnetic alloys seems to be the candidate of first choice [13]. Recently, the preparation of Co – Pt alloy nanoparticles from organometallic precursors in the presence of polymer was reported [1,14]. Unfortunately, the synthetic approach allows to prepare only polydisperse Co-Pt alloy nanocrystals with the sizes smaller than 1.8 nm. Because of strong perpendicular magnetic anisotropy of bulk Co – Pt alloys [15] and their high chemical stability [16], these materials might be especially suitable for magneto-optical storage media [17-21].

In *this Chapter* several synthetic organometallic approaches used a novel regulating and stabilizing agent (adamantanecarboxylic acid) to prepare CoPt<sub>3</sub> magnetic alloy nanocrystals will be reported. These approaches allow to obtain nearly monodisperse, highly crystalline CoPt<sub>3</sub> nanocrystals. Depending on the coordinating mixtures and reaction temperatures the preparation of different size series is possible.

### **2.2. Synthesis of CoPt<sub>3</sub> nanocrystals.**

CoPt<sub>3</sub> nanocrystals were prepared *via* the simultaneous reduction of Pt(acac)<sub>2</sub> and thermodecomposition of Co<sub>2</sub>(CO)<sub>8</sub> in the presence of organic molecules terminating the growth of Co - Pt bulk phases. A similar approach has been recently applied for the preparation of monodisperse FePt nanocrystals [8]. In this work the authors used a binary stabilizer mixture of oleic acid and oleylamine. For Co-Pt alloy nanocrystals this mixture resulted, however, in the formation of a product which was almost amorphous in XRD. This result is consistent with a recent finding of Park *et al.* [1] who reported the formation of CoPt<sub>3</sub> particles with diameters below 1.8 nm under these conditions. In the case of pure Co nanoparticles Sun *et al.* [12] assumed a strong binding of oleic acid to surface sites which greatly impeded the particles to growth. Our results also suggest a too strong complexation of the metal by this stabilizer. Various capping agents (TOPO, TOP, phosphonic acids, primary and secondary amines, fatty acids and mixtures of these compounds) were systematically tested in order to prepare stable colloids of Co-Pt alloy nanocrystals.

## 2. Organometallic synthesis and characterisation of monodisperse CoPt<sub>3</sub> nanocrystals

We found that high quality nanocrystals in the reported size regime could only be obtained in the presence of 1-adamantanecarboxylic acid (ACA)\* or 1-adamantanecetic acid.

The best results (with respect to control of nanoparticle size, monodispersity, crystallinity as well as the reproducibility of the synthesis) were obtained with two-component mixtures of HDA - diphenyl ether and TDPA - diphenyl ether (see Table 2.1). In fact, HDA and TDPA have been previously applied in the synthesis of cadmium chalcogenide nanocrystals of controllable sizes and shapes [22].

A typical colloidal organometallic synthesis is carried out under an inert gas atmosphere using standard Schlenk line technique as shown in Figure 2.1 on an example of CoPt<sub>3</sub> nanocrystals [9]. Injection of the cobalt precursor into a hot solution containing platinum acetylacetonate and stabilizing agent (ACA) in a mixture of hexadecylamine (HDA) and diphenyl ether induces fast a simultaneous decomposition of platinum and cobalt precursors yielding CoPt<sub>3</sub> nanocrystals. Subsequent annealing of the nanoparticles at ~280°C is necessary to improve their crystallinity. After cooling the reaction mixture to room temperature, the nanocrystals are precipitated by addition of propanol-2 and isolated from the crude solution by centrifugation. The isolated nanocrystals are easily re-dispersable in a variety of non-polar organic solvents like chloroform, hexane or toluene.

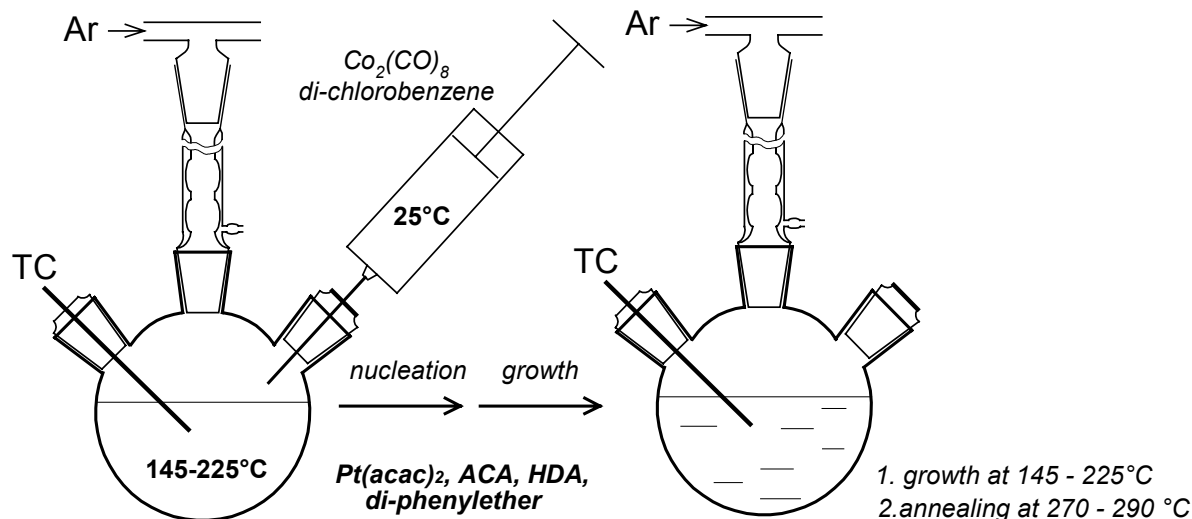
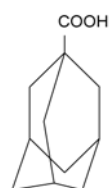


**Figure 2.1.** Scheme of the organometallic synthesis of CoPt<sub>3</sub> nanocrystals

\*



Graphical formula of adamantanecarboxylic acid.

## 2. Organometallic synthesis and characterisation of monodisperse CoPt<sub>3</sub> nanocrystals

**Table 2.1.** *Experimental conditions applied for preparation of CoPt<sub>3</sub> nanocrystals.\**

Coordinating solvent mixtures	Temperature of injection, °C	Temperature of reaction, °C	Time of reaction	Comments
HDA – diphenyl ether	100	268-290	1 min	Spherical nanocrystals of ~4 – 6 nm size, some amount of nanowires
			40 min	Spherical nanocrystals of ~4 – 6 nm size, some amount of nanowires
			3 h	Almost only spherical nanocrystals of ~4 – 6 nm
	170	230	40 min	Spherical nanocrystals of 4.0 nm
		268		Spherical nanocrystals of 4.0 nm
	220	230		Spherical nanocrystals of 2.6 nm
TDPA - diphenyl ether	100	255	40 min	Spherical nanocrystals of ~3 – 5 nm
	170	255		Spherical nanocrystals of ~3.6 nm
HDA, 1-hexadecanol	100	220	40 min	Spherical nanocrystals of ~1.5 – 2 nm
	170			

\* - ACA was used as stabiliser throughout

The use of the HDA - diphenyl ether coordinating mixture and injection of the cobalt stock solution at 100°C generally allowed the synthesis of spherical CoPt<sub>3</sub> nanocrystals with sizes ranging from ~4 to 5.5 nm. As an example, the size-histogram of a as-prepared CoPt<sub>3</sub> nanocrystal sample with a mean size of 4.8 nm (std. div. – 12%) is given in *Experimental Section, Figure ES.1*). Under these reaction conditions some amount of nanowires were also formed as a side-product (Figure 2.2).

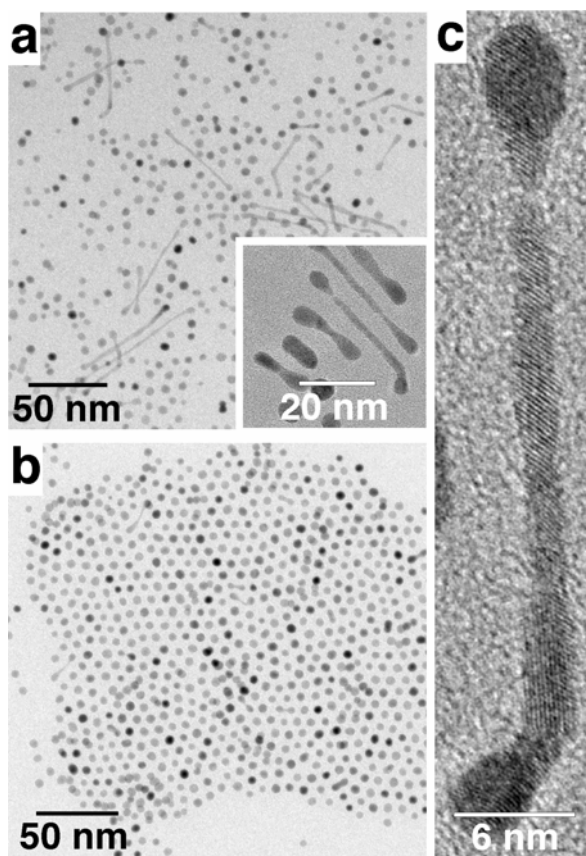


**Figure 2.2.** TEM images of as-prepared CoPt<sub>3</sub> nanocrystals grown in the HDA – diphenyl ether mixture: (a) 40 min refluxing, the inset shows an enlarged view of non-uniformly shaped nanowires; (b) refluxing for 3 h, almost no nanowires are seen. (c) HRTEM image of a CoPt<sub>3</sub> nanowire illustrating differently oriented crystalline domains.

The amount of wires and their length decreased drastically upon prolonged (~3 h) refluxing (Figure 2.2b). The length of the wires varied from 6 nm up to 150-200 nm. The wires were not uniform in length, but typically comprised two ‘heads’ at the ends which were of approximately the same size as the spherical particles in the same sample, and a ‘body’ with some bulges (Figure 2.2c). CoPt<sub>3</sub> nanowire-rich fractions can be isolated by high-speed centrifugation of colloidal solution (Figure 2.3) or by size selective precipitation technique.

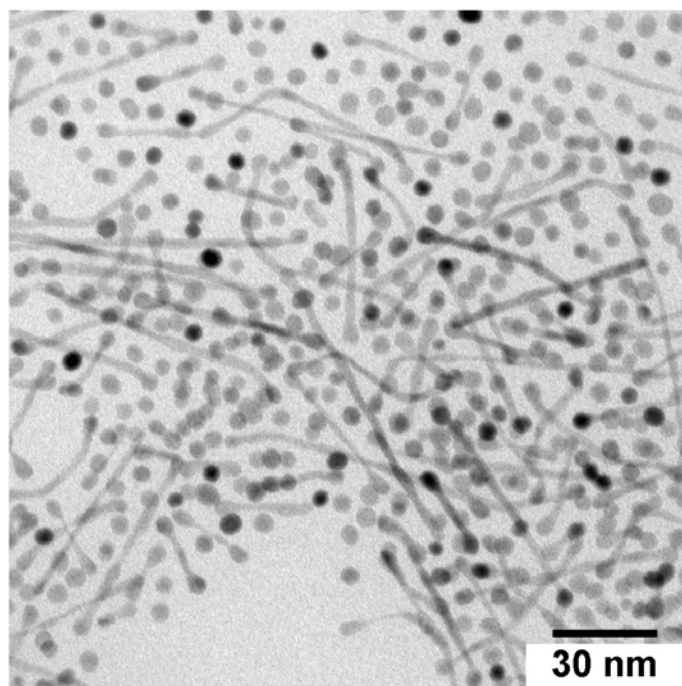


**Figure 2.3.** *A typical TEM image of a nanowires-rich CoPt<sub>3</sub> fraction.*

In order to find the way of preparation of CoPt<sub>3</sub> nanowires the reaction conditions (reaction temperature, concentrations and types of stabilisers and metal precursors, *etc.*) were systematically varied. It was found that an increase of the reaction temperature as well as an increase of the concentration of Pt(acac)<sub>2</sub> suppressed the wire formation.\* Increase of the concentration of Co<sub>2</sub>(CO)<sub>8</sub> resulted in the slight increase of the amount of CoPt<sub>3</sub> nanowires. A significant increase of the yield of wires was also observed when the synthesis was carried out without stirring. However nanowires prepared in a such a manner had no uniform composition. TEM analysis revealed that most of wires had core-shell structure (Figure 2.4a), while XRD data were typical for CoPt<sub>3</sub> nanocrystals and the presence of other substances was not detected by XRD. This means that the shell is either almost amorphous or polycrystalline material. Both suggestions are in agreement with HRTEM data which revealed the crystalline structure of the core and a nearly amorphous shell with some impregnation of crystalline material. Figure 2.4a represents a typical TEM image of core-shell nanowires: the dark core is surrounded by a shell with much lower contrast. The overview EDX analysis of such samples showed a higher concentration of cobalt (~70 at.%). As evidenced from EDX data from

\* Unfortunately, it is rather difficult to carry out a quantitative comparison of the influence of different factors on the wire formation, since CoPt<sub>3</sub> nanowires are mainly polycrystalline and hence XRD data can not indicate the presence of wire. Also TEM analysis has the high spatial selectivity and in the case of size segregation the overview information can not be obtained. Against this background our results in this set of experiments have only qualitative character.

## 2. Organometallic synthesis and characterisation of monodisperse CoPt<sub>3</sub> nanocrystals

selected wires the content of cobalt in the shell is ~ 95 at.%, while “naked” wires (Figure 2.4b) are characterised by the composition close to CoPt<sub>3</sub>. The mechanism of the formation and decomposition of nanowires requires further careful investigations.

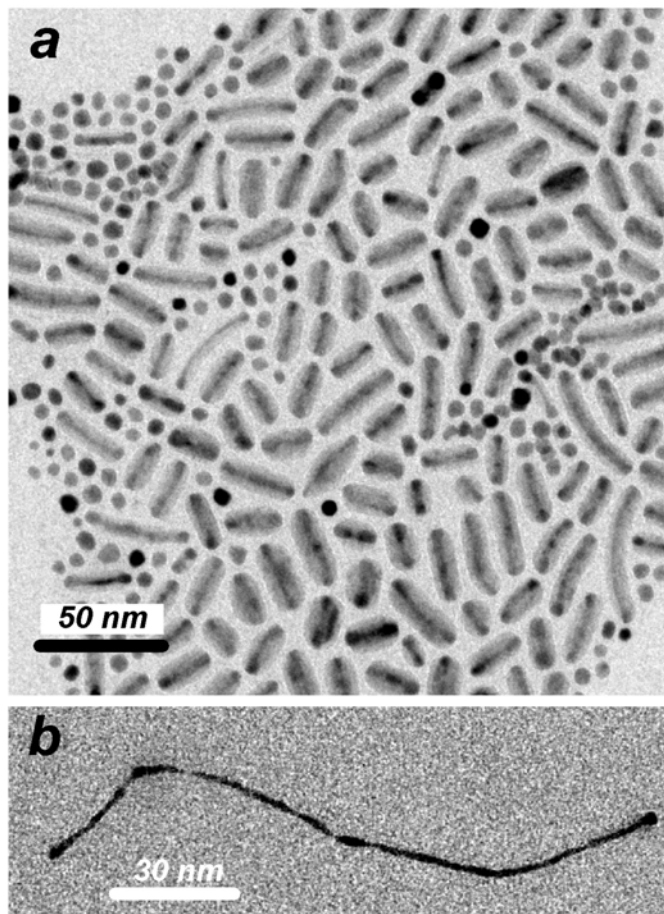


**Figure 2.4.** TEM images of as-prepared core-shell (a) and “naked” (b) wires grown in HDA – diphenyl ether mixture without stirring.

Exclusively spherical CoPt<sub>3</sub> nanocrystals were formed in TDPA - diphenyl ether or HDA – 1-hexadecanol (Table 2.1). The analysis of TEM images and XRD data shows that the duration of heating had no pronounced influence on the size of the spherical nanocrystals. Thus, refluxing for 1 min, 40 min and 3 h resulted in similar sizes and size distributions of spherical CoPt<sub>3</sub> nanocrystals. The use of TDPA - diphenyl ether as the coordinating mixture yielded spherical CoPt<sub>3</sub> nanocrystals with smaller sizes ranging from ~3 to 5 nm. CoPt<sub>3</sub> nanocrystals of ~1.5 to 2 nm (the HRTEM images of which are shown in Figure 2.5a) were obtained in HDA - 1-hexadecanol. Subsequent size-selective precipitation allowed to narrow the size distribution.

## 2. Organometallic synthesis and characterisation of monodisperse CoPt<sub>3</sub> nanocrystals

When the cobalt stock solution was injected into the reaction mixture at higher temperature (170°C instead of 100°C), monodisperse spherical CoPt<sub>3</sub> nanocrystals with mean sizes of about 4 nm and ~3.5 nm were obtained in HDA - diphenyl ether and TDPA - diphenyl ether, respectively. The corresponding TEM images are shown in Figure 2.5b (std. div.- 9%, see *Experimental Section, Figure ES.2*). No post-preparative size-selection was necessary to obtain the narrow particle size distribution in this case. A similar effect of narrowing the particle size distribution was observed for so-called “hot injection” technique in the synthesis of CdSe and InAs nanocrystals [22-24], where narrow size distributions were achieved by separating the nucleation and growth steps. Usually, monodisperse CoPt<sub>3</sub> nanocrystals spontaneously formed 3D arrays on the TEM grids, making the estimation of standard deviation in such cases difficult. Counting the lattice planes of individual nanocrystals in HRTEM images provides very high monodispersity within the self-assembled domains.

Additional injections of platinum and cobalt precursors into the solutions of the CoPt<sub>3</sub> nanoparticles prepared in HDA - diphenyl ether or TDPA - diphenyl ether coordinating mixtures increased the mean size keeping the size distribution still narrow. Figure 2.5c represents ~6.2 nm (std. div. – 12%%, see *Experimental Section, Figure ES.2*) CoPt<sub>3</sub> nanocrystals obtained from monodisperse 4.0 nm CoPt<sub>3</sub> nanocrystals by one additional injection of the corresponding amount of precursors. Obviously, the 4 nm particles acted as nucleation seeds for the deposition of the additional monomer. However, more than two additional injections led to a substantial broadening of the size distribution and formation of ~10 nm irregular-shaped polycrystalline CoPt<sub>3</sub> nanocrystals.

CoPt<sub>3</sub> nanocrystals prepared by one of these three approaches (Table 2.1) were soluble in any non-polar solvent (hexane, toluene or chloroform). These nanocrystals also revealed the good solubility in monomers, like laurilmethacrylate (LMA) which allowed to carry out the radical polymerisation of LMA in the presence of CoPt<sub>3</sub> nanocrystals of different concentrations. By this technique can one obtain randomly distributed magnetic nanocrystals strongly fixed in the polymer matrix. Such materials can be interesting for the investigation of magnetic behaviour of non-interacting magnetic nanoparticles (*Chapter 5*).

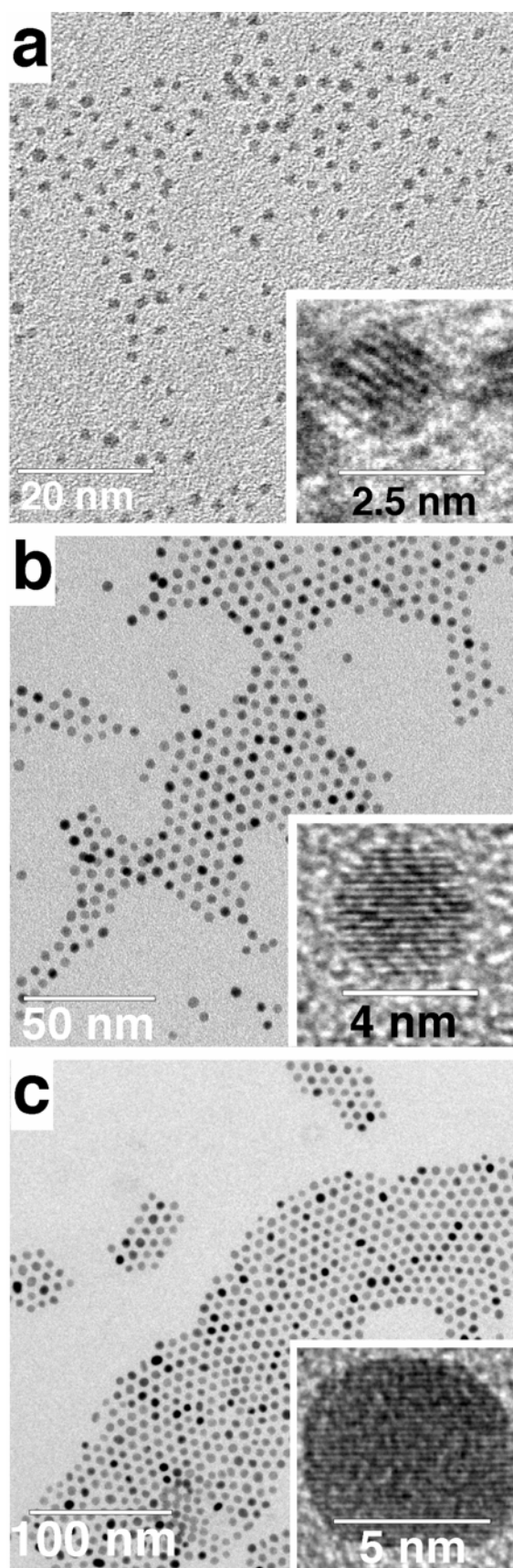


**Figure 2.5.** TEM overview of 1.5 nm (a), 3.8 nm (b) and 6.2 nm (c)  $\text{CoPt}_3$  nanocrystals. Insets show HRTEM image of each size.

## 2. Organometallic synthesis and characterisation of monodisperse CoPt<sub>3</sub> nanocrystals

In order to further elucidate the role of ACA, HDA and TDPA in the respective reaction mixtures we either removed one component completely during the synthesis or added it at a later stage of preparation. These experiments were performed using diphenylether as the solvent and the results can be summarised as follows: Using only ACA as stabilizer also allowed the synthesis of crystalline CoPt<sub>3</sub> nanoparticles which, however, exhibit a rather broad size distribution and a rather poor colloidal stability, i.e. these particles precipitated within one day after the final re-dissolution step (see post-preparative procedures, Experimental Section). The resulting precipitate could not be re-dissolved by an excess of ACA, whereas addition of HDA or dodecylamine resulted in an immediate and TDPA in a slow formation of a clear colloidal solution. On the other hand, when ACA was removed from the reaction mixture and only amines or TDPA were used from the beginning, a black precipitate of bulk Co and Pt was formed which could not be re-dissolved by any post preparative treatment. We therefore conclude that ACA has the main influence on the formation and stabilization of CoPt<sub>3</sub> nanocrystals, whereas amines and phosphonic acid act as co-surfactants improving the stability and size distribution of the resulting nanocrystals. We assume that HDA is object of a reversible, dynamic surface equilibrium. This assumption is supported by the observation that repeated washing with ethanol results in precipitation of CoPt<sub>3</sub> nanocrystals, which, however, can easily be re-dissolved after renewed addition of HDA.

It appears feasible to connect the extraordinary role of ACA with the bulky adamantyl end groups. In contrast to linear chains these adamantyl groups will probably protect a number of free surface sites from being co-ordinated by ligand molecules and, thus, increase the free surface energy. This explains why the particles grow to larger sizes and crystallisation easily occurs in contrast to experiments with fatty acids.

ATR-FTIR investigations were carried in order to verify the postulated surface chemistry. Unfortunately, these spectra were strongly dominated by CH vibrations which can hide additional information about interaction behaviour of ACA and TDPA with the surface of CoPt<sub>3</sub> nanocrystals. Although slightly shifted bands of the carboxylic acid groups (COO<sup>-</sup>) could be detected at  $\nu = 1600$  and  $1450 \text{ cm}^{-1}$ , an unambiguous interpretation of possible binding sites is presently not possible. Amine stretching bands, as present in the spectrum of pure HDA could not be detected in the samples of our nanocrystals.

In another set of blank experiments we tried the preparation of pure Co and pure Pt nanoparticles by removing the respective precursor under identical reaction conditions. As a result, we obtained a transparent blue solution in the case of prolonged heating cobalt

## 2. Organometallic synthesis and characterisation of monodisperse CoPt<sub>3</sub> nanocrystals

carbonyl without any traces of crystalline material, whereas the respective experiment with Pt(acac)<sub>2</sub> resulted in the formation of bulk fcc platinum which precipitated immediately. It means that capping ligands can not provide the sufficient passivation of the platinum surface, probably, because of too high lattice energy of platinum. This behaviour can be explained with strong differences in the binding energy of ACA to Co and Pt and suggests that ACA preferentially binds to Co. In this sense at least two types of surface sites of CoPt<sub>3</sub> nanocrystals can be proposed.

### **2.3. Structural characterisation of CoPt<sub>3</sub> nanocrystals.**

ICP AES measurements showed the ratio between Co and Pt being close to 1:3 for all samples studied. EDX measurements indicated the same compositions.

HRTEM images (*insets* in Figure 2.5a, 2.5b, 2.5c) of differently sized CoPt<sub>3</sub> nanocrystals show crystalline particles with clearly resolved lattice fringes and almost no distortions within the nanocrystal cores. XRD patterns of as-prepared nanocrystals (Figure 2.6) corresponded to the chemically disordered face-centered cubic (*fcc*) CoPt<sub>3</sub> structure which was also observed for vapour-deposited Co<sub>x</sub>Pt<sub>1-x</sub> films [20]. The width of the diffraction peaks at wide angles was considerably broadened and increased with decreasing particle size (Figure 2.6, *inset*). The intensity pattern of the reflexes and the lattice constant were very close to that of the CoPt<sub>3</sub> bulk phase [25,26] and showed that the nanocrystals did not grow in a preferred direction. Particle sizes calculated from the peaks widths agreed well with the sizes observed in the TEM images indicating a very high degree of average particle crystallinity, i.e. the particles represent single crystalline domains.

Although the XRD patterns are in good agreement with CoPt<sub>3</sub>, nano-phase segregation or even core-shell formation can not completely be excluded from these data. We believe, however, that these processes do not occur under our reaction conditions for the following reasons: Because of its much lower contrast domains of pure Co should be recognised in TEM against a background of Pt or CoPt<sub>3</sub>. However, segregated Pt domains can not be distinguished from CoPt<sub>3</sub> by TEM because of the similarity in phase contrast and lattice spacing. Nevertheless, the behaviour of the pure elementary compounds (Co and Pt) as well as the constant stoichiometry observed for the obtained nanocrystals rule out the possibility of nano-phase segregation or core-shell formation from our point of view.

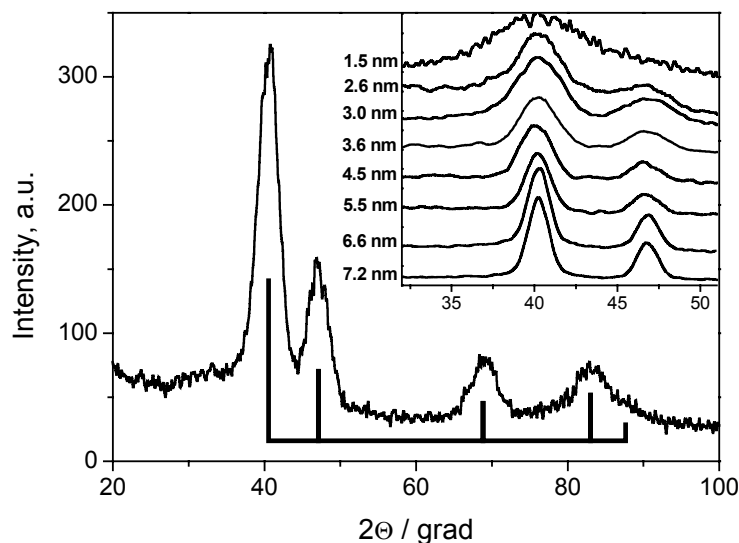


**Figure 2.6.** XRD pattern of as-synthesised 4.0 nm CoPt<sub>3</sub> nanocrystals (reflexes of bulk fcc CoPt<sub>3</sub> are shown with a stick spectrum). Inset: Size-dependent XRD. The particle size was calculated by Debye–Sherrer equation.

## 2.4. Conclusions

A colloidal synthesis of CoPt<sub>3</sub> nanoparticles was developed for the first time allowing the preparation of highly crystalline particles of different distinct sizes with narrow particle size distribution. The key point of the synthesis is the use of the novel stabiliser 1-adamantancarboxylic acid. Elemental analysis, XRD data, TEM and HRTEM images provided direct prove of the formation of highly crystalline CoPt<sub>3</sub> nanoparticles possessing a chemically disordered *fcc* structure. As expected, the reaction conditions such as capping ligands, reaction temperature, *etc* influenced on the final size of CoPt<sub>3</sub> nanocrystals. Variation of the capping ligands in co-ordinating mixtures allowed to prepare nearly monodisperse differently sized CoPt<sub>3</sub> nanocrystals. However, in this case the differently sized nanocrystals have different capping ligands attached to the particle surface. The surface chemistry of magnetic nanocrystals can significantly influence the magnetic properties of the material (see *Chapter 5*) and complicate investigation of size-dependent magnetic properties. Further progress in the investigation and understanding of size-dependent magnetic properties of nanocrystals depends on our ability to understand and control the parameters governing the size of colloiddally grown magnetic alloy nanocrystals. The next Chapter deals with the further

investigation of the microscopic processes responsible for nucleation and growth of magnetic alloy nanocrystals.

## **2.5. References**

1. Park, S.J.; Kim, S.; Lee, S.; Khim, Z.G.; Char, K.; Hyeon, T. *J. Am. Chem. Soc.* **2000**, *122*, 8581.
2. Murray, C.B.; Sun, S.; Doyle, H.; Betley, T. *MRS Bulletin* **2001**, 985.
3. Sun, S.; Murray, C.B.; Doyle, H. *Mat. Res. Soc. Symp. Proc.* **1999**, *577*, 385.
4. Puentes, V.F.; Krishnan, K.; Alivisatos A.P. *Topics in Catalysis* **2002**, *19*, 145.
5. Puentes, V.F.; Krishnan, K.; Alivisatos A.P. *Science* **2001**, *291*, 2115.
6. Puentes, V.F.; Zanchet, D.; Erdonmez, C.K.; Alivisatos, A.P. *J. Am. Chem. Soc.* **2002**, *124*, 12874.
7. Dumestre, F.; Chaudret, B.; Amiens, C.; Fromen, M.-C.; Casanove, M.-J.; Renaud, P.; Zurcher, P. *Angew. Chem. Int. Ed.* **2002**, *41*, 4286.
8. Sun, S.; Murray, C.B.; Weller, D.; Folks, L.; Moser, A. *Science* **2000**, 287,1989.
9. Shevchenko, E.V.; Talapin, D.V.; Rogach, A.L.; Kornowski, A.; Haase, M.; Weller, H.. *J. Am. Chem. Soc.* **2002**, *124*, 11480.
10. Hyeon, T.; Lee, S.S.; Park, J.; Chung, Y.; Na, H. B. *J. Am. Chem. Soc.* **2001**, *123*, 12798.
11. Eychmüller, A. *J. Phys. Chem. B* **2000**, *104*, 6514.
12. Sun, S.; Murray, C. B. *J. Appl. Phys.* **1999**, *85*, 4325.
13. Pustogova, U.; Zabloudil, J.; Uilberacker, C.; Blass, C.; Weinberger, P.; Szunyogh, L.; Sommers, C. *Phys. Rev. B* **1999**, *60*, 414-420.
14. Ould Ely, T.; Pan, C.; Amiens, C.; Chaudret, B.; Dassenoy, F.; Lecante, P.; Casanove, M.-J.; Mosset, A.; Respaund, M.; Broto, J.-M. *J. Phys. Chem. B* **2000**, *104*, 695.
15. Weller, D.; Brändle, H.; Chappert, C. *J. Magn. Magn. Mater.* **1993**, *121*, 461.
16. Tyson, T. A.; Conradson, S. D.; Farrow, R. F. C.; Jones, B. A. *Phys. Rev. B* **1996**, *54*, R3702.
17. Grange, W.; Maret, M.; Kappler, J.-P.; Vogel, J.; Fontaine, A.; Petroff, F.; Krill, G.; Rogalev, A.; Coulon, J.; Finazzi, M.; Brookes, N. *Phys. Rev. B* **1998**, *58*, 6298.
18. Weller, D.; Brändle, H.; Gorman, G.; Lin, C.-J.; Notarys, H. *Appl. Phys. Lett.* **1992**, *61*, 2726.
19. Lin, C.-J.; Gorman, G. L. *Appl. Phys. Lett.* **1992**, *61*, 1600.

## 2. Organometallic synthesis and characterisation of monodisperse CoPt<sub>3</sub> nanocrystals

20. Shapiro, A.L.; Rooney, P.W.; Tran, M.Q.; Hellman, F.; Ring, K.M.; Kavanagh, K.L.; Rellinghaus, B.; Weller, D. *Phys. Rev. B* **1999**, *60*, 12826.
21. Chang, G.; Lee, Y.; Rhee, J.; Lee, J.; Jeong, K.; Whang, C. *Phys. Rev. Lett.* **2001**, *87*, 067208-1.
22. Peng, X.; Wickham, J.; Alivisatos, A.P. *J. Am. Chem. Soc.* **1998**, *120*, 5343.
23. Talapin, D.V.; Rogach, A.L.; Kornowski, A.; Haase, M.; Weller, H. *Nano Lett.* **2001**, *1*, 207.
24. Peng, Z.A.; Peng, X. *J. Am. Chem. Soc.* **2001**, *123*, 183.
25. Geisler, A. H; Martin, D.L. *J. Appl. Phys.* **1952**, *23*, 375.
26. Hansen, M. *Constitution of binary alloys*, McGraw-Hill: New York Toronto London, **1958**, pp. 492-494.

### 3. The mechanism of nucleation and growth of CoPt<sub>3</sub> nanocrystals

---

*High quality CoPt<sub>3</sub> nanocrystals were synthesized via simultaneous reduction of platinum acetylacetonate and thermodecomposition of cobalt carbonyl in the presence of 1-adamantanecarboxylic acid and hexadecylamine as stabilizing agents. The high flexibility and reproducibility of the synthesis allows us to consider CoPt<sub>3</sub> nanocrystals as a model system for the hot organometallic synthesis of metal nanoparticles. Different experimental conditions (reaction temperature, concentration of stabilising agents, ratio between cobalt and platinum precursors, etc.) have been investigated in order to reveal the processes governing the formation of the metal alloy nanocrystals. It was found that CoPt<sub>3</sub> nanocrystals nucleate and grow up to their final size at an early stage of the synthesis with no Ostwald ripening observed upon further heating. In this case the nanocrystal size can be controlled only via proper balance between the rates for nucleation and for growth from the monomer. Nucleation rate determines the final size of nanocrystals and can be controlled by the reaction temperature, concentration of ACA and monomers. The size of CoPt<sub>3</sub> nanocrystals can be precisely tuned from ~3 nm up to ~18 nm in a predictable and reproducible way. The possible mechanism of homogeneous nucleation, evolution of the nanocrystal ensemble in the absence of Ostwald ripening, and nanocrystal faceting are investigated and discussed.*

---

#### 3.1. Introduction

In the case of crystalline particles consisting of  $\sim 10^2$ - $10^4$  atoms, a nearly continuous tunability of the particle size is possible, as an addition or removal of a unit cell requires only a small variation of the nanocrystal free energy [1]. However, in the majority of the existing routes for metal nanocrystals, tuning of the particle size is based on nearly empirical variation of the ratio between capping groups and metal precursors or on the nature of capping ligands, whereas an exact adjustment of the particle size could only be achieved via costly post-preparative size fractionation [2]. Moreover, the mechanisms responsible for size-control at room temperature and “hot” synthetic routes are, probably, different. For instance, the room

temperature syntheses of Au and Ag nanocrystals agree with the concept of “thermodynamic size-control” – the increase of the stabilizer-to-precursor ratio results in a decrease of the particle size [3]. In contrast, the synthesis of Fe nanocrystals in oleic acid - dioctyl ether mixture at 300°C revealed the opposite behavior – the nanocrystal size increases with increasing concentration of the stabilizing agent (oleic acid) [4]. The lack of information on the processes occurring in the reaction vessel during “hot” organometallic synthesis hinders the development of predictable size-control schemes.

In *this Chapter* we show that size control in the “hot” synthesis of metal nanoparticles is a kinetically driven process where the ratio between the rates for nucleation and for growth is responsible for the final nanocrystal size. The control of this ratio allows an easy tuning of the nanocrystal size as demonstrated on the example of magnetic alloy CoPt<sub>3</sub> nanocrystals, the material being of great interest for ultra-high density magnetic storage media [5].

## **3.2. Study of nucleation and growth of magnetic alloy nanocrystals**

CoPt<sub>3</sub> nanocrystals were prepared via the simultaneous reduction of Pt(acac)<sub>2</sub> and thermal decomposition of Co<sub>2</sub>(CO)<sub>8</sub> in the presence of 1-adamantanecarboxylic acid (ACA) and hexadecylamine (HDA) as stabilising agents. This co-ordinating mixture was chosen as the most appropriate for the investigation of process governing the formation and growth of CoPt<sub>3</sub> nanocrystals due to possibility of variation of a lot of reaction parameters and high reproducibility of the ACA-HDA approach. Synthesised nanocrystals were routinely investigated by powder-XRD and TEM measurements in order to collect statistically reliable data about the dependence of the nanocrystal size, shape, and crystallinity on various reaction parameters. Nanocrystal sizes estimated by these methods will be further referred to as “XRD-size” and “TEM-size” correspondingly. The width of the XRD reflexes provides information about the X-ray coherence length which is close to the average size of the single crystalline domain inside the nanocrystal.

It was found that different experimental conditions (reaction temperature, ratio between the cobalt and platinum precursors, etc.) yielded the nanocrystals with nearly identical chemical composition. Both EDX measurements and chemical analysis of digested nanocrystals indicated compositions being very close to the ratio given by the CoPt<sub>3</sub> formula.

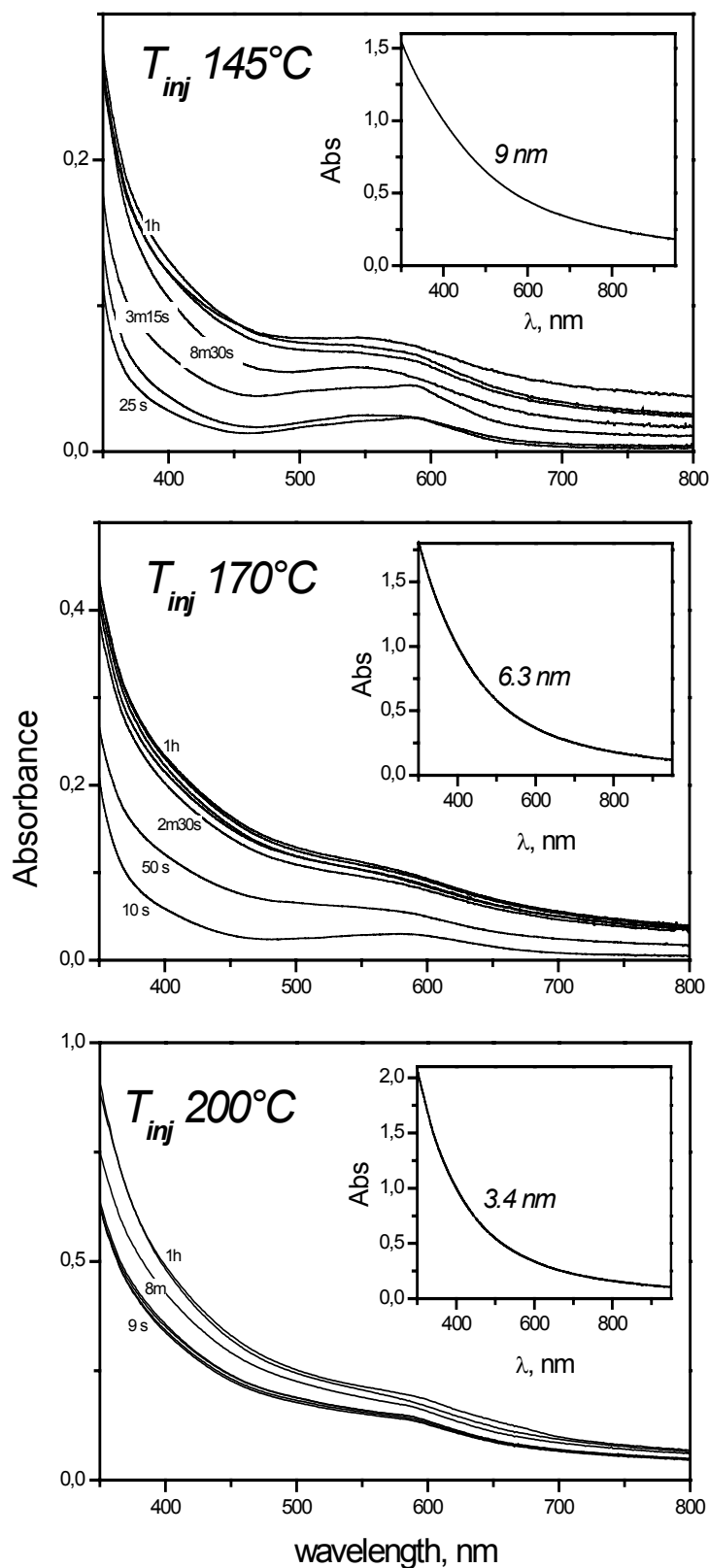


**Figure 3.1.** Temporal evolution of absorption spectra of crude solutions during the synthesis of  $\text{CoPt}_3$  nanocrystals at 145, 170 and  $200^\circ\text{C}$ . Insets show the absorption spectra of washed  $\text{CoPt}_3$  nanocrystals of different sizes in hexane.

### 3. The mechanism of nucleation and growth of $\text{CoPt}_3$ nanocrystals

Injection of the cobalt stock solution results in a colour change of the reaction mixture from pale yellowish to black. The temporal evolution of the absorption spectra of crude solutions is shown in the Figure 3.1.

If the injection temperature is higher than  $\sim 170^\circ\text{C}$  or if the injection is followed by fast heating of the crude solution to the boiling point, the particles rapidly nucleate and grow up to their final size (Figure 3.2a).

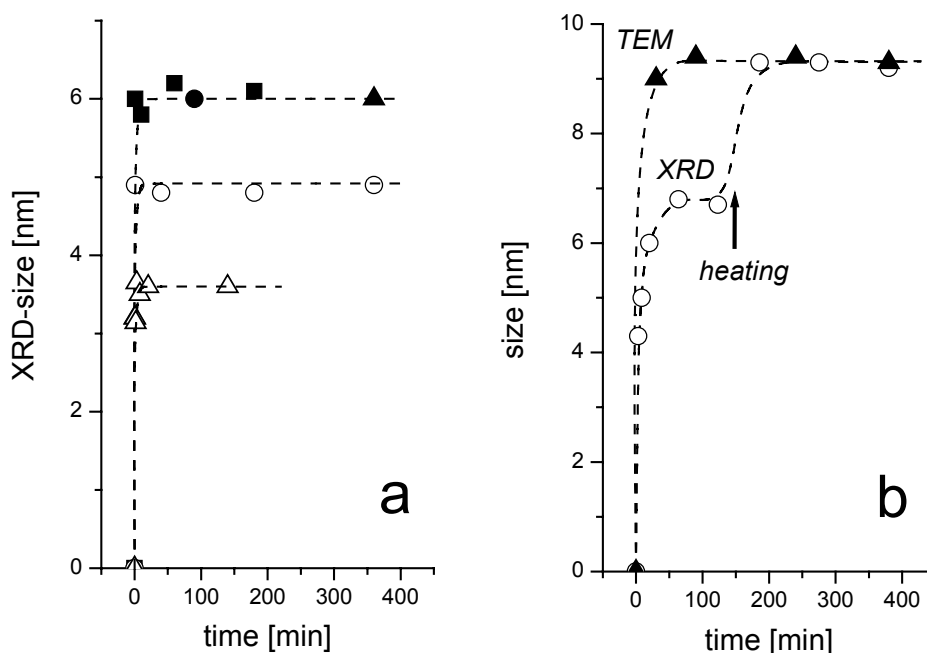


**Figure 3.2.** (a) Dependence of  $\text{CoPt}_3$  nanocrystals size on duration of heating. After injection of the cobalt stock solution at  $100^\circ\text{C}$ , the reaction mixture was rapidly ( $\sim 22^\circ\text{C}/\text{min}$ ) heated to  $\sim 275^\circ\text{C}$ . The molar ratios of Pt : Co : ACA were 1 : 3 : 2 (○) and 1-3-6 (●, ■, ▲ - indicates three different preparations). The evolution of the nanocrystal size during the reaction carried out by injection and heating at  $200^\circ\text{C}$  is shown by (Δ) (b) Evolution of the XRD (○) and TEM (▲) sizes of  $\text{CoPt}_3$  nanocrystals upon formation and annealing. The injection temperature of the cobalt stock solution is  $145^\circ\text{C}$ . Molar ratio Pt : Co : ACA is 1 : 3 : 6. Arrow corresponds to the increase of the reaction temperature from  $145^\circ\text{C}$  to  $\sim 275^\circ\text{C}$ .

Subsequent heating does not result in any detectable changes of the particle size (Figure 3.2.a). Thus, no Ostwald ripening was observed for  $\text{CoPt}_3$  nanocrystals. Prolonged excessive refluxing (days) led to the progressive decomposition of organic compounds rather than to particle growth. The chemical analysis of the supernatant solution after precipitation of the

### ***3. The mechanism of nucleation and growth of CoPt<sub>3</sub> nanocrystals***

---

nanocrystals shows that all Pt(acac)<sub>2</sub> is converted to nanocrystals during the first several minutes after starting the process. Note, that we always used some excess of the cobalt precursor (see *Experimental Section, Table ES.1*). Moreover, no change of the absorption spectra of the crude solution was observed at late stages of the nanocrystal synthesis (Figure 3.1). Therefore, we can conclude that no changes of the particle concentration takes place at late stages of the reaction.

Summarising, at high reaction temperature all CoPt<sub>3</sub> nanocrystals are formed directly after the injection of the cobalt crude solution and grow rapidly to their final size. Further heating does not change the particle size (Figure 3.2a). In the case of a lower reaction temperature, e.g., 145°C, the nanocrystals nucleate during ~2 min after the injection of cobalt stock solution and grow during ~10 min as evidenced from measurements of the TEM-size (Figure 3.2b). Below 130°C no formation of CoPt<sub>3</sub> nanocrystals was observed in a reasonable time window.

More detailed analysis of the temporal evolution of CoPt<sub>3</sub> nanocrystals in the reaction mixture shows a large difference between XRD and TEM sizes (Figure 3.2b) for samples taken directly after the formation of the particles which is a result from a poor crystallinity of the originally formed particles. Annealing of the CoPt<sub>3</sub> nanocrystals at the boiling point (~275-285°C) of the crude solution for ~30 min results in an increase of the XRD-size but no considerable changes of the TEM-size are observed (Figure 3.2b). We believe that the observed decrease of the difference between XRD- and TEM-sizes is a result of the annealing of defects [6] accompanied by an improvement of the particle crystallinity. This annealing process requires relatively high temperatures (200-300°C) to trigger atom diffusion inside the nanocrystals [7]. A more detailed description of the temporal evolution of the CoPt<sub>3</sub> nanocrystal size upon annealing is given in Figure 3.3 which demonstrates the tendency of CoPt<sub>3</sub> nanocrystals of different sizes (prepared in presence of different amounts of ACA) to improve their crystallinity under annealing procedure.

TEM-size of differently sized CoPt<sub>3</sub> nanocrystals prepared at temperatures below 170°C smaller than XRD-size (Figure 3.4a). An improvement of the particle crystallinity under annealing procedure has been observed for all nanocrystal sizes (Figure 3.4b). It allowed us to conclude that the annealing of crystal lattice is an important prerequisite to the formation of high-quality CoPt<sub>3</sub> nanocrystals. After annealing the XRD-size is nearly equal to the TEM-size (Figure 3.4b), indicating that most of the nanocrystals are single crystalline with nearly perfect lattice. HRTEM investigations also confirm the excellent crystallinity of annealed CoPt<sub>3</sub> nanocrystals (Figure 3.5, *insets* and Figure 3.6). Nanocrystals are well separated on

### 3. The mechanism of nucleation and growth of $\text{CoPt}_3$ nanocrystals

TEM grid and exhibit lattice fringes without stacking faults.  $\text{CoPt}_3$  nanocrystals larger than  $\sim 7$  nm usually exhibit facets of a cube-like shape.

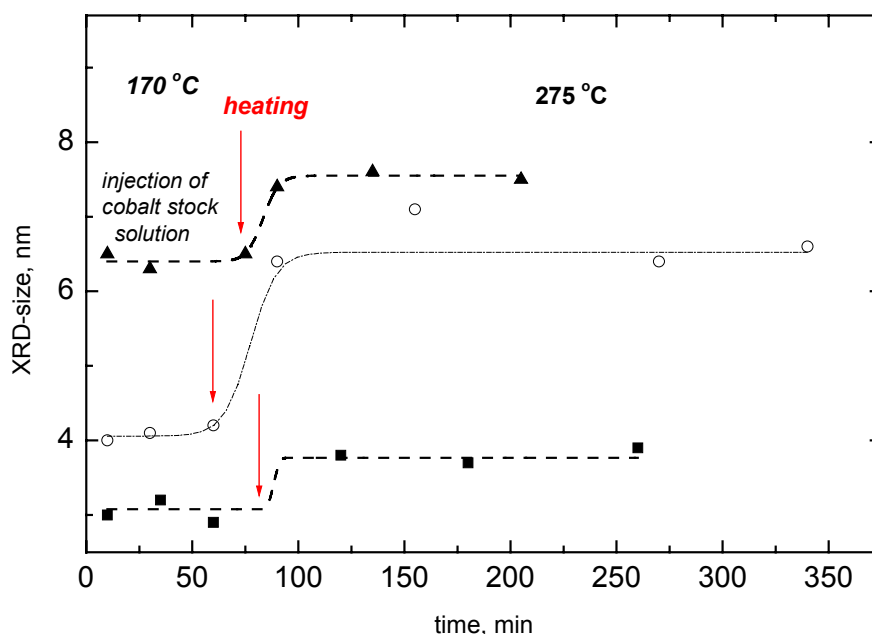


**Figure 3.3.** Evolution of the XRD size of  $\text{CoPt}_3$  nanocrystals prepared by injection of the cobalt stock solution at  $170^\circ\text{C}$  and subsequent annealing at  $\sim 275^\circ\text{C}$ . The curves correspond to the  $\text{CoPt}_3$  nanocrystal prepared in presence of different amounts of ACA. Molar ratio of  $\text{Pt} : \text{Co} : \text{ACA}$  are  $1 : 3 : 1$  (■);  $1 : 3 : 2$  (○) and  $1 : 3 : 6$  (▲).

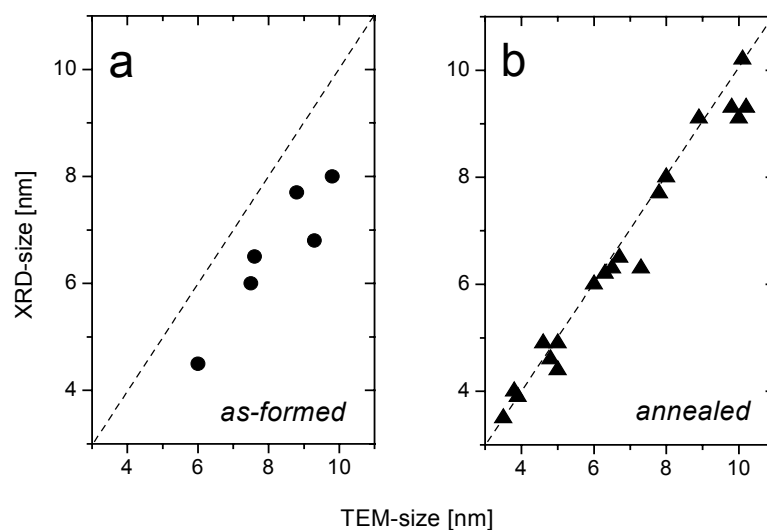


**Figure 3.4.** Comparison of the XRD- and TEM-sizes before and after annealing showing the influence of the annealing procedure on the crystallinity of  $\text{CoPt}_3$  nanoparticles.

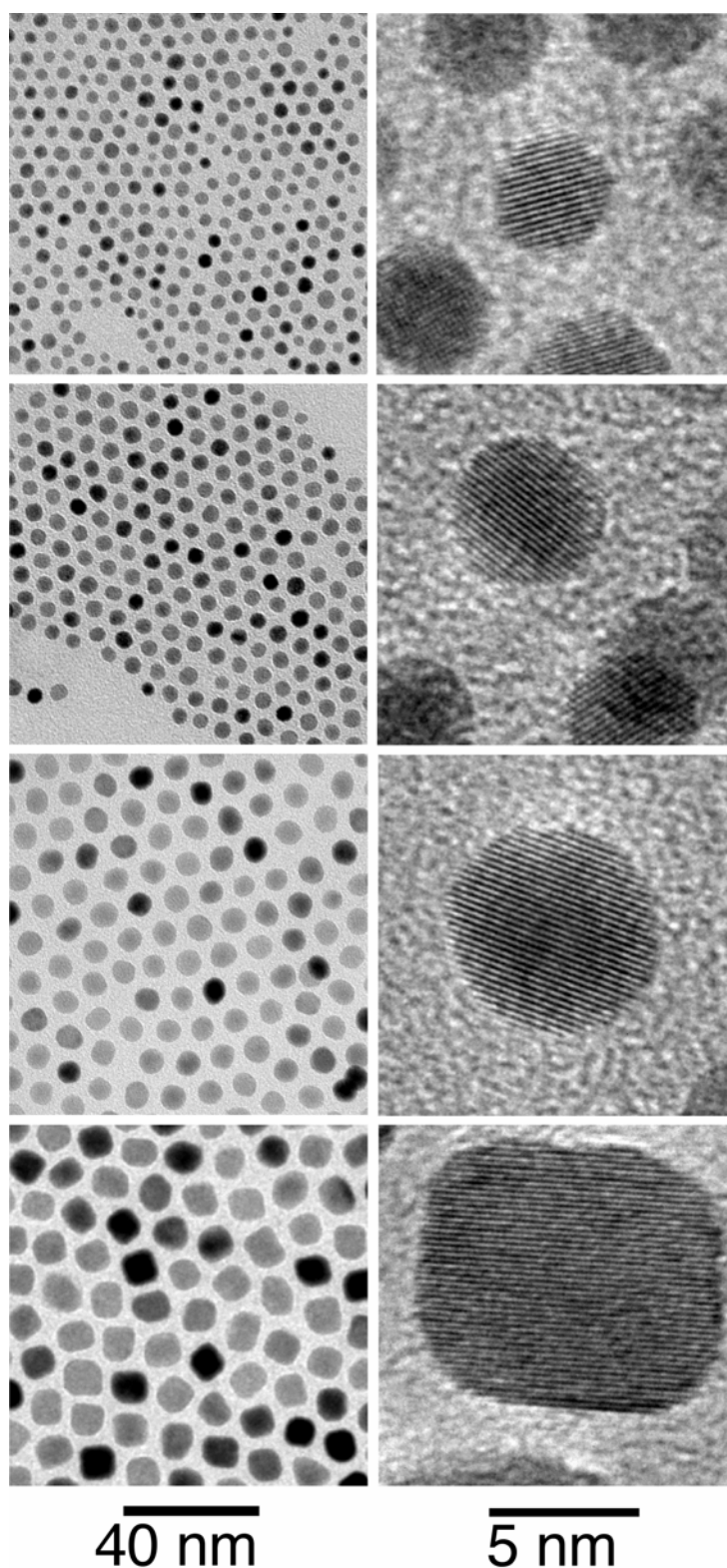


**Figure 3.5.** TEM and HRTEM images showing the effect of the reaction temperature on the mean size and size distribution of 3.7 nm, 4.9 nm, 6.3 nm and 9.3 nm  $\text{CoPt}_3$  nanocrystals prepared at 220, 200, 170 and 145 °C. The molar ratio of Pt : Co : ACA is 1 : 3 : 6 for all samples.

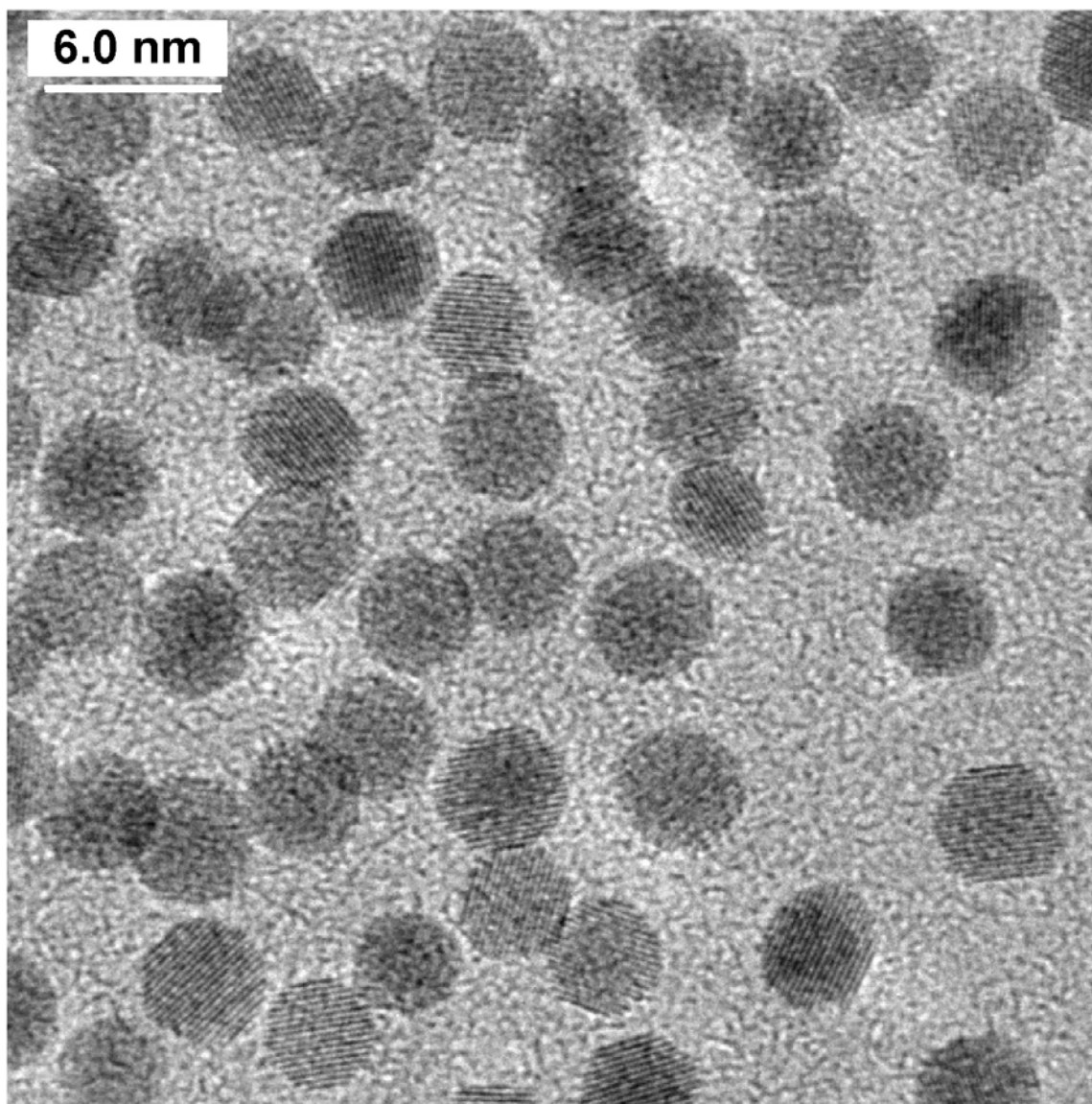


**Figure 3.6.** *An HRTEM image of annealed 4 nm CoPt<sub>3</sub> nanocrystals. Note that almost all nanocrystals display the lattice fringes without stacking faults and other defects.*

In order to better understand the processes of formation and growth of CoPt<sub>3</sub> nanocrystals we investigated the influence of the experimental conditions on the properties of the nanocrystals formed.

*3.2.1. Effect of the injection temperature and concentration of the stabilising agent (1-adamantanecarboxylic acid).*

In the presence of hexadecanediol the solution of Pt(acac)<sub>2</sub> in the HDA-ACA is stable over a wide region of temperatures and starts to decompose only above ~220°C. However, injection of the Co<sub>2</sub>(CO)<sub>8</sub> stock solution initiates a decomposition of Pt(acac)<sub>2</sub> already above

### 3. The mechanism of nucleation and growth of $\text{CoPt}_3$ nanocrystals

$\sim 130^\circ\text{C}$ . The formation and growth of  $\text{CoPt}_3$  nanocrystals was investigated at different temperatures. Figure 3.7a shows how the final size of the  $\text{CoPt}_3$  nanocrystal depends on the reaction temperature. An increase of the temperature from  $145^\circ\text{C}$  to  $225^\circ\text{C}$  allows to decrease the average final size from  $\sim 10$  nm to 3 nm, i.e. permits the preparation of nanocrystals in a wide range of sizes. Subsequent annealing of the nanocrystals at  $275\text{--}285^\circ\text{C}$  results in perfectly crystalline particles with nearly identical TEM and XRD sizes, as given above (Figures 3.4b, 3.5 and 3.6).

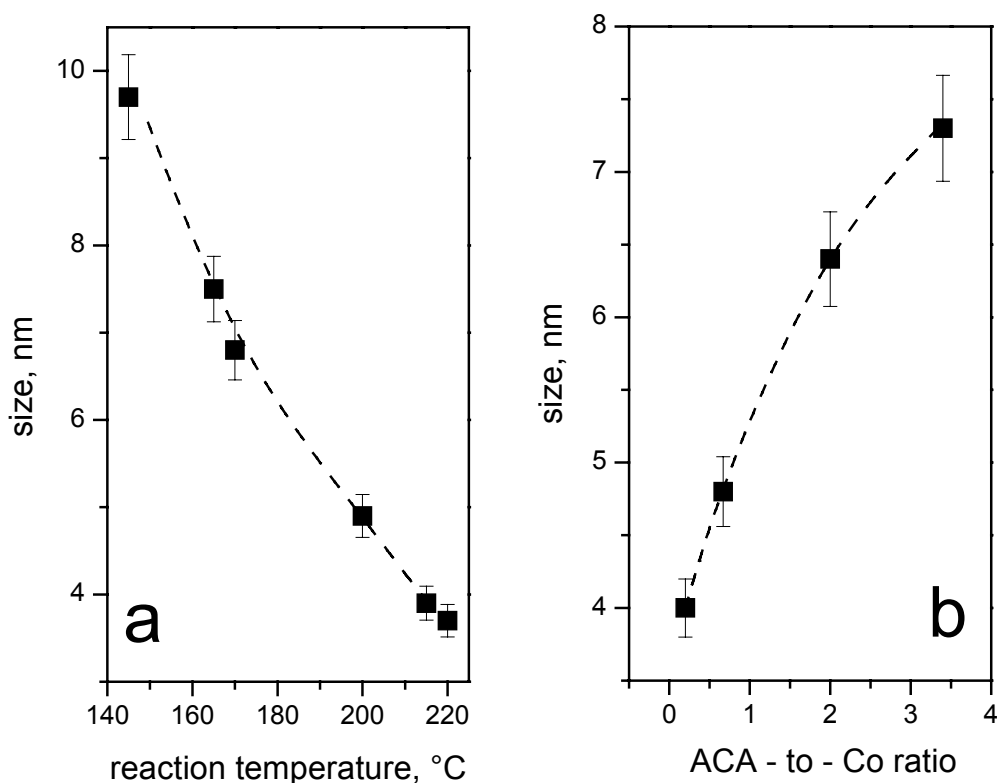


**Figure 3.7.** (a) *Dependence of  $\text{CoPt}_3$  nanocrystals size on the reaction temperature. Molar ratio of Pt : Co : ACA is 1 : 3 : 6;* (b) *Influence of initial amount of the stabilizing agent (ACA) on the nanocrystals size.*

### 3. The mechanism of nucleation and growth of CoPt<sub>3</sub> nanocrystals

ACA or 1-adamantaneacetic acid are most appropriate stabilisers to synthesise CoPt<sub>3</sub> nanocrystals of high quality [8]. The unique role of these extremely bulky stabilisers\* in the synthesis of CoPt<sub>3</sub> nanocrystals was discussed in *Chapter 2*. The major influence of ACA on the formation and stabilisation of CoPt<sub>3</sub> nanocrystals is evident from the drastic influence of the initial ACA concentration on the nanocrystal size. An increase of the initial concentration of ACA results in an increase of the average nanocrystal size (Figure 3.7b). Thus, a variation of the concentration of ACA in the crude solution provides an easy and efficient way to control the size of CoPt<sub>3</sub> nanocrystals.

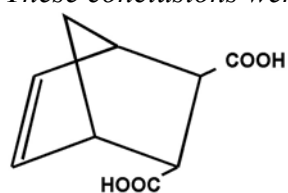
#### 3.2.3. Effect of the ratio between Co and Pt precursor.

In the next series of experiments we varied the initial concentrations of Co and Pt precursors and kept both the reaction temperature and the concentrations of HDA and ACA constant. Variation of the ratio between Co and Pt precursors does not change the composition of the nanocrystals. A Co-to-Pt ratio very close to 1 : 3 was observed for all nanocrystal samples.

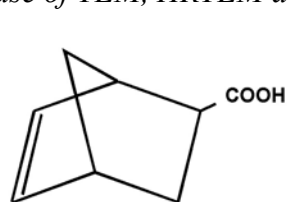
In the reaction we always used some excess of the Co-precursor (with respect to the 1-to-3 ratio in CoPt<sub>3</sub> phase) in order to prevent the formation of bulk Pt (*Experimental Section, Table ES.2*). Quantitative description of all processes occurring inside the reaction vessel during the nucleation and growth of CoPt<sub>3</sub> nanocrystals is rather complex. Note that both, Co and Pt precursors, compete for the finite amount of ACA and that both can be present in solution in different molecular forms. Therefore, in order to investigate the influence of the

---

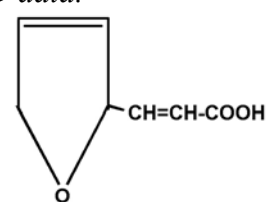
\* We have also investigated the possibility of using of other bulky stabilisers. The graphical formulas of these stabilisers are given below. In the case of nanocrystals prepared in the presence of 5-nonbornen-2-endo,3-exo-dicarboxylic acid or 5-nonbornen-2-carboxylic acid the content of platinum was higher as compared with the formula CoPt<sub>3</sub>. The use of  $\beta$ -(2-furyl-acryl acid) lead to the formation of CoPt<sub>3</sub> nanocrystals. However, probably because of not sufficient stabilisation of cobalt precursor by these stabilisers, the excess of cobalt precursor in the reaction mixture resulted in the formation of core-shell particles, where core is cobalt-platinum alloy and shell is almost amorphous cobalt. Also the size distribution of as-prepared nanoparticles was significantly broader as compared with the size distribution of CoPt<sub>3</sub> nanoparticles prepared under the same reaction conditions in the presence of ACA. These conclusions were reached on the base of TEM, HRTEM and XRD data.



5-nonbornen-2-endo,3-exo-dicarboxylic acid



5-nonbornen-2-carboxylic acid



$\beta$ -(2-furyl-acryl acid)

### 3. The mechanism of nucleation and growth of $\text{CoPt}_3$ nanocrystals

precursor ratio on the synthesis of  $\text{CoPt}_3$  nanocrystals, we performed two series of experiments. In the first one we varied the initial concentration of the Co-precursor whereas temperature and amounts of all other components were kept constant. In the second series of experiments we varied in the same manner the initial concentration of the Pt-precursor.

An increase of the concentration of cobalt (or an increase of the Co-to-Pt ratio) in the reaction mixture resulted in a decrease of the particle size (Figure 3.8a). A similar behavior was observed for different reaction temperatures allowing us to tune the mean particle size from  $\sim 3$  to 18 nm. Similarly, an increase of concentration of the Pt precursor results in an increase of the size of  $\text{CoPt}_3$  nanocrystals (Figure 3.8b).

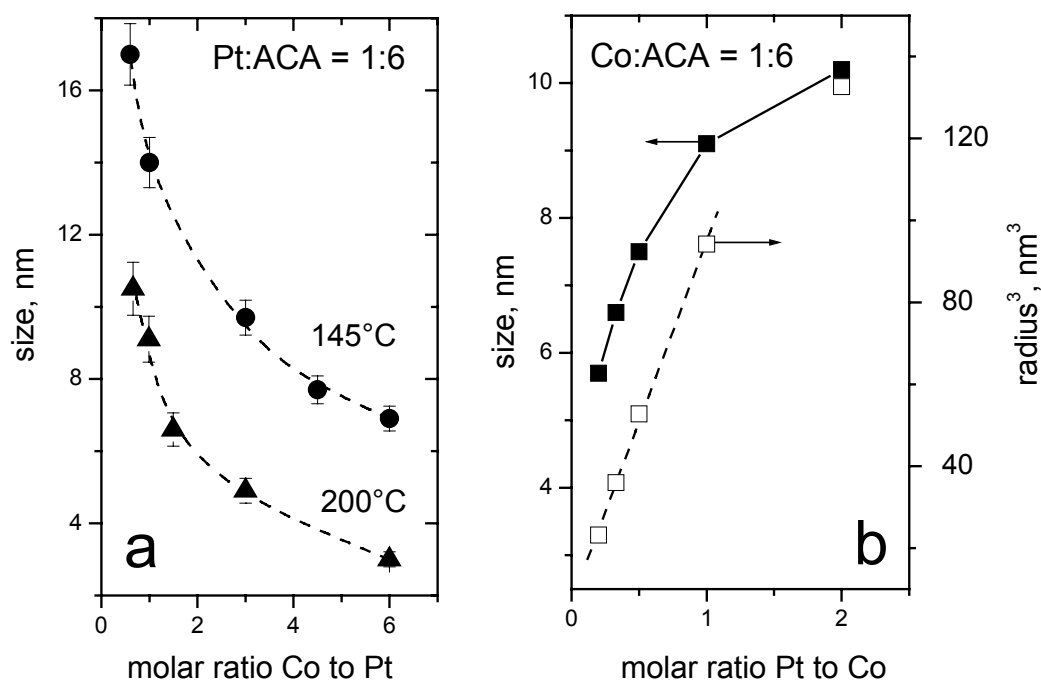


**Figure 3.8** (a) Influence of the molar ratio between Co and Pt precursors on the nanocrystal size at different reaction temperatures. (b) Influence of the molar ratio between Pt and Co precursors on the nanocrystal size for the reaction temperature 200 °C (■) and the same data plotted in the coordinates of cube of the particle radius vs. initial ration of Pt and Co precursors (□). After the nanocrystal formation all samples were annealed at  $\sim 270$ – $280$  °C for  $\sim 1$ h. The amount of ACA was constant (0.25 g) for all experiments.

#### *3.2.3. Size distribution of the CoPt<sub>3</sub> nanocrystals during growth.*

We studied the size distribution of CoPt<sub>3</sub> nanocrystals grown in the HDA-ACA mixture. Information about particle size distribution was obtained from statistical evaluation of all nanocrystals in a chosen area of a TEM micrograph (~1500-2000 particles) or from small-angle X-ray scattering (SAXS) data by means of the indirect transformation method [10, 11]. The latter averages over a huge number of nanocrystals whereas processing of the TEM images requires some care to avoid artifacts due to possible spatial separation of differently sized particles on the TEM grid. Figure 3.9a shows SAXS patterns for two samples of as-prepared CoPt<sub>3</sub> nanocrystals with mean sizes between ~4 and 10 nm. The nanocrystal size was adjusted by proper choice of the reaction temperature (215°C and 145°C). Figures 3.9b and 3.9c show the particle size distribution functions of as-prepared ~4 nm CoPt<sub>3</sub> nanocrystals as obtained from the SAXS and TEM data, correspondingly. The SAXS data evidence that small CoPt<sub>3</sub> nanocrystals form stable suspensions with single-particle population [12,13]. Both SAXS and TEM measurements confirm relatively narrow and nearly symmetric particle size distribution for as-prepared ~4 nm CoPt<sub>3</sub> nanocrystals (Figures 3.9b and 3.9c) whereas a minor deviation (~0.2 nm) between mean sizes estimated by these methods was observed. HRTEM always provided smaller estimates for particle size compared to SAXS, because the size distribution from SAXS is a volume (or mass) distribution, whereas that from microscopy is a number distribution. The difference between volume and number distribution is negligible when the distribution is narrow. However, in broad distributions or in the presence of a few aggregates the bigger particles count visibly more in volume distributions (SAXS) than in number distributions (TEM). Also note that the nanocrystal capping molecules ACA and HDA have an electron density similar to that of the solvent (hexane). Therefore the SAXS-sizes account only for the inorganic core in the nanocrystal.

In the case of ~10 nm CoPt<sub>3</sub> nanocrystals the SAXS size distribution curve was superimposed by a peak corresponding to the single particle population and a tail in the large size region (Figure 3.9d). The TEM investigations of the same sample revealed a symmetric size distribution curve without any features around 12 - 13 nm (Figure 3.9e). This allows us to assume partial aggregation of ~10 nm CoPt<sub>3</sub> in hexane at room temperature [12]. Long-term stability of the colloidal solutions as well as the absence of agglomerates in TEM images provides evidence that the aggregation is reversible. Relatively small attractive interactions between ~10 nm CoPt<sub>3</sub> nanocrystals are also evident from the Guinier plots with a concave curvature of the scattered X-ray intensity near the origin [13]. Dilution of the colloidal

solutions increases the particle aggregation whereas addition of small amount of HDA allows recovering single-particle population. Another factor resulting in some discrepancy between TEM and SAXS data might be shape anisotropy observed in TEM and HRTEM images for large CoPt<sub>3</sub> nanocrystals (Figure 3.5) which distorts the spherical particle approximation used in our calculations.

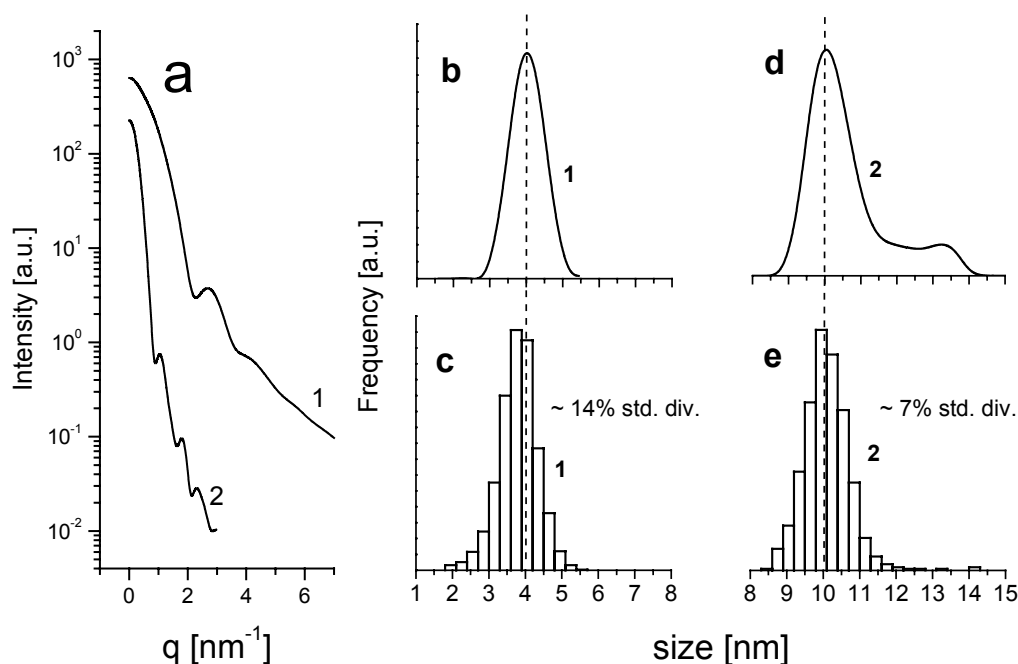


**Figure 3.9.** (a) The angular dependence of scattered X-ray intensity (SAXS) from two samples of as-prepared CoPt<sub>3</sub> nanocrystals with mean size (1) ~4 nm and (2) ~10 nm. (b) and (d) Particle volume fraction vs. size curves calculated from the SAXS data shown in part (a). (c) and (e) Particle size distribution histograms estimated for the same samples from TEM images.

The absolute width of particle size distribution is nearly constant for both, the ~4 nm and the ~10 nm samples (Figure 3.9). This means that the relative size distribution of as-prepared ~4 nm CoPt<sub>3</sub> nanocrystals is much broader as compared to that of ~10 nm nanocrystals (~14% and ~7% of standard deviation, correspondingly). The width of the size distribution for as-prepared CoPt<sub>3</sub> nanocrystals was plotted against the mean particle size for samples with different average size (Figure 3.10). The general tendency is a narrowing of the size distribution with increasing particle size. This behaviour was observed for all samples irrespective of the method of size control. The same trend is seen in the TEM and HRTEM

images (Figure 3.5). Post-preparative size-selective precipitation allows further narrowing of the nanocrystal size distribution.

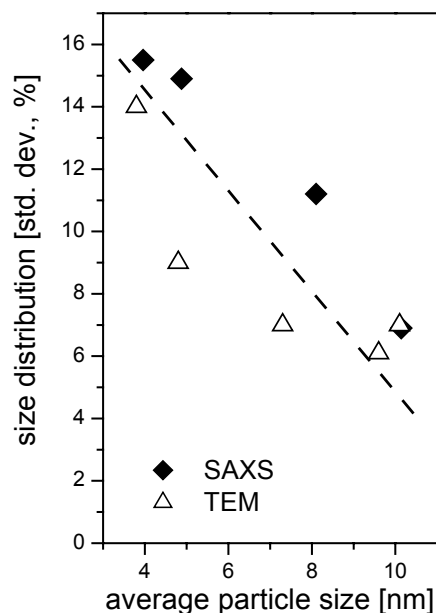


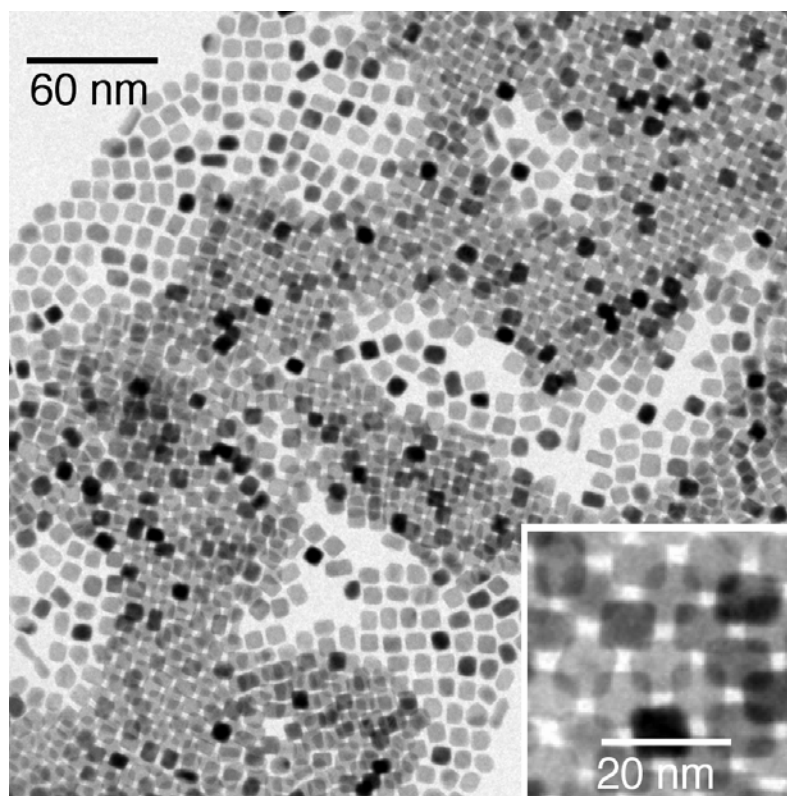
**Figure 3.10.** Standard deviation of the particle size distributions observed for as-prepared  $\text{CoPt}_3$  nanocrystals of different average size.

#### 3.2.4. Faceting of $\text{CoPt}_3$ nanocrystals.

$\text{CoPt}_3$  nanocrystals with sizes smaller than  $\sim 7$  nm are usually spherical (Figures 3.5 and 3.6). However, further increase of the nanocrystal size results in a rather abrupt transition from spherical to cubic, truncated cubic or, in some cases, plate-like shapes as shown in Figure 3.11. It was also observed that annealing at  $\sim 275^\circ\text{C}$  results in smoothing of the edges of cubic nanocrystals formed at  $145^\circ\text{C}$  (cf. Figures 3.5d and 3.11). Each side of cubic crystal lattices corresponds to the  $[100]$  direction of the *fcc* nanocrystal lattice. Cubic particles can be formed if the growth rate in the  $[111]$  direction is much higher than that in the  $[100]$  direction [14]. The ratio between growth rates in different directions can be varied by specific adsorption of organic surfactant onto particular crystallographic facets inhibiting the growth of a particular crystallographic direction [15]. Recently, this type of shape control has been demonstrated for the colloidal synthesis of CdSe [16], PbS [17], Pt [18], and Co [15, 19] nanocrystals. However, the phenomena responsible for the abrupt transition from spherical to

faceted particle during growth in a colloidal solution are not clear and require further investigation.

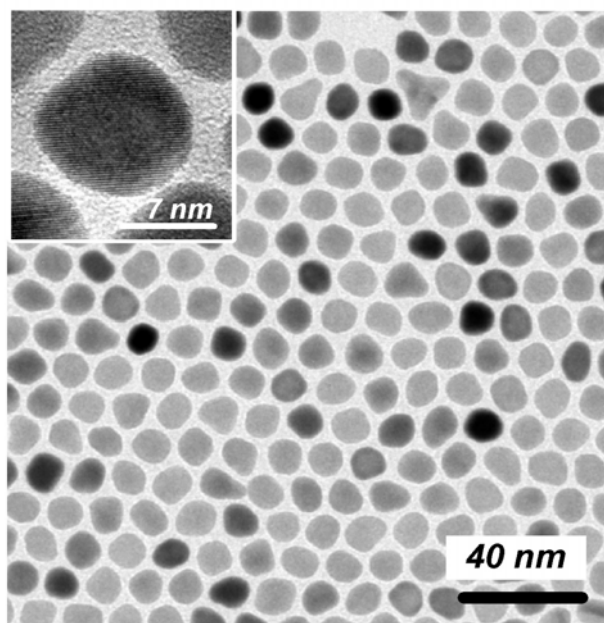
Monodisperse nanocrystals can self-assemble into 2D and 3D superlattices [2, 20-22] where individual nanocrystals play the role of building blocks (*Chapter 6*). Engineering of the nanocrystal shape should allow creating new kinds of superstructures.



---

**Figure 3.11.** TEM overview image of faceted CoPt<sub>3</sub> nanocrystals prepared at 145°C. Molar ratio of Pt : Co : ACA was 1 : 3 : 6.

Annealing of faceted CoPt<sub>3</sub> nanocrystals at ~270 during ~40 min – 2 h results in the smoothing of relatively sharp facets of nanoparticles. Also the tendency of smoothing of nanocrystal surfaces was clearly seen in the case of CoPt<sub>3</sub> nanocrystals prepared at higher reaction temperatures. Figure 3.12 demonstrates CoPt<sub>3</sub> nanocrystals nearly of the same size (~10.1 nm) prepared by injection of relevant amount of cobalt stock solution into the reaction mixture at 200 °C, the surface of those, however, is much smoother. The faceting of crystals is conditioned by the aspiration of the system to minimise its energy. At higher temperatures the system possesses the higher energy and as a result the nanoparticles prepared at higher temperature can be less faceted.



---

**Figure 3.12.** TEM overview and HRTEM images (inset) of  $\sim 10.2$  nm  $\text{CoPt}_3$  nanocrystals prepared at  $200^\circ\text{C}$ . Molar ratio of Pt : Co : ACA was 1 : 0.6 : 6.

### 3.3. The role of the nucleation rate in the size control of $\text{CoPt}_3$ nanocrystals

The synthesis of colloidal crystalline particles from a homogeneous solution involves two consecutive stages: formation of nuclei with sizes larger than the critical one (nucleation stage) and growth of these nuclei (growth stage) [23]. The latter can occur *via* the following mechanisms: (i) growth consuming molecular precursors from surrounding solution; (ii) Ostwald ripening or coarsening when larger particles grow at the expense of dissolving smaller ones [24], and (iii) fusion of several particles (oriented attachment) [25].

Colloidal metal nanocrystals usually grow *via* the first mechanism, i.e. consuming dissolved molecular species (monomers), whereas neither Ostwald ripening nor oriented attachment is observed [8, 12, 18, 26-32]. Ostwald ripening can occur only if the addition of a monomer to a nanocrystal is a reversible process, i.e., a nanocrystal can both consume or release molecular species. In this case smaller particles which have higher chemical potential evolve monomer and dissolve whereas larger particles consume monomer and grow. This behavior was observed for many semiconductor colloids and is usually used for tuning the mean particle size [2, 21]. In contrast, the transformation of molecular precursors to metal

particles is either irreversible or the equilibrium between monomer and solid is strongly shifted towards the solid.

In the absence of Ostwald ripening it is rather difficult to tune the particle size in a predictable and reproducible manner. Let us consider possible ways of size control on the example of CoPt<sub>3</sub> nanocrystals:

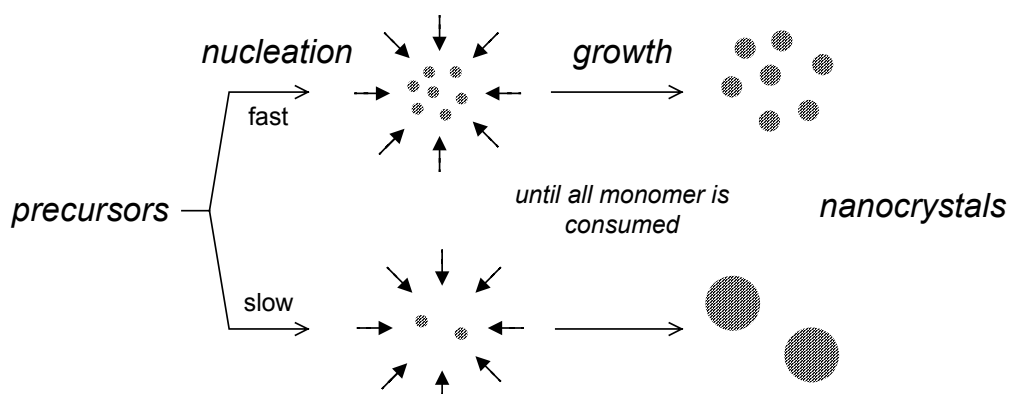
It is principally possible to inject the cobalt stock solution at a low temperature and quench the reaction at an early stage when the nanocrystals are small. However, this approach has serious drawbacks: (i) the particles exhibit poor crystallinity at an early stage of the reaction (Figures 3.2 and 3.3); (ii) only a small part of the precursors is converted to the nanocrystals; (iii) in the absence of any means suitable for express monitoring of the particle size (like the color changing in solutions of growing semiconductor nanocrystals) it is difficult to quench the reaction exactly at the desired stage.

Another approach to size tuning could be additional injections of precursors into the reaction mixture [8, 31]. However, in this case nucleation of new particles usually competes with growth of already existing ones (*Chapter 2*). Moreover, large CoPt<sub>3</sub> and FePt nanocrystals prepared by additional injections are irregularly shaped and possess various lattice defects [8, 32]. Therefore, more easy and facile ways of size-tuning are strongly desirable for CoPt<sub>3</sub> and other metal nanocrystals.

In the case of CoPt<sub>3</sub> nanocrystals it was found that an increase in the concentration of the stabilizing agent resulted in the increase of the nanocrystal size (Figure 3.7b). This is rather surprising because the conventional routes for Au and Ag nanocrystals usually exhibit opposite behaviour [3]. Also a higher concentration of stabilising agent is commonly used to prepare smaller semiconductor particles. The size dependence of CoPt<sub>3</sub> nanocrystals on the concentration of ACA as well as the number of other experimental data observed for the synthesis CoPt<sub>3</sub> (Figures 3.7 and 3.8) and some other metal nanocrystals can be understood when we consider some peculiarities of the nanocrystal nucleation process. In the absence of Ostwald ripening and oriented attachment particles can grow only until all molecular precursors are consumed. The total amount of consumed monomers (as well as the total volume of formed particles) is constant. In this case the balance between the rates of nucleation and growth should affect the final particle size as illustrated in Scheme 3.1. Fast nucleation provides high particle concentration and yields small particles. Slow nucleation provides low concentration of seeds consuming the same amount of monomer and results in large particles. Thus, a control over the nucleation rate allows tuning of the final nanocrystal size in the absence of Ostwald ripening. The screening of experimental conditions

### 3. The mechanism of nucleation and growth of CoPt<sub>3</sub> nanocrystals

demonstrates the possibility to vary the size of CoPt<sub>3</sub> nanocrystals in a wide range (Figures 3.7 and 3.8).



**Scheme 3.1.** Schematic representation of nanocrystal synthesis in the absence of the Ostwald ripening stage.

To date, almost no reliable information about microscopic mechanism and kinetics of nucleation of real colloidal nanoparticles is available [34]. However, there are some general features inherent to the homogeneous nucleation phenomenon. The classical nucleation theory gives the following expression for the crystal nucleation rate per unit volume [23, 34]:

$$J_N = B_N \exp\left(-\frac{\Delta G^N}{RT}\right) \quad (1)$$

$$\Delta G^N = \frac{16\pi\gamma^3 V_m^2}{3|\Delta\mu|^2} \quad (2)$$

where  $\Delta G^N$  is the activation energy for homogeneous nucleation;  $\gamma$  is the surface tension;  $V_m$  is the molar volume of solid;  $\Delta\mu$  ( $<0$ ) is the difference in chemical potential between solid and monomers;  $B_N$  is the pre-exponential factor depending on many parameters such as desolvation of species, etc.

*Effect of the reaction temperature.* Figure 3.7a shows the decrease of CoPt<sub>3</sub> nanocrystal size with increasing the reaction temperature demonstrating that the nucleation rate raises with temperature faster than the growth rate. Usually, the activation energy for the nucleation process  $\Delta G^N$  is much higher than that for particle growth [23]. It means that the nucleation rate is much more sensitive to changes in temperature as compared to the growth rate. In fact, this situation is widely used in the organometallic synthesis of semiconductor nanocrystals:

### 3. The mechanism of nucleation and growth of CoPt<sub>3</sub> nanocrystals

the “hot-injection” technique allows temporal separation of nucleation and growth stages because the homogeneous nucleation can be completely quenched via a small temperature drop whereas the growth rate does not undergo such drastic changes [2,6]. In other words, variation of the reaction temperature affects the nucleation stronger than the growth and, therefore, can be used to adjust the balance between nucleation and growth rates. At higher reaction temperature more nuclei are formed and, according to the Scheme 3.1, the final particle size is smaller. In combination with subsequent annealing of the nanocrystal lattice, variation of the reaction temperature provides a powerful tool for size control which can be used to prepare different high quality metal nanocrystals.

The nucleation rate ( $\frac{dC_{nuclei}}{dt}$ ) characterises the rate of changing of the concentration of nuclei with time. If the nucleation time is kept constant the concentration of nuclei can be taken as a measure of the nucleation rate. The narrow size distribution of the as-prepared nanocrystals provides strong evidence of temporal separation of the nucleation and growth stages. In the absence of the Ostwald ripening the concentration of nanoparticles remains constant during the growth stage (Scheme 3.1). In this case the final mass of the particles is determined by the number of nuclei and the overall concentration of monomer. If the latter is also kept constant the final size (mass) of the particle can be taken as a measure for the nucleation rate. In a corresponding set of experiments the nanocrystal grew until all molecular precursor is consumed and the total amount of nanocrystals ( $M$ ) obtained at different temperatures was nearly constant. In this case the concentration of nuclei and, in turn, the nucleation rate can be expressed as a ratio between the overall weight of all formed nanocrystals and the mass of a single particle ( $m$ ):  $J_N \propto \frac{M}{m}$ . The mass of a spherical particle can be easily expressed as  $m = 4\rho\pi r^3 / 3$  where  $\rho$  - is density and  $r$  is the nanoparticle radius. Therefore, the nucleation rate should be inversely proportional to cube of particle radius:  $J_N \propto \frac{3M}{4\rho\pi r^3} \propto const * r^{-3}$  or, in other words,  $J_N \propto r^{-3}$ .

This assumption allows us to calculate the activation energy for the nucleation process. We measured the final size of the particles as a function of the injection temperature. The injection temperature ( $T_{inj}$ ) is the temperature at which the nucleation occurs and thus may be considered as the nucleation temperature. The equation (1) can be linearised in the coordinates  $\ln(J_N)$  vs.  $1/T_{inj}$ :

$$\ln(J_N) = \ln(B_N) - \left( \frac{\Delta G^N}{R} \right) * \frac{1}{T_{inj}} \quad (3)$$

### 3. The mechanism of nucleation and growth of CoPt<sub>3</sub> nanocrystals

According equation (3) we obtain the activation energy for nucleation in a  $\ln(r^{-3})$  versus  $1/T_{inj}$  plot, which is shown in Figure 3.13. The expected linear relationship is observed and from the slope  $\Delta G^N \approx 79.8 \text{ kJ mol}^{-1}$  is found.

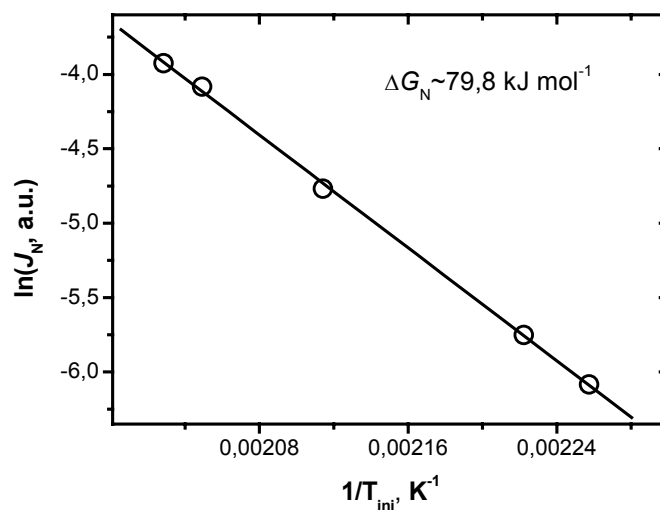


**Figure 3.13.** Dependence of the nucleation rate on the injection temperature.

*Effect of the concentration of the stabilising agent.* The nucleation rate can also be adjusted via the parameter  $\Delta\mu$  which affects both  $\Delta G^N$  and  $B_N$  in the equations (1) and (2) [23]. The parameter  $\Delta\mu$  describing the difference in chemical potential between solid and monomers rises with increase of monomer oversaturation (the simplest relation is  $\Delta\mu = RT \ln S$ , where the oversaturation  $S$  is the ratio between the current and the equilibrium concentration of monomer [23]). Molecules like ACA, TOPO, TOP, amines, etc. used to passivate the surface of growing nanocrystals can also form stable complexes with individual metal atoms of a molecular precursor (monomer). The formation of such complex precedes the particle nucleation process. For instance, the platinum precursor ( $\text{Pt}(\text{acac})_2$ ) decomposes in the HDA - diphenyl ether - 1,2-hexadecandiol mixture at  $\sim 130^\circ\text{C}$ . Addition of ACA in the amount commonly used for the synthesis of CoPt<sub>3</sub> nanocrystals increases the decomposition temperature up to  $\sim 220^\circ\text{C}$ . A similar behaviour was also observed for the cobalt precursor: addition of ACA drastically enhances the stability of the cobalt carbonyl solution against thermodecomposition. Formation of a stabilising agent – monomer complex increases the equilibrium concentration of the monomer, i.e. it decreases the monomer oversaturation as well as the parameter  $\Delta\mu$  in the Equation 2. Therefore, an increase of the concentration of a stabilizing agent is expected to suppress nucleation and, as a consequence, yields larger nanocrystals (Scheme 3.1). These predictions are in agreement with the behaviour of CoPt<sub>3</sub> nanocrystals: higher initial concentrations of ACA results in a considerable increase of the

average nanocrystal size (Figure 3.7b). In fact, dependencies similar to that shown in Figure 3.7b for CoPt<sub>3</sub> nanocrystals were recently reported for  $\gamma$ -Fe<sub>2</sub>O<sub>3</sub> [27], prepared via oxidation of pre-formed iron seeds and for Pt nanocrystals prepared *via* a relatively “hot” synthesis [26]. However thermodynamic model of nanocrystal synthesis demonstrates decrease of the particle size with the increase of the stabiliser-to-precursor ratio [3].

*Dependence of the nucleation rate on the ratio between Co and Pt precursors.* We varied the initial concentrations of Co and Pt precursors keeping all other parameters constant. As it has been discussed above, the final nanocrystal size depends mainly on the balance between the particle nucleation and growth rates. Probably, one has to apply this approach to the inverse task, i.e. use the final size of the CoPt<sub>3</sub> nanocrystals as a probe of the balance between nucleation and growth rates.

An increase of the concentration of cobalt precursor results in a decrease of the particle size (Figure 3.8a). In accord with our model (Scheme 3.1) one can expect the increasing of the nucleation rate for CoPt<sub>3</sub> nanocrystals. For high concentration of cobalt precursor more nucleation seeds are generated and as a result the CoPt<sub>3</sub> nanocrystals of smaller sizes are formed.

An increase of the concentration of the Pt precursor results in an increase of the size of CoPt<sub>3</sub> nanocrystals (Figure 3.8b). We always used some excess of the Co-precursor with respect to the 1 : 3 ratio given by the CoPt<sub>3</sub> formula. Therefore, the nanocrystals should grow until all Pt is consumed. The increase of the particle size results from the termination of the particle growth at a later stage. Surprisingly, the linear dependence of cube of particle size ( $\sim$ particle volume) on the concentration of the Pt precursor was observed in the wide range of Pt-to-Co ratios (Figure 3.8b). This provides evidence that the number of formed nuclei is constant and does not depend on the initial concentration of Pt or, in other words, the nucleation rate of CoPt<sub>3</sub> nanocrystals has 0-th kinetic order with respect to Pt(acac)<sub>2</sub>. A deviation from this behaviour was observed only in the case of high platinum concentrations (Figure 3.8b, *dash line*) and can be explained by some increase of the number of formed nuclei at very high concentration of the Pt-precursor. As mentioned above, ACA can form complexes both with cobalt and platinum precursors. When the concentration of the Pt-precursor is very high, a considerable amount of ACA is consumed by platinum, and, therefore, less amount of ACA is available for the stabilisation of the Co-precursor. As a result, the nucleation rate can slightly vary with the concentration of the Pt-precursor even if it does not directly participate in the nucleation process (see below).

We also studied the influence of the nature of the cobalt and platinum precursors on the final size of CoPt<sub>3</sub> nanocrystals. If cobalt acetylacetonate (Co(acac)<sub>2</sub>) is injected into the reaction mixture at 170 °C instead of Co<sub>2</sub>(CO)<sub>8</sub> the size of CoPt<sub>3</sub> nanocrystals (~11.5 nm) was considerably larger than the size of the nanocrystals prepared according the conventional method (~6.2 nm). Probably, in the case of more stable Co(acac)<sub>2</sub> the nucleation rate was considerably slower. On the other hand, when we performed the synthesis of CoPt<sub>3</sub> nanocrystals at 170°C in the absence of 1,2-hexadecandiol which affects mainly the reduction rate of Pt(acac)<sub>2</sub> [31], the mean nanocrystal size (~6.3 nm, Figure 3.14) was nearly equal to that of nanocrystals prepared via the conventional method (6.2 nm). This seems to be another strong hint that the platinum precursor does not determine the nanocrystal nucleation rate.

*Size distribution of the CoPt<sub>3</sub> nanocrystals during growth.* Progressive narrowing of the particle size distribution with increasing their mean size was observed for CoPt<sub>3</sub> nanocrystals (Figures 3.5, 3.9, 3.10). The size distribution of colloidal nanoparticles was a subject of many investigations.[23, 24, 34] Thus, if nanoparticles grow via Ostwald ripening, the particle size distribution tends to the unique one irrespective of the initial shape of the size distribution [24, 35]. On the other hand, if nanocrystals grow consuming molecular precursors from surrounding solution, the size of smaller particles increases faster than that of the larger ones. In this case an increase of the mean particle size is accompanied by a narrowing of the initial particle size distribution, which keeps nearly symmetric during particle growth [24]. This growth regime was recently observed for ensembles of CdSe nanocrystals and was called “focusing” of size distribution [34]. As was discussed above, CoPt<sub>3</sub> nanocrystals can grow only by consuming the monomers from solution, i.e., in the “focusing” mode. This explains the observed narrowing of the size distribution with increase of the particle size.

#### **3.4. Discussion of the nucleation mechanism**

It is extremely complex to investigate the microscopic nucleation mechanism. The difficulty originates from basics of the nucleation phenomenon: the bottleneck for determining the nucleation process is the formation of critical nuclei which are the most unstable species with the highest chemical potential in the reaction mixture [33]. As a result, the critical nuclei are present at a concentration so tiny that their structural characteristics cannot be probed by existing methods. Moreover, the phase that nucleates needs not be the one that is thermodynamically stable [36]. This opens up a broad field of speculation about the

### *3. The mechanism of nucleation and growth of CoPt<sub>3</sub> nanocrystals*

peculiarities of the nucleation process in a given system. Probably, the observed independence of the nucleation rate of the concentration of the platinum precursor means that the critical nuclei for CoPt<sub>3</sub> nanocrystals consist only of Co or, in other words, the growth of the nanocrystals starts from the formation of some Co-clusters which serve as seeds for further growth of CoPt<sub>3</sub> particles. In fact, such polynuclear cobalt carbonyl clusters, e.g. Co<sub>4</sub>(CO)<sub>12</sub> and Co<sub>6</sub>(CO)<sub>16</sub>, form as intermediates upon the thermal decomposition of Co<sub>2</sub>(CO)<sub>8</sub> [15].

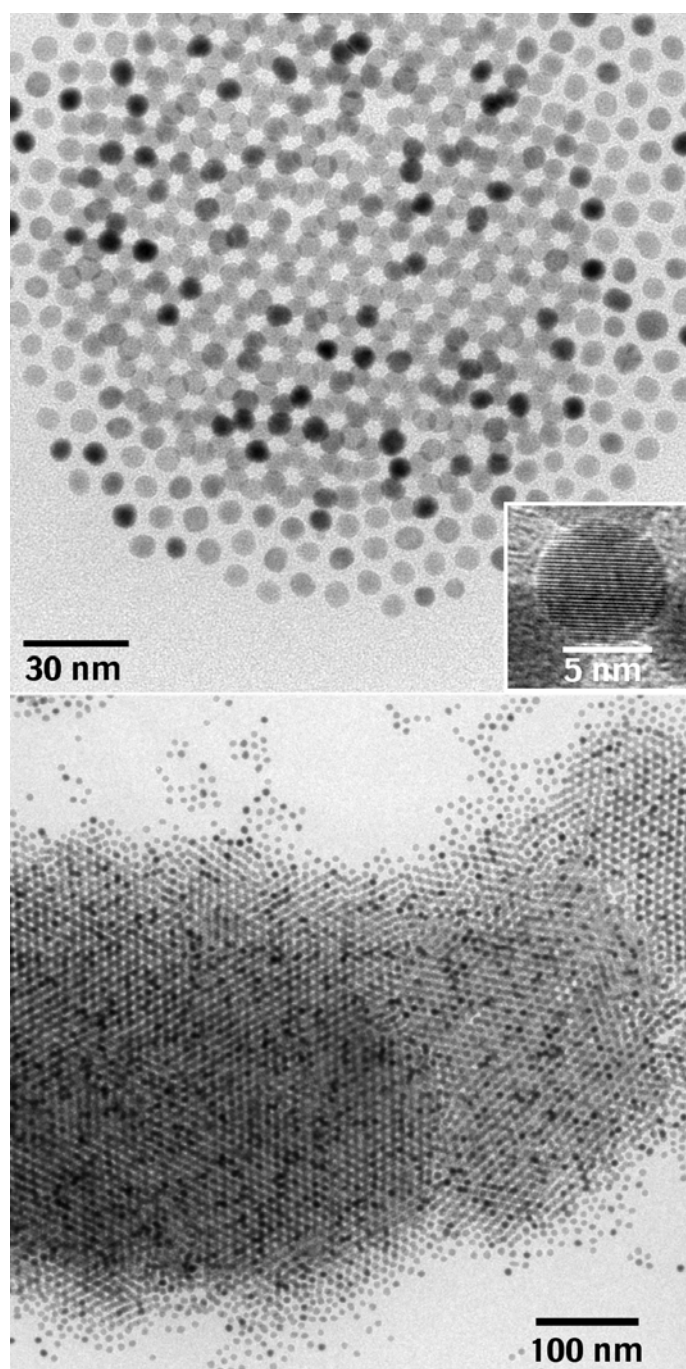
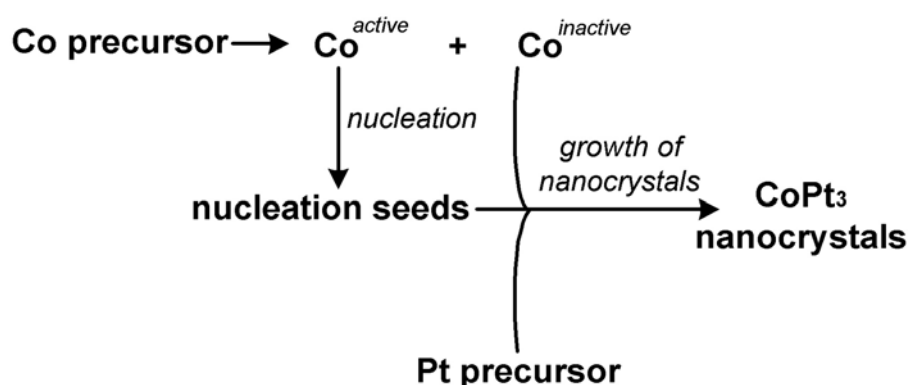


**Figure 3.14.** TEM and HRTEM (inset) images of CoPt<sub>3</sub> nanocrystals prepared without 1,2-hexadecandiol.

### 3. The mechanism of nucleation and growth of CoPt<sub>3</sub> nanocrystals

When the concentration of the cobalt precursor increases, the number of these Co-seeds also increases (smaller CoPt<sub>3</sub> nanocrystals form) whereas a concentration of the platinum precursor does not affect the number of the Co-seeds for further growth of alloy nanoparticles. We assume that after injection of the cobalt stock solution, ACA molecules can complex to cobalt and form stable complexes (Co<sup>inactive</sup>) (Scheme 3.2). “Active” cobalt precursor (Co<sup>active</sup>) forms nucleation seeds (Scheme 3.2) which can further grow consuming both “active” and “inactive” cobalt precursors from the reaction solution. Cobalt precursor complexed by ACA have higher activation energy for nucleation than “free” cobalt precursor (Co<sup>active</sup>). This means that the stable complex of the cobalt precursor (Co<sup>inactive</sup>) is “bad” for the nucleation. However, inactive in the nucleation process stable complexes of cobalt precursor (Co<sup>inactive</sup>) can take part in the growth process.



**Scheme 3.2.** Growth of CoPt<sub>3</sub> nanocrystals.

These our suggestions are base on the following experiments:

*Experiment 1.* All components except Pt(acac)<sub>2</sub> were mixed and heated up to 240 °C. The colour of the reaction mixture changed from pale violet to transparent bright blue. After cooling to ~ 50 °C Pt(acac)<sub>2</sub> was added and the reaction mixture was slowly (~1 °C/min) heated again. At ~230 °C the solution started to change the colour from blue to black (under standard conditions it happens at ~130 °C) which indicated the formation of colloidal nanocrystals. Analysis of XRD data showed 14 nm chemically disordered *fcc* CoPt<sub>3</sub> particles, while the injection of cobalt stock solution into the solution of platinum precursor at 230 °C results in the formation of ~3 nm CoPt<sub>3</sub> particles.

*Experiment 2.* After addition of Pt(acac)<sub>2</sub> to blue solution (see *Exp.1*) the reaction mixture was slowly (~1 °C/min) heated up to 200 °C. ~ 1/10 of the initial amount of Co<sub>2</sub>(CO)<sub>8</sub>

### 3. The mechanism of nucleation and growth of CoPt<sub>3</sub> nanocrystals

was added to the solution. The solution become black immediately. The weight of final product (CoPt<sub>3</sub> nanocrystals) was much smaller than usually. The colour of supernatant solution was bright blue that indicates the non-reacted complex of cobalt with ACA. XRD data showed ~9 nm CoPt<sub>3</sub> crystals while usually injection of cobalt stock solution results in the formation of ~5 nm nanocrystals. This experiment indicates that additional amount of Co<sub>2</sub>(CO)<sub>8</sub> (or at least part of it) is consumed to form nuclei but further growth of nanocrystals can be occurred due to inactive, at least, at the nucleation stage stable complexes of cobalt precursor – Co<sup>inactive</sup>.

So we can assume that properly co-ordinated cobalt Co<sup>inactive</sup> can take part in the growth of nanocrystals, however, it has a too high activation energy to nucleate at temperatures at which Co<sup>active</sup> can form nuclei for further growth of CoPt<sub>3</sub> nanocrystals. In the absence of cobalt precursor the formation of platinum takes place above ~230 °C. Probably, these cobalt nuclei catalyse the precipitation of platinum since in presence of cobalt precursors reduction of platinum happens at significantly lower temperatures (~130 - 140 °C). In the absence of platinum precursors cobalt nuclei are not stable and the equilibrium shifts towards the complexation of cobalt precursor. We can suggest that precipitation of platinum at these nuclei stabilise them and the reaction equilibrium shifts towards the formation of CoPt<sub>3</sub> nanocrystals. The final nanocrystal size was very sensitive to the cobalt precursor. When we replace cobalt carbonyl with cobalt acetylacetonate, injection of cobalt stock solution at 170 °C results in much larger CoPt<sub>3</sub> nanocrystals (~11.5 nm) than those (~6.3 nm) obtained when cobalt carbonyl precursor is used. It can also be considered as a hint that cobalt precursor is responsible for the nucleation stage of the reaction. So our experimental data can be attributed to the growth of CoPt<sub>3</sub> nanocrystals on some Co-seeds. In all cases we have the lack of platinum precursor to avoid the formation of bulk Pt. Thus the growth of CoPt<sub>3</sub> nanocrystals takes place until all platinum precursor is consumed.

The initial cobalt seeds are, probably, some clusters consisting of only several atoms. These seeds after covering with platinum-rich shell can be easily converted into an uniform alloy by mutual diffusion of only several atoms. Such atomic diffusion definitely takes place during the nanocrystal annealing. Also, cobalt seeds can interact with Pt(acac)<sub>2</sub> via transmetalation reaction forming cobalt-platinum alloy [37].

Recently, Ciacchi et al. reported a theoretical investigation of possible pathways for the nucleation of Pt nanocrystals after reduction of Pt(II) salts both in gas phase and in solution [38]. Their calculations as well as the experimental observations by Henglein et al. [39] have ruled out Pt(0) atoms as reaction intermediates. In contrast, reduction of Pt(II) to Pt(I) is

followed by the formation of Pt(I)-Pt(II) dimers. Intriguing, the addition of ions to a growing cluster takes place before their reduction to the metallic state [38]. Probably, Pt(II) can also be attached to a polynuclear cobalt carbonyl cluster (nucleation seed) with further reduction of the entire cluster and followed by iterated reduction/addition mechanism of growth of Co-Pt cluster. Reducing agent in this case can be either  $\alpha$ -diol (1,2-hexadecandiol) or CO-ligands. As was reported by Gogging et al. [40], CO can reduce Pt(II) in solution and, simultaneously, be a ligand stabilizing the Pt(I) intermediate. When we tried to perform the synthesis in the absence of 1,2-hexadecandiol using Pt(acac)<sub>2</sub> and Co(acac)<sub>2</sub> as precursors, no nanocrystals were formed at 170°C. A very interesting and still unanswered question is why the nanocrystals always retain their CoPt<sub>3</sub> stoichiometry in spite of the existence of other stable cobalt-platinum intermetallic compounds? One assumption might be that the constant Co-to-Pt ratio is a result of the complex reduction mechanism of Pt(II) involving interactions with a certain number Co atoms supplying their CO ligands.

### **3.5. Temporal stability and thermostability of CoPt<sub>3</sub> nanocrystals.**

Long-term stability under ambient conditions is an important issue for any new nanomaterial, especially for its potential application. Colloidal solutions prepared by washing and re-dissolving CoPt<sub>3</sub> nanocrystals in non-polar solvents (hexane, toluene or chloroform) were stable for several days before a uniform film was formed at the bottom and the walls of the glass vessel. Addition of small amounts of HDA (~0.1 mg of HDA per 25 mg of the nanocrystals) resulted in immediate dissolution of this film. The resulting colloids were stable in air for months without any further precipitation. XRD patterns of the samples which were stored in air for weeks were almost identical to those of as-prepared CoPt<sub>3</sub> nanocrystals. Even at elevated temperatures oxidation of CoPt<sub>3</sub> nanocrystals was very slow. Figure 3.15a shows XRD patterns of both as-prepared CoPt<sub>3</sub> nanocrystals and the samples annealed at 100, 200 and 300°C for 2 h in air. The nanocrystals annealed at 100 and 200°C were still easily soluble in non-polar solvents and did not reveal the presence of any oxides. After annealing at 300°C in air the CoPt<sub>3</sub> nanocrystals became insoluble in common non-polar solvents and the XRD pattern revealed weak additional reflexes which could be assigned to CoO. Moreover, the (111) reflex in the XRD pattern was slightly shifted towards a platinum-rich alloy. XRD patterns of CoPt<sub>3</sub> samples annealed at 400°C and 500°C under vacuum did not show the presence of any crystalline oxides as well (Figure 3.15b).

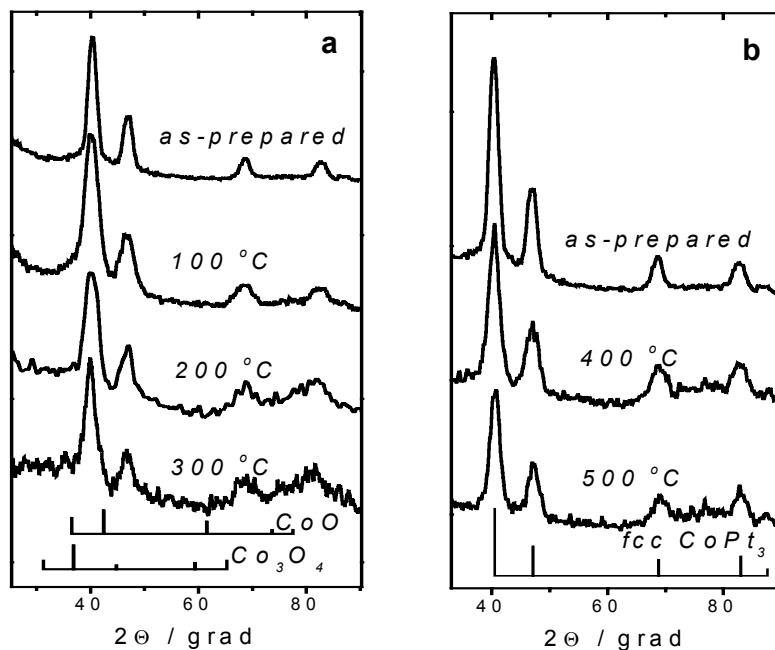


**Figure 3.15.** (a) and (b) XRD patterns of annealed  $\text{CoPt}_3$  nanoparticles (a) in air and under (b) vacuum respectively.

Annealing of  $\text{CoPt}_3$  nanoparticles at temperature higher than  $600\text{ }^\circ\text{C}$  in the atmosphere of forming gas ( $\text{Ar} - 95\%$ ;  $\text{H}_2 - 5\%$ ) results in the transition from chemically disordered *fcc* to chemically ordered *fcc* phase. Figure 3.16 represents XRD pattern of  $\sim 6.3\text{ nm}$   $\text{CoPt}_3$  nanoparticles annealed at  $600\text{ }^\circ\text{C}$  for  $\sim 1\text{h}$ . Narrowing of XRD peaks after heat treatment indicates coalescence of particles which causes an increase of apparent particle size from  $\sim 6.3$  to  $\sim 13\text{ nm}$ . Frommen et al. [41] reported that  $\text{CoPt}_3$  nanoparticles stabilised with oleic acid and oleyl amine undergo a transition from a disordered to an ordered state at  $\sim 750\text{ }^\circ\text{C}$  and this transition was also accompanied by particle coalescence.

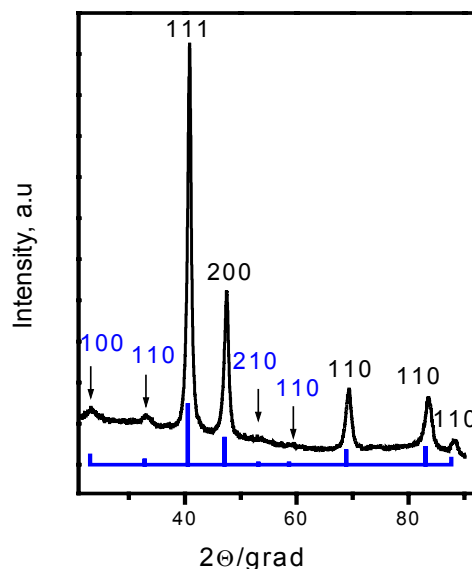


**Figure 3.16.** XRD pattern of  $\sim 6.3\text{ nm}$   $\text{CoPt}_3$  nanocrystals annealed at  $600\text{ }^\circ\text{C}$  for  $\sim 1\text{h}$ . Arrows depict the additional peaks which are typical for chemically ordered *fcc*  $\text{CoPt}_3$  nanoparticles.

The difference in the transition temperature can be explained by the different nature of stabilising shell around the nanocrystals.

### **3.6. Conclusions**

High quality CoPt<sub>3</sub> nanocrystals with narrow particle size distribution and mean size between ~3 nm up to 18 nm can be prepared in a predictable and reproducible manner via simultaneous reduction of platinum acetylacetonate and thermodecomposition of cobalt carbonyl in the presence of 1-adamantanecarboxylic acid and hexadecylamine as stabilizing agents. Figure 3.17 shows the systematic evolution of XRD patterns of chemically disordered fcc phase CoPt<sub>3</sub> nanocrystals upon increase of their size from ~3 to 17 nm. All samples were synthesised in form of stable colloidal solutions via the same chemical route applying the nanocrystal size-control techniques described below. CoPt<sub>3</sub> nanocrystals larger than ~13 nm are stable in crude solutions only at temperatures above ~100°C because of their strong magnetic dipole interactions which result in nanocrystal aggregation at room temperature.

From the investigation of the effect of different reaction conditions (reaction temperature, concentration of the precursors and stabilizer) on the nanocrystal synthesis we conclude that the size control achieved in this system is of purely kinetic nature. Nanocrystal size control in systems without the Ostwald ripening stage can be achieved via control over the balance between the nucleation and growth rates. We demonstrated on an example of CoPt<sub>3</sub> nanocrystals that slower nucleation results in the formation of larger nanocrystals with narrower size distribution (st.div.~7%), while fast nucleation yields smaller nanocrystals with broader (st.div.~14%) size distributions. The CoPt<sub>3</sub> nanocrystal size increases with increasing of the concentration of stabilizer (1-adamantanecarboxylic acid). This effect was attributed to the slower rate of nucleation at high concentration of the stabilizer. Such behavior seems to be typical of the hot organometallic syntheses of metal nanocrystals and was observed also in the preparation of Fe, Pt as well as FePt and CoPd<sub>2</sub> nanocrystals. The possibility of the formation of faceted cubic CoPt<sub>3</sub> nanocrystals was also shown.

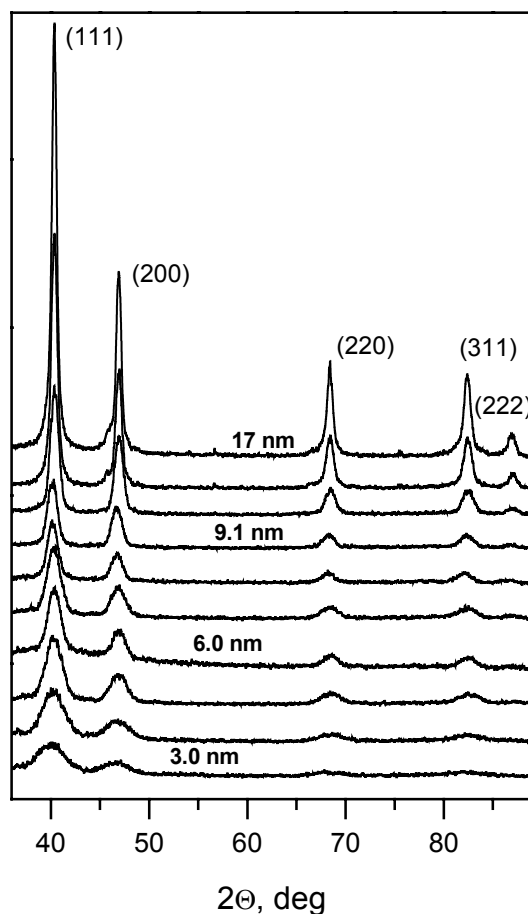


**Figure 3.17.** Size-dependent XRD patterns of  $\text{CoPt}_3$  nanocrystals. The average nanocrystal sizes were calculated by the Debye-Scherrer equation.

Size control of nanocrystals via control of the concentrations of stabilisers and precursors allows us to prepare nanocrystals of the same sizes at different temperatures which allows to investigate the temperature influence on the faceting at the nanometer scale.

The experimental results seem to indicate that nucleation of  $\text{CoPt}_3$  nanocrystals occurs on some cobalt seeds forming via thermodecomposition of cobalt carbonyl. The formation of these clusters is the rate-limiting step for the whole nucleation process whereas the concentration of platinum precursor does not affect the nucleation rate. A possible microscopic nucleation mechanism was discussed.

To the best of our knowledge, this is the first attempt of a systematic experimental study of the “hot” synthesis of metal nanocrystals and the nucleation mechanism of metal alloys. The development of new methods of precise size control of  $\text{CoPt}_3$  nanocrystals allows the investigation of their size-dependent magnetic properties.

The CoPt<sub>3</sub> nanocrystals were stable in air and did not reveal any oxidation even after annealing at 200°C under ambient conditions. Annealing under forming gas atmosphere results in the transition from chemically disordered to chemically ordered fcc CoPt<sub>3</sub> nanoparticles.

### **3.7. References**

1. Alivisatos, A. P. *Science* **1996**, *271*, 993.
2. Murray, C. B.; Kagan, C. R.; Bawendi, M. G. *Annu. Rev. Mater. Sci.* **2000**, *30*, 545.
3. Leff, D.V.; Ohara, P.C.; Heath J.R.; Gelbart, W.M. *J. Phys. Chem.* **1995**, *99*, 7036.
4. Hyeon, T.; Lee, S. S.; Park, J.; Chung, Y.; Na, H. B. *J. Am. Chem. Soc.* **2001**, *123*, 12798.
5. Wiekhorst, F.; Shevchenko, E.; Weller, H.; Kötzler, *J. Phys. Rev. B* (in press).
6. Murray, C. B.; Norris, D. J.; Bawendi, M. G. *J. Am. Chem. Soc.* **1993**, *115*, 8706.
7. Yang, M. H.; Flynn, C. P. *Phys. Rev. Lett.* **1989**, *62*, 2476.
8. Shevchenko, E.V.; Talapin, D.V.; Rogach, A.L.; Kornowski, A.; Haase, M.; Weller H. *J. Am. Chem. Soc.* **2002**, *124*, 11480.
9. Peng, Z. A.; Peng, X. *J. Am. Chem. Soc.* **2002**, *124*; 3343.
10. Glatter, O. *J. Appl. Cryst.* **1977**, *10*, 415.
11. Glatter, O. *J. Appl. Cryst.* **1980**, *13*, 7.
12. Korgel, B. A.; Fullam, S.; Connolly, S.; Fitzmaurice, D. *J. Phys. Chem. B* **1998**, *102*, 8379.
13. Mattoussi, H.; Cumming, A. W.; Murray, C. B.; Bawendi, M. G.; Ober, R. *J. Chem. Phys.* **1996**, *105*, 9890.
14. Wang, Z. L. *Adv. Mater.* **1998**, *10*, 13.
15. V. F. Puentes, D. Zanchet, C. K. Erdonmez, A. P. Alivisatos. *J. Am. Chem. Soc.* **2002**, *124*, 12874-12880.
16. Peng, X.; Manna, L.; Yang, W. D.; Wickham, J.; Scher, E.; Kadavanich, A.; Alivisatos, A. P. *Nature* **2000**, *404*, 59.
17. Lee, S.-M.; Jun, Y.-W.; Cho, S.-N., Cheon, J. *J. Am. Chem. Soc.* **2002**, *124*, 11244.
18. Ahmadi, T.S.; Wang, Z.L.; Green, T.C.; Henglein A.; El-Sayed, M.A. *Science* **1996**, *272*, 924.
19. Puentes, V. F.; Krishan, K. M.; Alivisatos, A. P. *Science* **2001**, *291*, 2115.
20. Murray, C. B.; Kagan, C. R.; Bawendi, M. G. *Science* **1995**, *270*, 1335.

21. Rogach, A. L. ; Talapin, D. V.; Shevchenko, E. V.; Kornowski, A.; Haase M.; Weller H. *Adv. Funct. Mater.* **2002**, *12*, 653.
22. Collier, C. P.; Vossmeier, T.; Heath, J. R. *Annu. Rev. Phys. Chem.* **1998**, *49*, 371.
23. Sugimoto, T. *Monodisperse Particles*, Elsevier **2001**.
24. Talapin, D. V.; Rogach, A. L.; Haase, M.; Weller, H. *J. Phys. Chem. B* **2001**, *105*, 12278.
25. Pacholski, C.; Kornowski, A.; Weller, H. *Angewandte Chemie, Int. Edition* **2002**, *41*, 1188.
26. Teranishi, T.; Hosoe, M.; Tanaka, T.; Miyake, M. *J. Phys. Chem. B* **1999**, *103*, 3818.
27. Park, S.-J.; Kim, S.; Lee, S.; Khim, Z.G.; Char, K.; Hyeon, T. *J. Am. Chem. Soc.* **2000**, *122*, 8581.
28. Murray, C. B.; Sun, S.; Doyle, H.; Betley, T. *MRS Bulletin* **2001**, 985.
29. Sun, S.; Murray, C. B.; Doyle H. *Mat. Res. Soc. Symp. Proc.* **1999**, *577*, 385.
30. Sun, S.; Murray, C. B. *J. Appl. Phys.* **1999**, *85*, 4325.
31. Sun, S.; Murray, C. B.; Weller, D.; Folks, L.; Moser, A. *Science* **2000**, *287*, 1989.
32. Dai, Z. R.; Sun, S.; Wang, Z. L. *Surf. Sci.* **2002**, *505*, 325.
33. Auer, S.; Frenkel, D. *Nature*, **2001**, *409*, 1020 and references herein.
34. Peng, X.; Wickham, J; Alivisatos, A. P. *J. Am. Chem. Soc.* **1998**, *120*, 5343.
35. Wagner, C. Z. *Elektrochem.* **1961**, *65*, 581.
36. Klein, W.; Leywraz, F. *Phys. Rev. Lett.* **1986**, *57*, 2848.
37. Park, J-I.; Cheon, J. *J. Am. Chem. Soc.*; **2001**; *123*; 5743.
38. Ciacchi, L. C.; Pompe, W.; De Vita, A. *J. Am. Chem. Soc.* **2001**, *123*, 7371.
39. Henglein, A.; Giersig, M. *J. Phys. Chem. B* **2000**, *104*, 6767.
40. Gogging, P. L.; Googfellow, R. *J. Chem. Soc., Dalton Trans.* **1973**, 2355.
41. Frommen, C.; Rösner, H.; Fenske, D. *J. Nanosci. Nanotech.* **2002**, *2*, 509.



## 4. Synthesis of other magnetic alloy nanocrystals and phase transfer of magnetic nanocrystals into water

---

*Platinum – iron and palladium – cobalt alloy nanocrystals were synthesised. The use of different co-ordinating mixtures allowed us to control composition and shape of platinum – iron nanocrystals. Size series of fairly monodisperse, highly crystalline platinum – iron and palladium – cobalt nanocrystals were obtained with the mean particle size between 2.5 – 7.6 nm and 3.5 – 6 nm, respectively. Surface modification of magnetic alloy nanocrystals with 11-mercaptopundecanoic acid allowed us to prepare water soluble magnetic alloy nanocrystals.*

---

### 4.1. Introduction

An evident progress in understanding of the phenomena of nanomagnetism has been achieved during the last years [1]. The most part of the magnetic investigations was focused on the nanolayers of the magnetic materials where the control of the composition, thickness and crystallinity is possible. In spite of both fundamental and practical great interest to the size-dependent physical properties of magnetic nanoparticles the lack of synthetic methods for the synthesis of high quality magnetic nanoparticles restricted their systematic investigation. Significant progress was achieved by introducing the organometallic approach for the synthesis of metal [2-11] and oxide [12,13] magnetic nanoparticles. Relatively high reaction temperature ( $> 100$  °C) and the proper choice of capping ligands provide high crystallinity and narrow size distribution of nanoparticles. Several successful syntheses based on the colloidal organometallic approach were developed for Fe [2], Ni [3,4], Co [4,5-9], FePt [10], CoPt<sub>3</sub> [11],  $\gamma$ -Fe<sub>2</sub>O<sub>3</sub> [12], Fe<sub>3</sub>O<sub>4</sub> [13] and cobalt ferrite [14] magnetic nanocrystals. The air sensitivity of the magnetic transition metal nanocrystals makes their handling complex and has prompted the use of the metal oxide nanoparticles in many applications despite the weaker magnetic properties [15]. The magnetic and chemical properties of the monometallic magnets can be significantly enhanced by the formation of alloy with noble metals [16]. The further study of fundamental aspects and practical applications requires the extension of a pollete of available materials and hence further screenings of novel materials is desired.

In this Chapter the synthetic methods and the concepts of size control of platinum – iron and cobalt – palladium binary alloy nanoparticles are discussed. Also a method of the transfer of magnetic PtFe and CoPt<sub>3</sub> nanocrystals from organic media into water is reported.

### 4.2. PtFe nanocrystals

#### 4.2.1. Oleic acid - oleyl amine approach

PtFe nanocrystals can be prepared by a high temperature organometallic synthesis based on reduction of platinum acetylacetonate and decomposition of iron pentacarbonyl in the presence of oleic acid and oleyl amine [3]. A combination of oleic acid\* (OA) and oleyl amine was used to stabilise the PtFe colloids and prevent oxidation. The recipe given by Sun et al. was the pioneer approach which allowed to produce magnetic alloy nanocrystals of high quality. The typical synthetic procedure is as follows: under airless conditions platinum acetylacetonate (197 mg) and 1,2-hexadecandiol (390 mg) were dissolved in dioctylether (20mL) and heated to 100 °C. Oleic acid, oleyl amine and Fe(CO)<sub>5</sub> were added and the reaction mixture was heated to reflux (~300 °C) for ~30 min. After cooling of the reaction mixture to the room temperature the particles were isolated and purified by adding ethanol and centrifugation. The washed particles were re-dispersed in hexane or toluene. EDX measurements on properly washed nanocrystals gave the composition nanocrystals close to PtFe. Elaidin acid (trans-isomer of oleic acid) can be also used in the co-ordinating mixture instead of oleic acid (cis-isomer). The use of elaidin acid – oleyl amine co-ordinating mixture resulted in the formation PtFe nanoparticles identical to PtFe nanoparticles prepared in OA-oleyl amine co-ordinating mixture. Figure 4.1. represents XRD-patterns of as-synthesized 3 nm PtFe nanocrystals prepared in OA-oleyl amine and elaidin acid-oleyl amine co-ordinating mixtures.

OA-oleyl amine synthesis of PtFe nanocrystals has obvious advantages. First, the simplicity of the synthesis allows to prepare sufficient amounts of PtFe nanocrystals. Second, the composition of nanocrystals can be readily controlled by varying the molar ratio of iron carbonyl to the platinum salt. However relatively low reproducibility and high sensitivity of quality of the resulting materials to many parameters (traces of oxygen, purity of the precursors, *etc.*) can be considered as the drawbacks of this approach.

---

\*  $CH_3(CH_2)_7CH=CH(CH_2)_7CO_2H$  (*cis-9-octadecen acid = oleyl acid*).

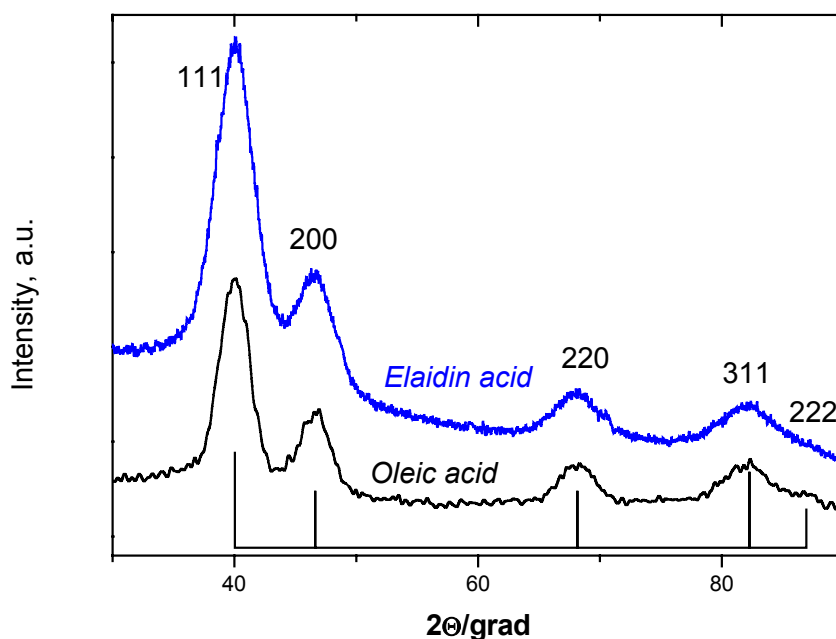


**Figure 4.1.** XRD pattern of as-synthesized 3 nm PtFe nanocrystals prepared in the presence of oleic acid and elaidin acid. The indexing is based on tabulated fcc PtFe reflections. The size of nanocrystals was calculated by Debye–Sherrer equation.

TEM and HRTEM investigations of as-prepared PtFe nanoparticles showed relatively monodisperse (st. div. 14 %) well separated crystalline nanoparticles (Figure 4.2). Subsequent size-selective precipitation divided initial colloidal solution to the fractions with narrower size distribution ( $\leq 7\%$ ) which can be used to build two-dimensional and three-dimensional ordered structures (*Chapter 6*). When colloids of PtFe nanocrystals were stored at ambient conditions oxidation of nanocrystals was noticed in approx. two weeks. The appearance of iron oxides was detected by XRD. So, PtFe nanocrystals stabilised with OA – oleyl amine have to be stored under nitrogen atmosphere or they need a better protection of their surface.

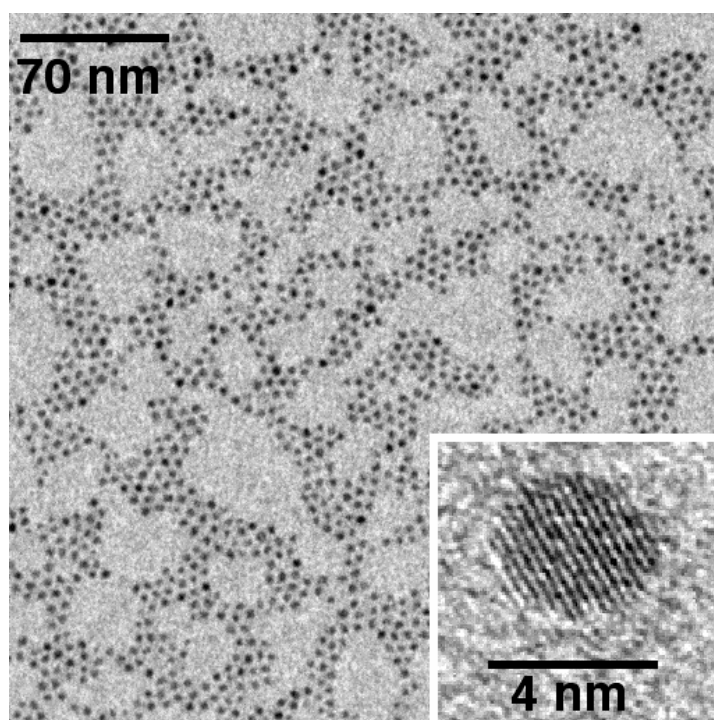


**Figure 4.2.** TEM and HRTEM (inset) of as-synthesised PtFe nanocrystals.

As in the case of CoPt<sub>3</sub> nanocrystals, size of PtFe nanocrystals did not change with the refluxing time (Figure 4.3). Nanocrystals isolated from the reaction solution after different refluxing time had the same size.

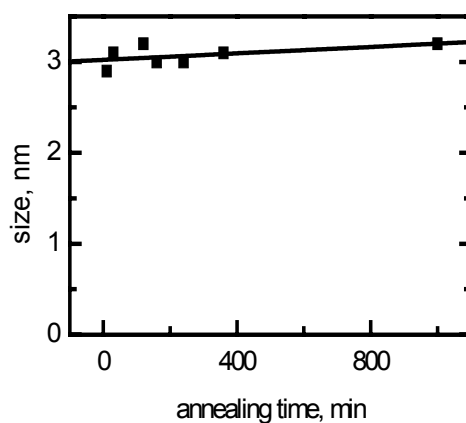


**Figure 4.3.** Dependence of FePt nanocrystal size on duration of heating. FePt nanocrystals were prepared via the organometallic route in OA – oleyl amine coordinating mixture. The size of nanocrystals was calculated from width of the XRD reflexes according to the Debye–Scherrer equation.

The size control of the platinum - iron nanocrystals can be achieved by growing of 2.5 – 3 nm monodisperse seed particles and then adding more reagents to enlarge the existing

seeds to the desired size [10]. These seeds serve as nucleation centres for additional precursors. The final nanocrystal size is control by the varying the amount of precursors added to the seed particles. This universal approach was earlier successfully applied to increase the size of both semiconductor and magnetic nanocrystals [10,11,17,18]. However, this approach is rather complex to be performed under rigorously air-free conditions. Another problem is a nucleation of new nanocrystals resulting in a broad size distribution of colloidal solution [11]. However, even if monodispersity of nanocrystals is achieved, nanocrystals enlarged by the method of additional injections usually have a high concentration of lattice defects. Figure 4.4. represents the XRD pattern of relatively monodisperse PtFe nanocrystals enlarged by this way from 3 nm to 6 nm as confirmed by TEM. TEM investigation indicates PtFe nanocrystals with narrow size distribution. Nevertheless, the size of nanocrystals calculated by Debye– Sherrer equation\* (“XRD-size”) is only 4 nm. Considerably smaller value of “XRD-size” than “TEM-size” (values obtained by statistical processing of TEM images) means that the crystalline lattice of PtFe nanocrystals contains a lot of lattice defects (stacking faults, twinned planes, *etc.*).

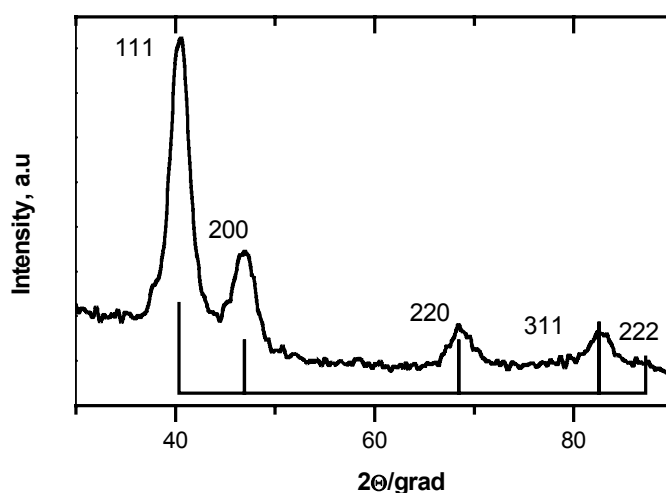
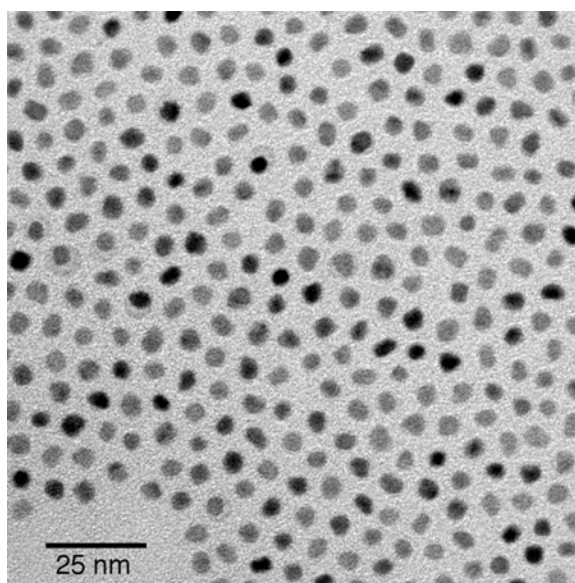


**Figure 4.4.** XRD pattern of 6 nm (“TEM-size”) PtFe nanocrystals obtained by adding more reagents to 3 nm seeds.

\* Width of the XRD reflexes provides information about the X-ray coherence length which is close to the average size of the single crystalline domain inside the nanocrystal.

##### 4.2.2. ACA-approach

ACA approach developed for CoPt<sub>3</sub> nanocrystals (*Chapter 2*) also allowed us to obtain platinum – iron alloy nanocrystals of high quality. We have tested different particle growth regimes, various precursors and stabilising agents (ACA, primary amines, TDPA and etc.) with the goal to make the synthesis of platinum – iron nanocrystals more controllable, versatile and improve the stability of nanocrystals surface against oxidation. Syntheses of platinum – iron nanocrystals in the presence of ACA result in the preparation of relatively monodisperse crystalline platinum – iron nanocrystals (Figure 4.5).



---

**Figures 4.5.** TEM image of the PtFe nanocrystals prepared in DDA-diphenyl ether coordinating mixture in the presence of ACA.

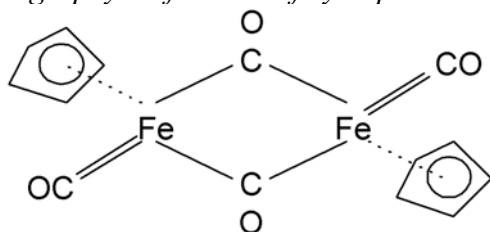
Proper choice of the reaction temperature regime allowed us to obtain well separated highly crystalline nanoparticles of the different sizes. Surprisingly, the same initial molar ratio of platinum and iron precursor (1:2) yields different compositions of platinum – iron alloy nanocrystals compositions in different stabilising mixtures. To find out the composition, EDX analyses of properly washed platinum-iron nanocrystals were performed. In the case of OA – oleyl amine and primary amine – ACA co-ordinating mixtures, composition close to PtFe was observed, while in the ACA – TDPA, HDA – ACA – TDPA co-ordinating mixtures platinum – iron nanocrystals with the composition close to Pt<sub>3</sub>Fe were formed (Table 4.1). The influence of different reaction conditions on the nanocrystal composition is summarised in Table 4.1.

**Table 4.1** ACA approach to synthesis of PtFe nanocrystals

Fe precursor	Stabilisers, solvents	Nanocrystal composition	XRD-Size, nm
Fe(CO) <sub>5</sub>	ACA, TDPA, <i>di</i> -phenylether		~4.2 spherical ~3.8 spherical
Cyclopentadienyliron dicarbonyl dimer*	ACA, TDPA <i>di</i> -phenylether	Fe – 25–30 % Pt – 70–75 %	~4.8 spherical
	ACA, HDA, TDPA, <i>di</i> -phenylether		~9.0 irregular-shaped
	ACA, HDA, <i>di</i> -phenylether	Fe ~ 50 % Pt ~ 50 %	~5.6 irregular-shaped
Ferrocene	ACA, TDPA <i>di</i> -phenylether	Precipitation of bulk Pt	

As evident from the Table 4.1, TDPA strongly influences on the final composition of platinum – iron alloy nanocrystals. The shift in the peak positions is consistent with Vegard’s law [19] that states that the lattice parameter of a binary solid solution is directly proportional to the atomic percent of the substance in the alloy. Peaks of XRD patterns of all samples prepared in the presence of TDPA are systematically shifted towards platinum (Figure 4.6a). This fact also confirms the excess of platinum in comparison with the samples synthesised without TDPA (Figure 4.6b). In the presence of TDPA the reaction\*\* occurs only at temperatures higher than ~190 °C. In the absence of TDPA the reaction happens at ~165 – 170 °C. As shown above on the example of CoPt<sub>3</sub> nanocrystals (*Chapter 3*), cobalt precursors are expected to be responsible for the nucleation process. Disseminating the suggestions

\* *graphical formula of cyclopentadienyliron dicarbonyl dimer:*



\*\* *the beginning of the reaction is accompanied by a rapid colour change from transparent orange to dark-brown*

found to be valid for  $\text{CoPt}_3$  nanocrystals to platinum – iron nanocrystals, we can assume that iron precursor forms the critical nuclei. In this case strong complexation of iron monomer with TDPA can explain both relatively high reaction temperatures and platinum-rich final composition of platinum – iron alloy nanocrystals: TDPA forms strong complexes with iron which thermally decompose forming nuclei for further growth of platinum – iron nanocrystals. It happens at temperatures higher than  $190\text{ }^\circ\text{C}$  when  $\text{Fe}(\text{CO})_5$  or  $220\text{ }^\circ\text{C}$  when cyclopentadienyliron dicarbonyl dimer are used as an iron precursor. Due to the strong complexation of iron, less iron monomer is available at the growth stage and, as a consequence, platinum – rich alloy nanocrystals are formed.

Because of the high temperature of the initiation of the reaction the role of ACA concentration was not so crucial as in the case of  $\text{CoPt}_3$  nanocrystals where the initiation the reaction occurs at much lower temperature ( $\sim 130\text{ }^\circ\text{C}$ ). Analysis of the XRD and TEM data showed that two different initial concentrations of ACA (Figure 4.6a, curves 1 and 2) lead to the formation of platinum-iron alloy nanocrystals of the same size. It is necessary to note that also in the case of  $\text{CoPt}_3$  nanocrystals if the injection of cobalt stock solution was performed at  $\sim 200\text{ }^\circ\text{C}$  the variations of ACA concentration did not result in any pronounced changes of nanocrystal sizes.

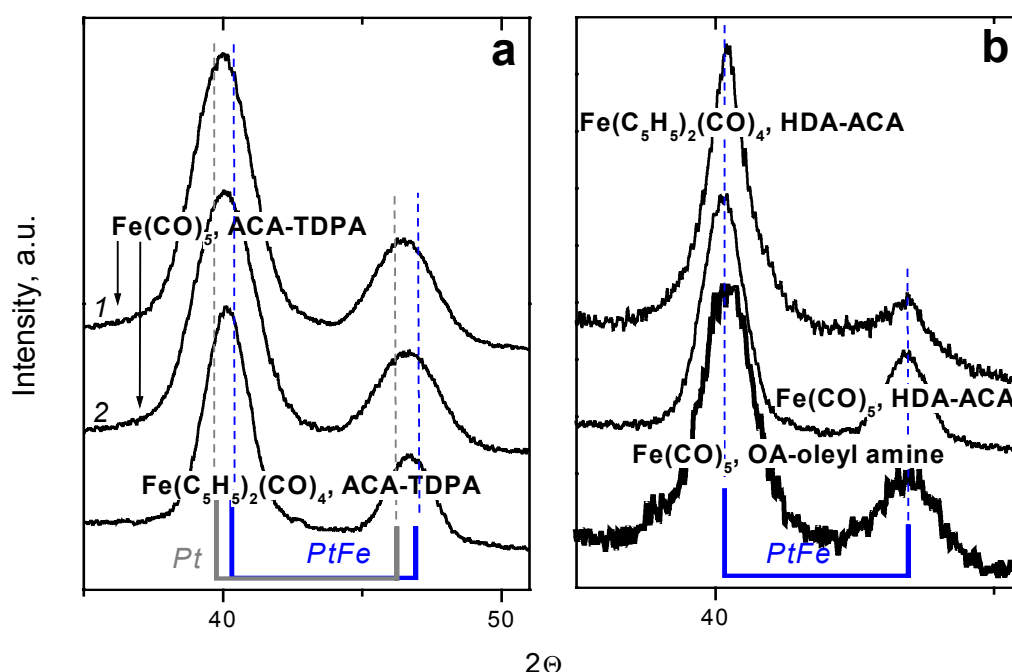


**Figure 4.6.** XRD patterns of platinum – iron nanocrystals prepared in the presence (a) and in the absence (b) of TDPA. (a) – curve 1 and 2 correspond to platinum-iron alloy nanocrystals prepared at different ACA concentration: molar ratio Pt:Fe:ACA – 1:2:2 (curve 1); Pt:Fe:ACA – 1:2:10 (curve 2).

Due to high toxicity of iron carbonyl the search for less dangerous iron precursors is desired. Thus it was found that  $\text{Fe}(\text{CO})_5$  can be replaced with cyclopentadienyliron dicarbonyl dimer.

The nature of the iron precursor did not affect the composition of nanocrystals (Table 4.1) and all dependencies found to be valid for the synthesis of platinum – iron alloy nanocrystals with the use of  $\text{Fe}(\text{CO})_5$  are valid for the synthesis with cyclopentadienyliron dicarbonyl dimer. Figure 4.7 represents TEM and HRTEM images of platinum-rich alloy nanocrystals (the composition of alloy is close to  $\text{Pt}_{75}\text{Fe}_{25}$ ) obtained from cyclopentadienyliron dicarbonyl dimer and  $\text{Pt}(\text{acac})_2$  in the presence of TDPA.

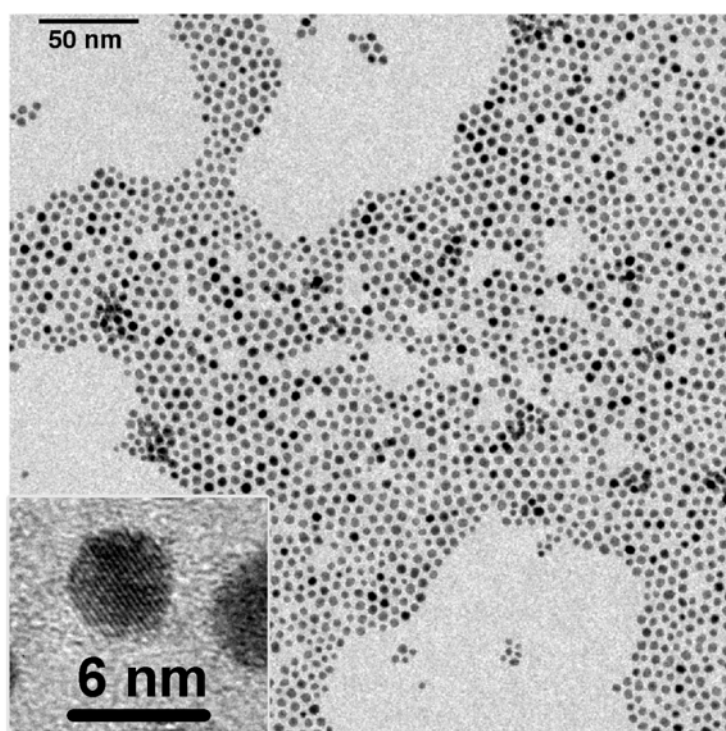


**Figure 4.7.** TEM and HRTEM (inset) of as-synthesised platinum-rich iron-platinum alloy nanocrystals on ACA-TDPA-diphenyl ether coordinating mixture

Moreover, the use of cyclopentadienyliron dicarbonyl dimer as an iron precursor improves the reproducibility of the synthesis. However the transition to less toxic iron precursor (ferrocene) did not result in the formation of platinum – iron nanocrystals because of too high stability of this precursor at the reaction conditions. Even at 230 °C decomposition of ferrocene complex was not detected. Further increase of the reaction temperature resulted in the formation of bulk platinum that is confirmed by XRD data.

We also investigated the synthesis of platinum – iron nanocrystals in order to reveal an easy method of size control of FePt nanocrystals. The original recipe by Sun et al. yields ~3 nm FePt nanocrystals and the particle size is tuned only via additional injections of precursors [10]. In the presence of oleic acid and oleyl amine Pt(acac)<sub>2</sub> starts to decompose at ~130°C what makes difficult tuning the particle size via variation of the reaction temperature. We adopted our ACA – primary amine approach for the preparation of PtFe nanocrystals, because in this coordinating mixture platinum precursor retains the stability up to ~230 °C. The synthesis of FePt nanocrystals was performed in the ACA- dodecylamine coordinating mixture. Injection of the Fe(CO)<sub>5</sub> stock solution at 170 °C resulted in the formation of nearly monodisperse ~4.8 nm nanocrystals with the composition close to Pt<sub>48</sub>Fe<sub>52</sub> (Table 4.2). An increase of the injection temperature up to 215°C resulted in a decrease of the average nanocrystal size to ~3.5 nm and a broader size distribution. The nanocrystal nucleation is too slow at temperatures below 170 °C and thus larger FePt nanocrystals can not be prepared in the ACA – dodecylamine mixture in a reasonable time window.

Stabilising agents control the growth of nanoparticles by binding to the nanoparticle surface. If stabilisers bind too tightly to the particle surface, the growth rate is strongly impeded. In contrast, reversible stabilisation of metal surface results in slow and controllable nanoparticle growth [15]. Sterical factors can also influence on the final nanoparticle size: molecules containing bulky groups have to passivate the surface atoms “worse” because the smaller amount of capping molecules can be arranged at the particle surface. Usually decrease of the particle sizes is observed when the length of alkyl chain increases [4,5]. Thus, the use of tri-butylphosphine (TBP) and tri-butylamine (TBA) results in the formation of ~12-13 nm Co nanoparticles. Replacing TBP and TBA with TOP and tri-octyl amine (TOA) gives ~8-10 nm particles. The size dependence of nanoparticle size on stabiliser length was also observed in the case of magnetic binary alloy nanoparticles. Indeed, the range of available sizes of FePt nanocrystals can be extended when HDA or octadecylamine are used instead of dodecylamine (Table 4.2). However, a relation between particle size and ligand length was not monotonic. Thus the smallest PtFe nanoparticles are prepared in DDA (C<sub>12</sub>). Much larger PtFe nanoparticle can be prepared in HDA (C<sub>16</sub>). Further increase of the length of alkyl chain of primary amine results in the decrease of particle size: nanoparticles grown in ODA (C<sub>18</sub>) were smaller than those, prepared in HDA.

The reaction temperature affected the nanoparticle size of platinum-iron alloy nanoparticles in the same manner as it was observed for CoPt<sub>3</sub> nanocrystals. The considerable decrease of the average nanocrystal size was always observed with increasing reaction

temperature (Table 4.2). However as-prepared FePt nanocrystals larger than ~6 nm usually have rather irregular shape which makes quantitative estimation of the “TEM – size” rather difficult.

**Table 4.2.** *Size control of PtFe nanocrystals*

Pt(acac) <sub>2</sub> - 0.0328 g Fe(CO) <sub>5</sub> – 0.04 mL ACA – 4 g Primary amine – 4 g Diphenyl ether – 2mL	Injection temperature of Fe(CO) <sub>5</sub>	Primary amine		
		DDA	HDA	ODA
	170	4.8 nm	7.6 nm	6.1 nm
	200	4.2 nm	7.3 nm	5.6 nm
	214	3.5 nm	6.7 nm	

The most irregular-shaped platinum – iron nanocrystals were formed in HDA – ACA co-ordinating mixture when cyclopentadienyliron dicarbonyl dimer was used instead of Fe(CO)<sub>5</sub> (Figure 4.8). As in the case of CoPt<sub>3</sub> nanocrystals, we assume here the reversible coordination of platinum – iron nanocrystals with HDA. Probably, in this case weak complexation of the nanocrystal surface at the initial stages of the reaction results in the partial fusion of growing nanocrystals. Analysis of the TEM images shows that the most of irregular-shaped nanocrystals consists of several fused nanocrystals of smaller size (Figure 4.8, *inset*). Also, it was possible to reveal the defects of the crystalline lattice inside some nanocrystals. The storage of the colloidal solution of such irregular-shaped nanoparticles under ambient conditions for months did not result in particles coalescence. The largest nanocrystals (Figure 4.8) can be isolated from the colloidal solution by applying external magnetic field (~0.68 T).

Irregular-shaped nanocrystals have very high surface-to-volume ratio and, as a consequence, a huge amount of stabilising agents at the surface which prevent the aggregation of nanocrystals in the solution and provide long term stability of solutions of platinum – iron nanocrystals. High surface-to volume ratio of these platinum-iron nanocrystals can be interesting for their application in catalysis.

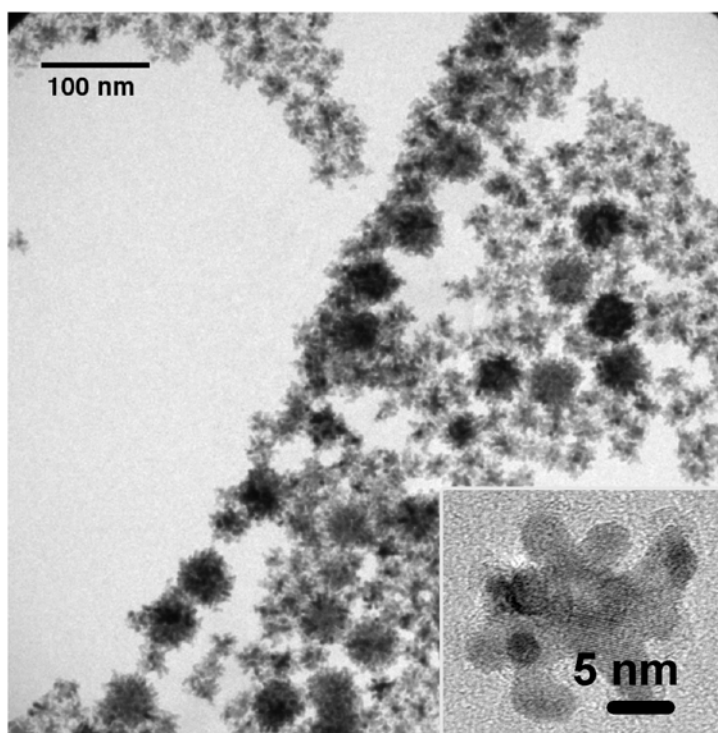


**Figure 4.8.** TEM overview and HRTEM of irregular-shaped platinum-iron nanocrystals prepared when cyclopentadienyliron dicarbonyl dimer was used as an iron precursor.

In contrast to the synthesis of  $\text{CoPt}_3$  nanoparticles a variation of the nanocrystal composition was observed in the case of platinum – iron alloy nanocrystals when the initial ratio of the iron and platinum precursors was changed [10]. Variation of the concentration of precursors results in the preparation of alloy nanocrystals of different sizes but differently-sized nanocrystals have different compositions. This makes the platinum – iron nanocrystal synthesis more complex for studying as compared to  $\text{CoPt}_3$ .

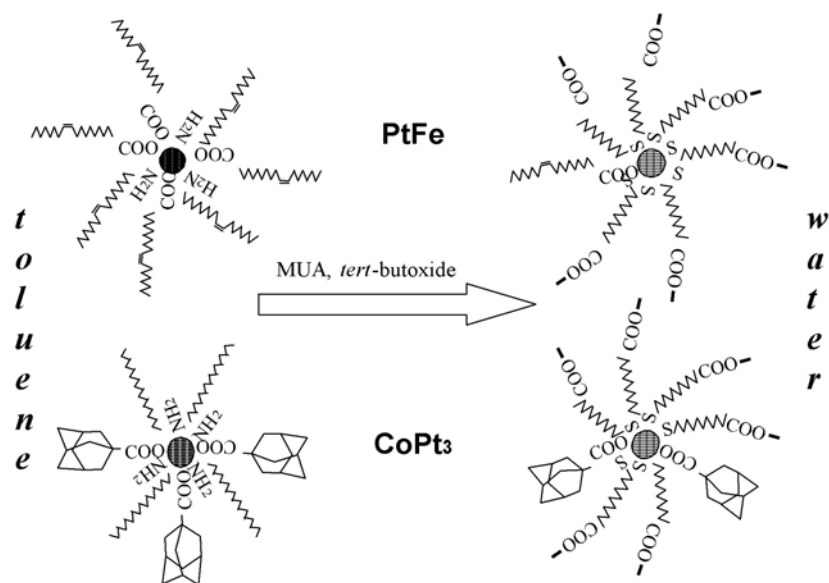
#### 4.2.3. Phase transfer of $\text{PtFe}$ and $\text{CoPt}_3$ nanocrystals from organic solvents into aqueous medium

The nanocrystal surface can be modified by post-preparative exchange of the capping ligands [10,20]. This procedure provides an additional degree of freedom in further handling the nanocrystals because the chemistry of the surface ligands determines a number of important nanocrystal properties: solubility in polar or non-polar solvents, stability against oxidation, interparticle spacing in self-assembled superstructures, *etc.* Moreover, specific surface groups of the stabilisers can be used for linking magnetic nanocrystals to different species like other nanoparticles or biomolecules. For instance,  $\text{Fe}_2\text{O}_3\text{-Fe}_3\text{O}_4$  magnetic

nanocrystals functionalized with amine groups were coupled with oligonucleotides and were used as a magnetic nanosensor for the detection of specific oligonucleotides [21]. It was also shown that species adsorbed at the surface of magnetic nanoparticles, e.g., electron donors like pyridine, can change the magnetisation and decrease the surface contribution into magnetic behaviour of nanocrystals [22]. Poly(ethylenimine)-functionalized FePt nanocrystals were packed into uniform films with controllable dimension and thickness using the layer-by-layer deposition technique [23].

The organometallic route seems to be the most perspective way to produce magnetic alloy nanocrystals. The surface of as-prepared PtFe and CoPt<sub>3</sub> nanocrystals is capped with a passivating organic shell. These surface ligands determine the solubility of nanocrystals in non-polar solvents. However, some potential applications, e.g. bio-labeling, require water-soluble and stable magnetic nanoparticles with no loss of physical or chemical properties over extended period of time. A surface-exchange procedure was proposed to transfer the nanocrystals from organic solvents into water [23].

Due to exchange (Scheme 4.1) of the initial stabilisers (ACA - HDA in the case of CoPt<sub>3</sub> and OA-oleyyl amine in the case of PtFe nanocrystals) with long chain 11-mercaptoundecanoic acid (MUA), PtFe and CoPt<sub>3</sub> nanocrystals can be successfully transferred from non-polar solvent into water. In a typical route ~20 mg of freshly prepared magnetic alloy nanocrystals were precipitated and dried under vacuum. After that ~20 mg of 11-mercaptoundecanoic (11-MUA) acid were added to the nanocrystals. Nanocrystals and 11-MUA were stirred at ~50 °C for ~12 hours. ~30mL of THF were added to the MUA/nanocrystals mixture at ~40 °C and a clear solution of nanocrystals was formed. A suspension of potassium *t*-butoxide in THF was added to the THF solution of nanocrystals in order to deprotonate the carboxylic acid group of MUA. The resulting gel was centrifuged and supernatant solution was poured off. The residue was washed five times with THF and the final residue was allowed to dry in air for 20 min. The obtained dry residue was dissolved in water and filtered through a PTFE 0.2 µm filter. Aqueous colloids of PtFe and CoPt<sub>3</sub> nanocrystals revealed essential stability. Figure 4.9 represents TEM and HRTEM images of water-soluble 4.5 nm PtFe and 3.8 nm CoPt<sub>3</sub> nanoparticles. The particles have the same size and size distribution as they had before the surface exchange.



**Scheme 4.1.** Schematic presentation of phase transfer of magnetic into aqueous medium

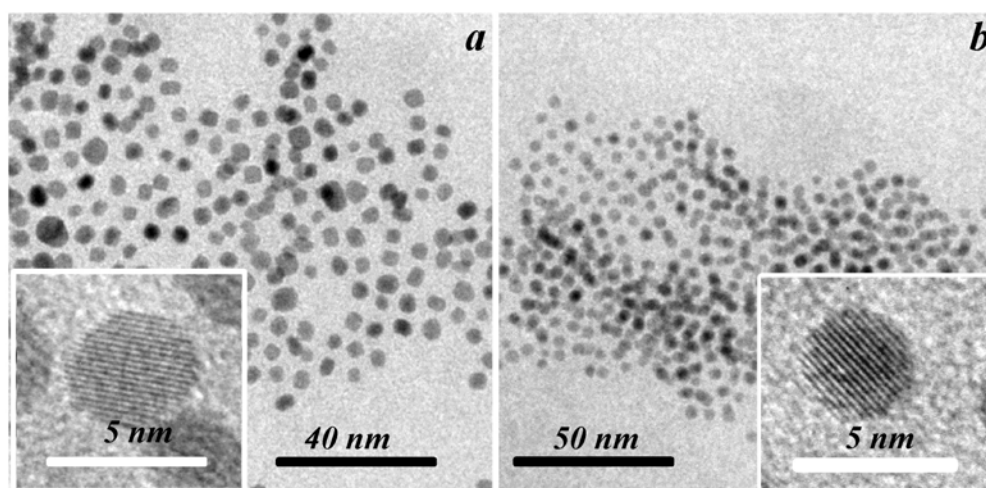
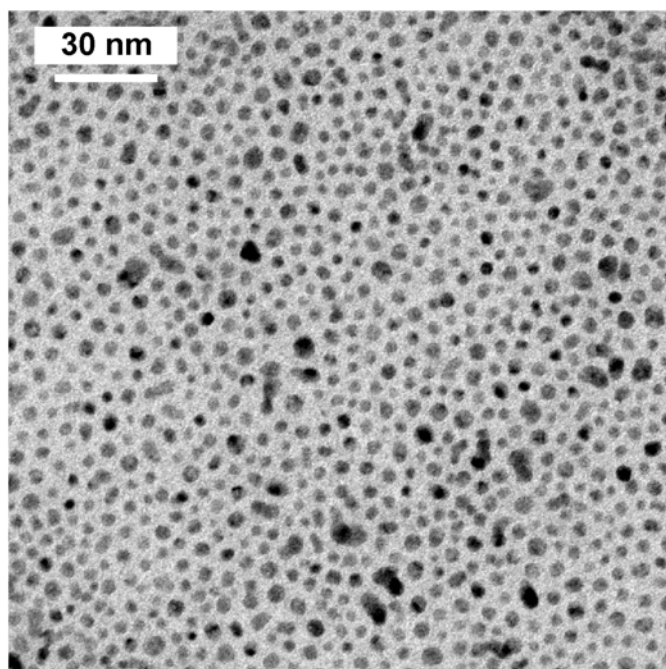


**Figure 4.9.** TEM and HRTEM (insets) of water-soluble  $\sim 4.5$  nm PtFe (a) and  $\sim 3.8$  nm CoPt<sub>3</sub> (b) nanocrystals capped with 11-mercaptoundecanoic acid and transferred from toluene into water.

### 4.3. CoPd<sub>2</sub> nanocrystals

CoPd<sub>2</sub> nanocrystals can also be prepared by the ACA approach in a neat HDA or HDA – diphenyl ether coordinating mixture (Figure 4.10). However, the preparation of CoPd<sub>2</sub> nanocrystals has some peculiarities in comparison with CoPt<sub>3</sub> nanocrystals. Pd(acac)<sub>2</sub> starts to decompose at relatively low temperature ( $\sim 125^\circ\text{C}$ ) in the ACA - HDA mixture yielding

irregularly shaped polydisperse Pd nanocrystals. This makes rather complex tuning the particle size by a variation of the reaction temperature. Also, if the concentration of ACA is high enough, the Co-precursor formed a too stable complex with ACA what again resulted in formation of Pd nanocrystals. However, the proper choice of the molar ratio between Co precursor and ACA was a key point of the successful synthesis of  $\text{CoPd}_2$  nanocrystals. Variation of the injection temperature as well as the ratio between the palladium and cobalt precursors allowed tuning the size of  $\text{CoPd}_2$  nanocrystals in the same manner as in the case of  $\text{CoPt}_3$  nanocrystals. For instance, injection of cobalt precursor at 125 °C resulted in the formation of ~3.5 nm crystals while the injection at 100 °C increased the size of  $\text{CoPd}_2$  nanocrystals up to ~6 nm. However reaction conditions of synthesis of cobalt-palladium alloy nanocrystals need to be improved, since as-prepared  $\text{CoPd}_2$  nanocrystals have size distributions much broader than as-prepared platinum-iron and cobalt-platinum alloy nanocrystals. Figure 4.10 represents a typical TEM image of  $\text{CoPt}_2$  nanoparticles prepared in HDA-diphenyl ether co-ordinating mixture. Probably improvement of the particle size distribution can be achieved by proper choice of co-surfactant in addition to ACA.



---

**Figure 4.10.** TEM overview image of  $\text{CoPd}_2$  nanocrystals prepared by ACA approach.

#### 4.4. Conclusions

Highly crystalline platinum – iron,  $\text{CoPt}_3$  and novel  $\text{CoPd}_2$  magnetic alloy nanocrystals were synthesised *via* organometallic approach in different co-ordinating mixtures (Figure 4.11) and characterised by XRD, EDX, TEM and HRTEM. The size of PtFe and  $\text{CoPd}_2$  nanocrystals can be controlled using the methods developed for  $\text{CoPt}_3$  nanoparticles and discussed in *Chapter 3*. The ACA approach seems to be a perspective way to prepare cobalt – palladium nanocrystals of high quality. Synthesis of cobalt - palladium nanocrystals requires further optimisation of the reaction conditions. However series of nearly monodisperse platinum – iron and  $\text{CoPd}_2$  nanocrystals can be isolated by size-selective precipitation. Magnetic alloy nanocrystals prepared in non-polar solvents can be successfully transferred from organic solvent into aqueous medium by modification of nanocrystal surface.

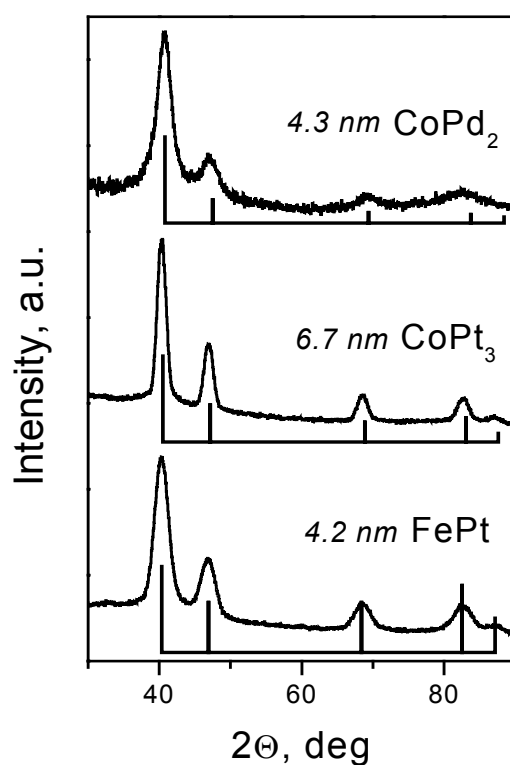


**Figure 4.11.** Typical XRD patterns of FePt,  $\text{CoPt}_3$  and  $\text{CoPd}_2$  nanocrystals synthesised in the ACA-primary amine stabilising mixture. The average nanocrystal sizes were calculated by the Debye-Scherrer equation.

## 4.5. References

1. Klabunde, K.J. *Nanoscale Materials in Chemistry*, John Wiley & Sons, Inc. **2001** (Sorensen C.M. *Magnetism*. pp.162-221).
2. Park, S. J.; Kim, S.; Lee, S.; Khim, Z.G.; Char, K.; Hyeon, T. *J. Am. Chem. Soc.* **2000**, *122*, 8581.
3. Ely, T.O.; Amiens, C.; Chaudret, B.; Snoeck, E.; Verelst, M.; Respaud, M.; Broto, J.M. *Chem. Mater.* **1999**, *11*, 526.
4. Murray, C.B.; Sun, S.; Doyle, H.; Betley, T. *MRS Bulletin* **2001**, 985.
5. Sun, S.; Murray, C.B.; Doyle, H. *Mat. Res. Soc. Symp. Proc.* **1999**, *577*, 385.
6. Puentes, V.F.; Krishnan, K.; Alivisatos, A.P. *Topics in Catalysis* **2002**, *19*, 145.
7. Puentes, V.F.; Krishnan, K.; Alivisatos, A.P. *Science* **2001**, *291*, 2115.
8. Puentes, V.F.; Zanchet, D.; Erdonmez, C.K.; Alivisatos, A.P. *J. Am. Chem. Soc.* **2002**, *124*, 12874.
9. Dumestre, F.; Chaudret, B.; Amiens, C.; Fromen, M.-C.; Casanove, M.-J.; Renaud, P.; Zurcher, P. *Angew. Chem. Int. Ed.* **2002**, *41*, 4286.
10. Sun, S.; Murray, C.B.; Weller, D.; Folks, L.; Moser, A. *Science* **2000**, *287*, 1989.
11. Shevchenko, E.V.; Talapin, D.V.; Rogach, A.L.; Kornowski, A.; Haase, M.; Weller, H. *J. Am. Chem. Soc.* **2002**, *124*, 11480.
12. Hyeon, T.; Lee, S.S.; Park, J.; Chung, Y.; Na, H.B. *J. Am. Chem. Soc.* **2001**, *123*, 12798.
13. Sun, S.; Zeng, H. *J. Am. Chem. Soc.* **2002**, *124*, 8204.
14. Liu, C.; Zou, B.; Rondinone, A.; Zhang, Z.J. *J. Phys. Chem. B* **2000**, *104*, 1141.
15. Sun, S.; Murray, C.B. *J. Appl. Phys.* **1999**, *85*, 4325.
16. Park, J.; Cheon, J. *J. Am. Chem. Soc.* **2001**, *123*, 5743.
17. Peng, X.; Wickham, J.; Alivisatos, A.P. *J. Am. Chem. Soc.* **1998**, *120*, 5343.
18. Talapin, D.V.; Rogach, A.L.; Kornowski, A.; Haase, M.; Weller, H. *Nano Lett.* **2001**, *1*, 207.
19. Klemmer, T.J.; Shukla, N.; Liu, C.; Wu, X.W.; Svedberg, E.B.; Mryasov, O.; Chantrell, R.W.; Weller, D.; Tanase, M.; Laughlin, D.E. *Appl. Phys. Lett.* **2002**, *81*, 2220.
20. Murray, C.B.; Kagan, C.R.; Bawendi, M.G. *Annu. Rev. Mater. Soc.* **2000**, *30*, 545.
20. Josephson, L.; Perez, J. M.; Weissleder, R. *Angew. Chem. Int. Ed.* **2001**, *40*, 3204.
21. van Leeuwen, D.A.; van Ruitenbeek, J.M.; de Jongh, L.J. *Phys Rev Lett* **1994**, *73*, 1432.

#### ***4. Synthesis of other magnetic alloy nanocrystals***

---

22. Sun, S.; Anders, S.; Hamann, H.F.; Thiele, J.U.; Baglin, J.E.E.; Thomson, T.; Fullerton, E.E.; Murray, C.B.; Terris, B.D. *J. Am. Chem. Soc.* **2002**, *124*, 2884.
23. Bawendi, M.; Mikulec, F.; Lee, J.K.; Kwanak-Gu. *American Patent* PCT/US99/21493, **2000**.

## 5. Magnetic properties of CoPt<sub>3</sub> nanocrystals

---

*The magnetic properties of CoPt<sub>3</sub> alloy nanocrystals were investigated. CoPt<sub>3</sub> nanocrystals exhibit superparamagnetic behaviour at room temperature. Magnetic measurement performed on monodisperse samples of differently sized non-interacting CoPt<sub>3</sub> nanocrystals revealed the size-dependence of blocking temperature, coercivity, remanent and saturation magnetisation. Significant influence of nature of the capping ligands on the magnetic properties was observed.*

---

### 5.1. Introduction into magnetic properties of nanocrystals

Magnetism is a result of moving charges. The magnetic properties of materials arise mainly from motion of electrons: the orbital motion of the electrons and the spin motion of the electrons. Other contributions like nuclear magnetic effects are usually much smaller compared to the electrons one. The electronic structure of a nanometer size metal particle is strongly size-dependent resulting in size-dependent magnetic behaviour. Many physical phenomena (magnetic domain size, exchange coupling effects, etc.) which determine experimentally observable magnetic properties of materials have natural length scales laying in the nano- and micrometer size range [1]

All materials interact with a magnetic field and this interaction can be either attractive toward a magnetic pole (ferro- and paramagnetism) or repulsive (diamagnetism). The application of a magnetic field ( $H$ ) results in a magnetization ( $M$ ) of a sample which can be measured by, e.g., a super-conductive quantum interference device (SQUID), one of the most popular and sensitive methods of investigating the magnetic properties. When a ferromagnetic material is magnetized by an increasing applied field and the field is then decreased, the magnetisation does not follow the initial magnetisation curve obtained during the increase of the magnetic field strength. This irreversibility is called hysteresis [1] (Figure 5.1). At high applied magnetic fields, the magnetisation approaches the maximum value called the saturation magnetisation ( $M_s$ ). Magnetic materials in a ferromagnetic state have a residual magnetisation, called remanent magnetisation ( $M_r$ ). Coercivity ( $H_c$ ) characterises the reverse-field strength needed to reduce the magnetisation to zero. Thus, the hysteresis measurements

directly yield the information about coercivity, remanent magnetisation and saturation magnetisation of a given material (Figure 5.1).

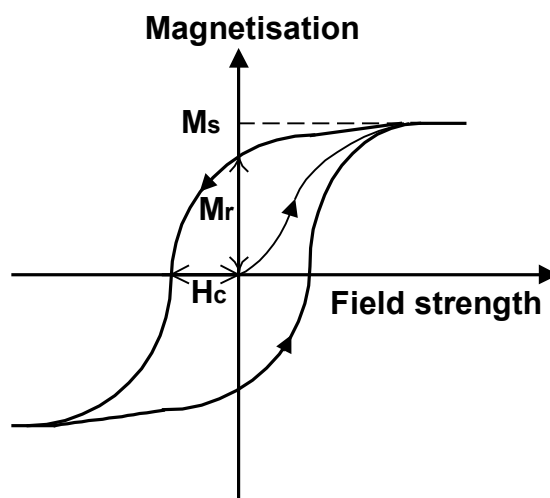


**Figure 5.1.** A typical hysteresis loop for a ferromagnetic material and the important magnetic parameters which can be obtained from the hysteresis loop. Dashed line shows the first scan.

Unfortunately, there is a curious mix of magnetic units in scientific and engineering literature. There are two widely used systems of units, the cgs (centimetre, gram, second) and the SI system. Thus, the magnetic field strength  $H$  can be measured in Oe (cgs) or in A/m (SI). Moreover, the applied field can be multiplied with the induction constant  $\mu_0$  and given in units of Gauss (cgs) or Tesla (SI). The magnetisation  $M$  is measured in emu/cm<sup>3</sup> (cgs) or A/m (SI) or, being multiplied with  $\mu_0$ , can also be given in Gauss or Tesla. Table 5.1 presents the magnetic units used in cgs and SI systems and some unit conversions.

**Table 5.21.** Magnetic units and unit conversions.

Magnetic units		cgs	SI	Conversion
Magnetic field strength	$H$	Oe (oersted)	A/m	1 kA/m = 12.57 Oe
Magnetisation	$M$	emu/cm <sup>3</sup>	A/m	1 emu/cm <sup>3</sup> = 10 <sup>3</sup> A/m
Magnetic flux density (induction)	$B$	G (gauss) B=H+4πM	T (tesla) B=μ <sub>0</sub> (H+M)	1 T = 10 <sup>4</sup> G
Induction constant	μ <sub>0</sub>	G/Oe	T/(A/m)	μ <sub>0</sub> = 1 G/Oe 4π·10 <sup>-7</sup> T/(A/m)

To minimise their energy, macroscopic ferromagnetic materials are broken into domains of parallel spins. Within a domain, the magnetic moments orient in one direction while the alignment of spins in neighbouring domains is usually antiparallel. The oppositely aligned magnetic domains are separated from each other by a domain wall. As the particle size decreases below some critical value the formation of domain walls become energetically unfavourable and ferromagnetic particle can support only a single domain. This critical size depends on material and is usually of order of tens of nanometers varying from ~14 nm for Fe up to ~170 nm for  $\gamma$ -Fe<sub>2</sub>O<sub>3</sub>. One can see that magnetic particles of nanometer size are usually single domains [2].

The dimensionless parameter – magnetic susceptibility ( $\chi$ ) defined as  $\chi = \partial M / \partial H$  is used to estimate the efficiency of applied magnetic field for magnetising a material. In many cases the susceptibility of a material depends on the direction in which it is measured. Such a situation is called magnetic anisotropy. The physical origin of magnetic anisotropy will be considered below. Now we would like only to emphasise that the anisotropy is an extremely important parameter determining the behaviour of a ferromagnetic material. When magnetic anisotropy exists, the total magnetisation of a system will prefer to lie along a special direction, called the easy axis of magnetisation. For a small single domain particle the energy associated with this alignment is called the anisotropy energy and in the simplest uniaxial approximation can be represented by  $E = KV \sin^2 \theta$ , where  $K$  - is the anisotropy constant,  $V$  the particle volume and  $\theta$  is the angle between the moment and the easy axes (Figure 5.2) [3]. The energy barrier  $\Delta E$  has to be overcome in order to rotate the magnetisation of a single domain particle. The height of this barrier  $\Delta E = KV$  is proportional to the particle volume and drops with decreasing the particle size. For small particles  $\Delta E$  may become compatible to thermal energy ( $kT$ ). In this case the energy barrier can no longer pin the magnetisation direction on the time scale of observation and rotation of the magnetisation direction occurs due to thermal fluctuations. Such a particle is said to be superparamagnetic. The coercivity of a superparamagnetic particles is zero ( $H_c = 0$ ) because thermal fluctuations prevent the existence of a stable magnetisation. Cooling of a superparamagnetic particle reduces the energy of thermal fluctuations and, at a certain temperature, the free movement of magnetization can be blocked by anisotropy. The temperature of the transition from superparamagnetic to ferromagnetic state is called the blocking temperature ( $T_B$ ).

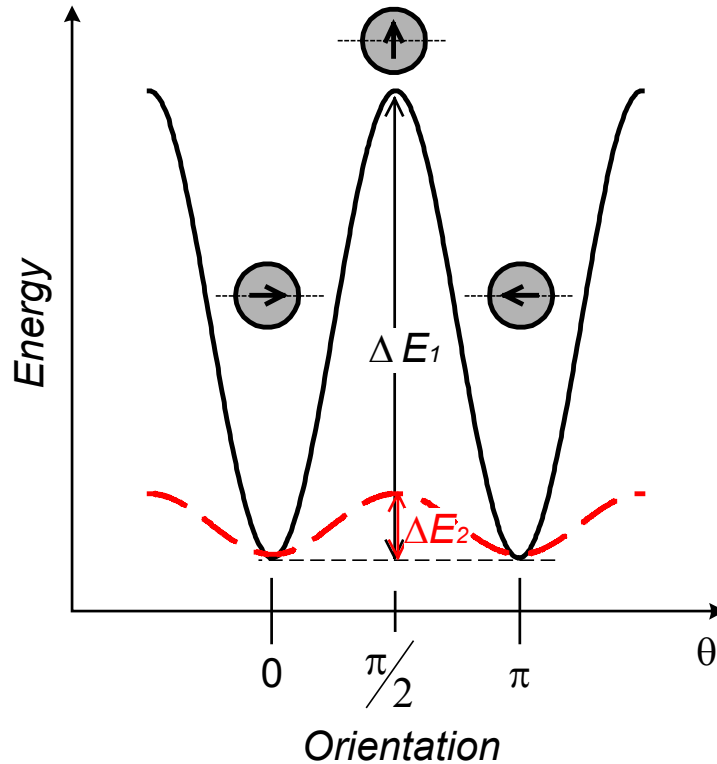


**Figure 5.2.** The energy associated with rotation of a magnetization direction for a uniaxial magnetic particle. The minima correspond to alignment of the magnetisation along the easy axis.  $\Delta E$  represents the energy barrier to the rotation of magnetisation. A two-fold decrease of the particle size results in an eight-fold reduce of the energy barrier (solid and dash lines, cf.  $\Delta E_1$  and  $\Delta E_2$ ).

When an external magnetic field interacts with the single-domain particle, an additional potential energy of  $E_f = -\vec{M}_s \cdot \vec{H}$  is supplied. Depending on the direction of the magnetic field with respect to the particle easy axis, the response of the particle moment to an applied field is different. Thus, if the field is applied perpendicular to the easy axis, the dependence of the particle potential energy on the magnetization direction evolves with the strength of applied field as shown in Figure 5.3a. The equilibrium direction of the magnetic moment, corresponding to the minimum of the total alignment energy  $E_{\text{tot}} = E_a + E_f$ , turns toward the field to the angle  $\theta = \arcsin(M_s H / (2KV))$ . At  $H = 2KV / M_s$  the moment aligns perpendicular to the easy axis (i.e. along the applied field) and magnetization approaches the saturation. In the  $M$  vs.  $H$  scans, the magnetization component parallel to the applied field changes linearly from  $-M_s$  to  $+M_s$  as shown in Figure 5.3c. Note that no magnetization

hysteresis is observed if the magnetic field is applied perpendicular to the easy axis of an uniaxial single-domain particle.

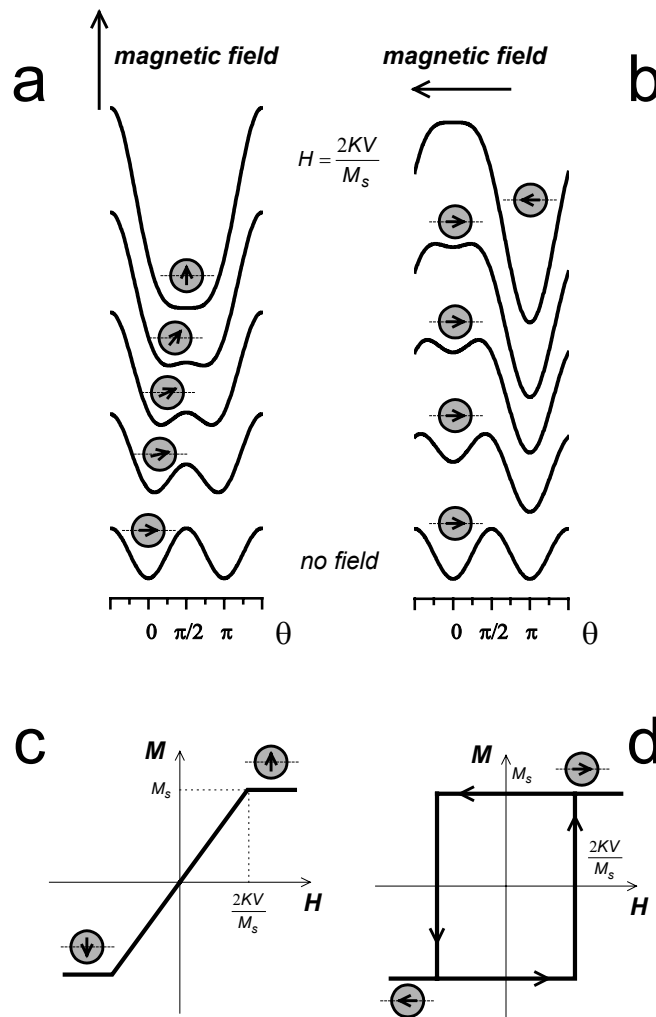


**Figure 5.3.** (a,b) Dependence of potential energy on the direction of a particle magnetic moment in presence of external magnetic fields applied (a) perpendicular and (b) parallel to the easy magnetization axis. The lower curves correspond to zero magnetic field and the upper ones correspond to the saturation magnetization when the magnetic moment align along the field. (c,d) Hysteresis loops for applied fields perpendicular (c) and parallel (d) to the easy axis of an uniaxial single-domain particle. The direction of easy magnetization axis is shown by dotted lines.

If a magnetic field is applied parallel to the easy axis, the particle moment can align either parallel or antiparallel to the field direction. The latter case is considered in Figure 5.3b. The alignment of the particle magnetization along the field is energetically favourable, however, in a relatively weak field the energy barrier blocks the magnetization reversal. The

height of the barrier decreases with increasing the field strength (Figure 5.3b). At  $H = 2KV/M_s$  the barrier vanishes and the particle magnetic moment jumps from antiparallel to the parallel alignment. This behavior leads to a square hysteresis loop with coersivity  $H_c = 2KV/M_s$  as shown in Figure 5.3d. The effect of magnetic field applied at any other angle to the particle easy axis can be evaluated in a similar manner.

As one can see, the response of an individual single-domain particle crucially depends on the direction of the applied magnetic field. The two situations considered above represent the extreme cases of the possible hysteresis curves, totally closed (no hysteresis) and totally open (square). Other orientations yield hysteresis curves between these limits. In reality, one usually has an ensemble of many particles with randomly oriented easy axes (Figure 5.4a) and the measured hysteresis loop is the result of averaging over all possible orientations. In an extremely strong magnetic field all particles align their moments along the field approaching the largest (saturation) magnetization. If the particles are fixed, e.g., dispersed in a solid non-magnetic matrix, the easy axes are randomly aligned and the magnetization occurs through rotation of the particle moments (Figure 5.4b). The time scale of this process is approx.  $10^{-9}$  s. However, the particles dispersed in a liquid can considerably decrease the potential energy aligning their easy axes along the external field (Figure 5.4c). This alignment occurs via the Brownian motion process when the particles strike with solvent molecules and is much slower ( $\sim 10^{-7}$  s for solvents like hexane) than the rotation of magnetic moment inside the particle.

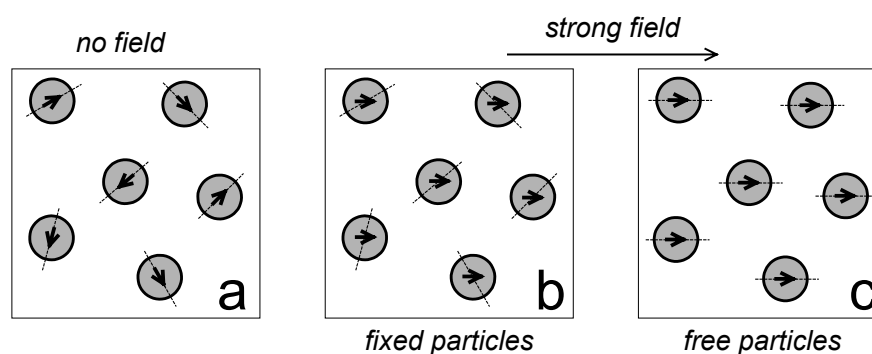
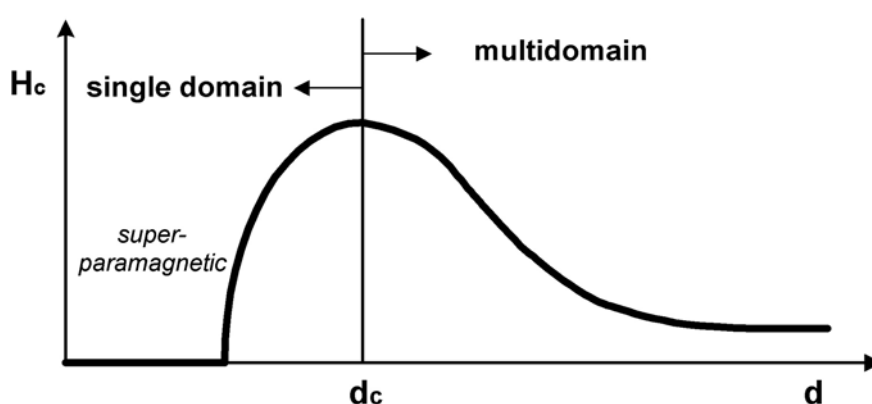


**Figure 5.4.** (a) An ensemble of magnetic particles with randomly distributed easy magnetization axe. (b) Magnetization of particle ensemble in a strong field via rotation of the particle magnetic moments. (c) Magnetic particles dispersed in a liquid can align their easy axes along the applied field. Directions of particle easy magnetization axes are shown by dotted lines.

The coercivity of a magnetic particle strongly depends on its size. Thus, if the particle is large enough to support multidomain structure, magnetisation reversal occurs through the domain walls motion [2]. This is relatively easy and, hence, the coercivity is low. On the other hand, in a single-domain particle the change of magnetisation direction can occur only by coherent rotation of spins, resulting in a considerably higher coercivity of single domain particles in comparison with multidomain ones (Figure 5.5)[1]. Upon further decrease of the particle size, the coercivity falls off due to progressively increasing role of the thermal fluctuations leading to superparamagnetism with  $H_c=0$  (Figure 5.2).



---

**Figure 5.5.** Particle coercivity vs. size. The largest coercivity is observed at the particle size  $d_c$  corresponding to the transition from multidomain to single domain structure.

Each magnetic nanoparticle is a single-domain magnet. To investigate the magnetic properties inherent to independent nanoparticles, the measurements have to be performed on an ensemble of uniform non-interacting nanoparticles. All sources of sample inhomogeneity (particle size and shape distribution, presence of particles with different crystalline modifications, polycrystalline particles, etc.) must be minimized. Interparticle interactions can be reduced by dissolving the particles in an appropriate solvent at a low concentration [3]. If a distribution of particle sizes is present, the initial susceptibility is more sensitive to the larger particles present whereas the approach to saturation is sensitive to the smallest particles of the sample [2]. In addition to the hysteresis measurements which allow estimating the coercivity and specific magnetization of a sample, *zero-field-cooled* (ZFC) and *field-cooled* (FC) measurements provide the information about the blocking temperature ( $T_B$ ).

In ZFC scans, a sample is cooled under zero applied magnetic field to a temperature well below the suspected  $T_B$ . The system is then warmed up and the magnetisation is

measured as a function of temperature by applying a relatively low external magnetic field. As the thermal energy increases, the moments align with the applied field and magnetisation increases. At the blocking temperature the magnetisation is maximal. Further growth of temperatures above  $T_B$  results in decrease of the magnetisation due to the effect of thermal energy causing fluctuation of magnetic moments of nanoparticles.

In the field-cooled (FC) scans a sample is cooled in a small external magnetic field, freezing-in a net alignment of the nanoparticle moments. The field is then removed, and the magnetisation is measured as the sample is slowly warmed up. Thermal energy unpins and randomizes the nanoparticle moments, lowering the sample's net magnetisation. Below  $T_B$  the free movement of magnetic moments is "blocked" by the anisotropy and so the particles are in a ferromagnetic state whereas above  $T_B$  the particles are characterised by superparamagnetic behaviour [4]. At blocking temperature ZFC and FC curves coverage [3]. The blocking temperature in a superparamagnetic system decreases with increasing applied measuring fields, being proportional to  $H^{2/3}$  at large magnetic fields and proportional to  $H^2$  at lower fields [2].

The magnetic anisotropy of nanocrystalline materials originates from the influence of crystal symmetry, shape and surface (or grain boundaries) effects. The most common anisotropies in the case of magnetic nanoparticles are *magnetocrystalline* and *shape* ones.

*Magnetocrystalline anisotropy* arises from the coupling of the electron spins to the electronic orbit, which, in turn, is coupled to the crystal lattice. The magnetisation is energetically favourable to align along a specific crystallographic direction called the easy axis of the material. In the case of hexagonal cobalt, the easy axis of magnetisation is the  $c$  axis. Magnetocrystalline anisotropy is intrinsic to a given material and independent of particle shape [2]. The easy and hard axes of Ni are  $\langle 111 \rangle$  and  $\langle 100 \rangle$  axes respectively, while in iron  $\langle 100 \rangle$  axes are considered as easy magnetisation axes [5]. Thus, in the case of cubic lattice symmetry multiple easy axes are formed.

In core-shell systems where metal core is surrounded by antiferro or ferrimagnetic oxide layers [2] *exchange anisotropy* can be observed [6]. This type of anisotropy is crucial in the case of small nanoparticles which can be easily oxidised, for example cobalt or iron nanoparticles [2]. Some molecular species adsorbed on surface of nanoparticles can also significantly influence the magnetic behaviour through the quenching of the surface atom contribution [7].

Non-spherical nanoparticles can possess also *shape anisotropy*. Shape anisotropy accounts for preferential orientation of the magnetisation along the long axis of an elongated

particle. The demagnetisation field is smaller in the long direction, because the induced poles at the surface are farther apart [1]. Shape anisotropy can produce large coercive forces. Advanced magnetic properties of the non-spherical nanoparticles attract great attention to the shape-controlled colloidal synthesis.

If the concentration of nanoparticles in a sample is high, magnetic moments of individual nanoparticles can interact and these dipolar interactions strongly affect the magnetic behaviour of the sample [8]. Interparticle interactions in 2D and 3D assemblies of magnetic nanoparticles result in the shift of the blocking temperature to higher values.

### 5.2. Characterisation of magnetic properties of CoPt<sub>3</sub> nanocrystals \*

All investigated sizes of CoPt<sub>3</sub> nanoparticles are below the critical size and hence CoPt<sub>3</sub> nanoparticles of investigated sizes are single domain. Also CoPt<sub>3</sub> magnetic particles are still small enough to be superparamagnetic and form stable colloidal solutions in an appropriate solvents. Since magnetic properties strongly depend on the particle size, monodispersity of nanoparticles is required. Size distribution in all our samples did not exceed 9 %. Nanocrystals of all sizes were refluxed at 270 °C to improve the crystallinity of CoPt<sub>3</sub> nanoparticles and avoid the influence of crystalline defects on the magnetic behaviour. The use of diluted solutions of magnetic particles allowed to minimise dipole interactions between the magnetic nanoparticles. Magnetic measurement were performed on CoPt<sub>3</sub> nanoparticles stabilised with HDA and ACA dispersed either in dodecane or in polylaurylmethacrylate (PLMA). The method of preparation of CoPt<sub>3</sub> nanocrystals immersed into polymer matrix is described in Experimental Section. TEM investigation of the CoPt<sub>3</sub> nanocrystals - polymer composite containing ~ 4.5 wt.% of 3.8 nm CoPt<sub>3</sub> nanocrystals reveals well separated nanocrystals randomly distributed in polymer matrix (Figure 5.6) and hence no interactions between CoPt<sub>3</sub> nanocrystals are expected.

---

\* This work was done in collaboration with Dr. Marina Spasova (Duisburg, Germany) and Örjan Festin and Prof. Dr. Peter Swendlith (Uppsala, Sweden).

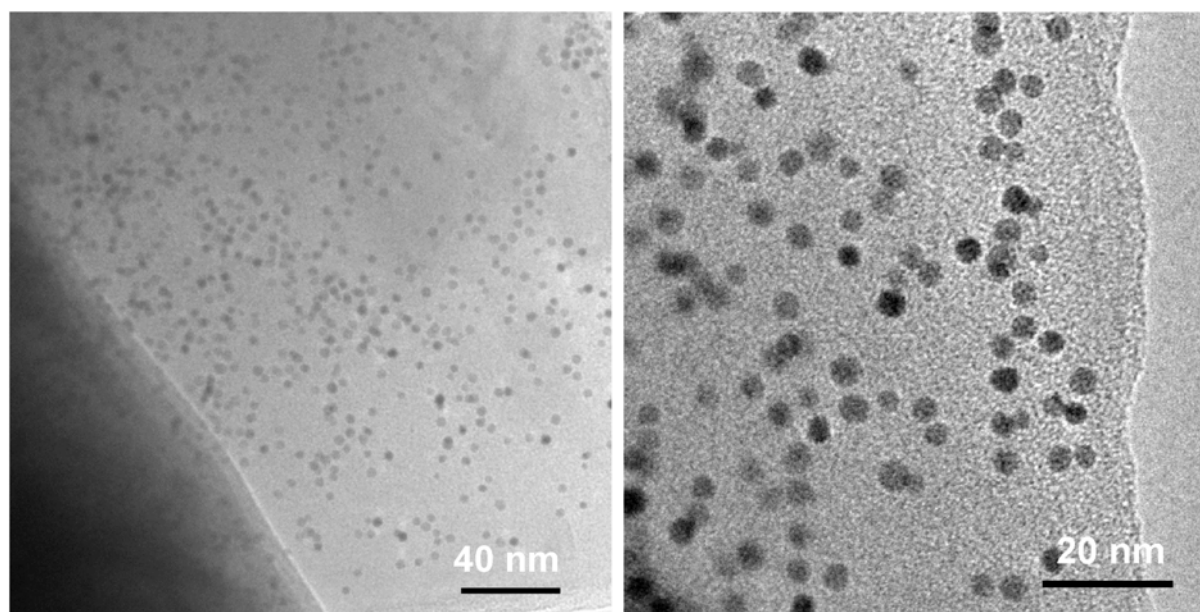


**Figure 5.6.** Overview (left) and closer look (right) TEM images of 3.8 nm  $\text{CoPt}_3$  nanocrystals distributed in the polymer (PLMA) matrix. The weight concentration of  $\text{CoPt}_3$  nanocrystals is 4.5 %.

The magnetisation of a size series of  $\text{CoPt}_3$  nanoparticles was measured as a function of field (up to 5000 Oe) and temperature (5-300 K) using a commercial SQUID magnetometer. The drop in the saturation magnetisation  $M_s$  with decrease of nanocrystal sizes was observed for  $\text{CoPt}_3$  nanocrystals stabilised with HDA and ACA (Figure 5.7). As expected, a decrease of the  $\text{CoPt}_3$  nanocrystal size results in the decrease of the coercivity, remanent and saturation magnetisation. Figure 5.8a summarises the size dependence of the coercivity, remanent and saturation magnetisation of  $\text{CoPt}_3$  nanocrystals stabilised with ACA and HDA. Similar results reported for hcp Co nanoparticles [3] were explained by increase in the nanoparticle surface-to-volume ratio and by the presence of several monolayers of cobalt oxide at the surface. In the case of  $\text{CoPt}_3$  nanocrystals the presence of cobalt oxides was not detected (Chapter 3), nevertheless, the influence of the surface effects can be significant due to ligand-metal interactions at the surface of nanocrystals [7,9,10]. Thus, complete quenching of the magnetic moment of the surface nickel atoms was reported for small nickel particles and  $\text{Ni}_{38}\text{Pt}_6$  clusters coated by carbonyl ligands [11]. The synthetic procedure of the preparation of  $\text{CoPt}_3$  nanocrystals includes thermodecomposition of  $\text{Co}_2(\text{CO})_8$  and despite the subsequent careful washing of as-synthesised  $\text{CoPt}_3$  nanocrystals the complete removal of carbonyl groups can be not achieved and thus some amount of carbonyl groups can present at the surface. Unfortunately, information about the presence of CO groups in our samples is not available

because of difficulty of analysis of extremely low concentrations of ligands at the surface of washed nanocrystals.

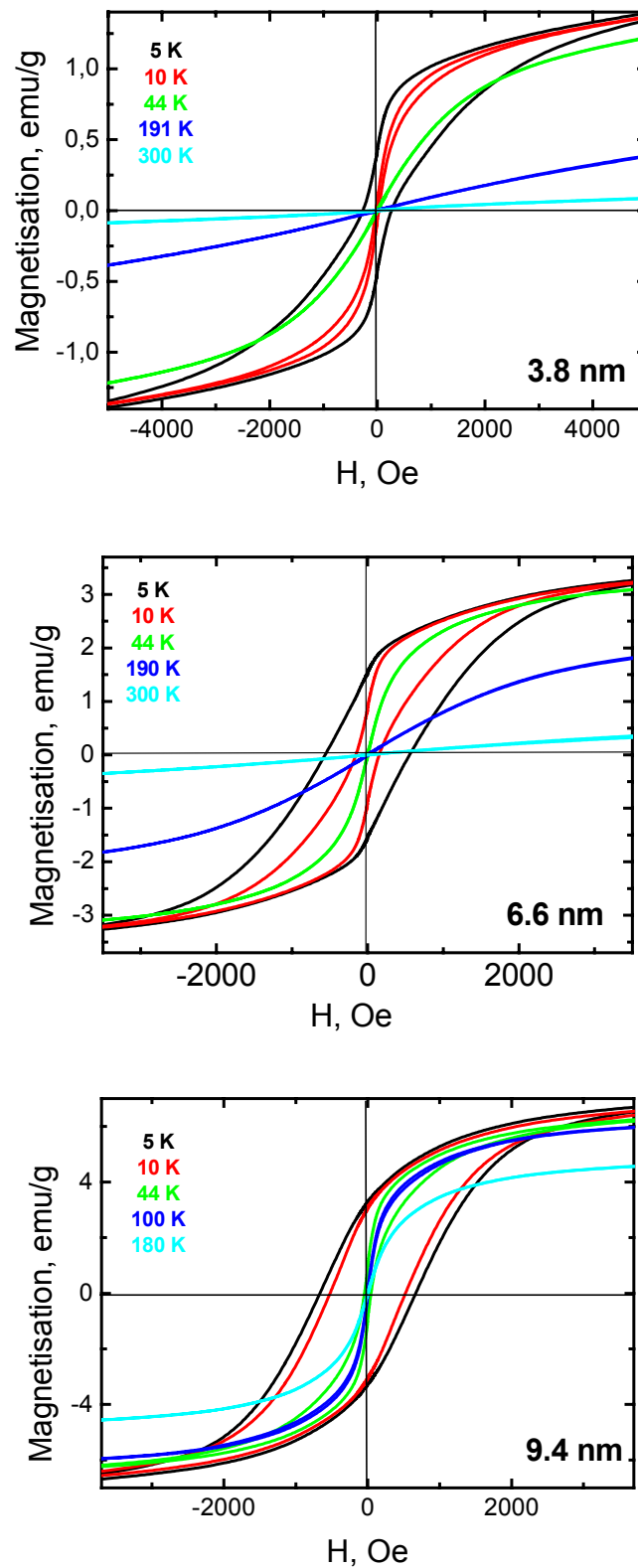


**Figure 5.7.** Experimental temperature-dependent hysteresis curves measured for  $\text{CoPt}_3$  nanocrystals of different sizes dissolved in dodecane.

The saturation magnetisation of bulk CoPt<sub>3</sub> is ~18.2 emu/g [11]. The values of the M<sub>s</sub> obtained in the case of nanoparticles are smaller: even the large ~9.4 nm CoPt<sub>3</sub> particles exhibit a saturation magnetisation of ~7.3 emu/g. The measured values of saturation magnetisation are usually normalised by the total weight of sample. In the case of nanoparticles, however, the surface of nanocrystals is covered by a ligand shell. Elemental analysis of 6.2 nm CoPt<sub>3</sub> nanocrystals showed that ~30 wt.% of the total nanoparticle weight is the weight of organic shell. Obviously, that in the case of 6.2 nm CoPt<sub>3</sub> nanocrystals the value of saturation magnetisation can be understated to 30 % if the correction of M<sub>s</sub> to the amount of outside nonmagnetic materials has not been carried out. It means that the investigation of the magnetic properties in the case of nanocrystals requires extremely precise control not only of size distribution and crystallinity but also of the amount of capping ligands in the investigated samples.

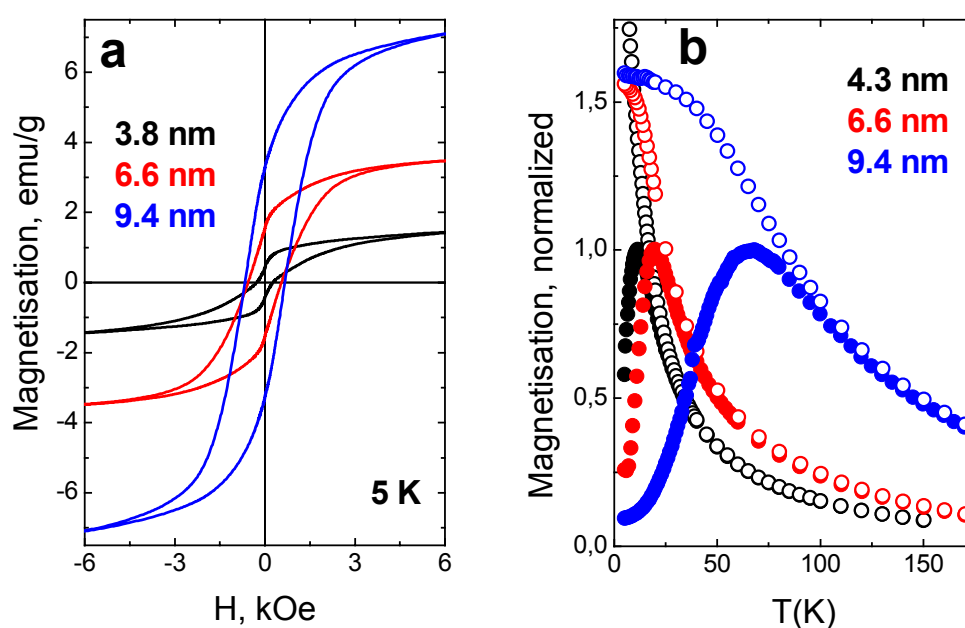


**Figure 5.8.** (a) Hysteresis loops of CoPt<sub>3</sub> nanocrystals measured at 5K; (b) ZFC/FC dependence of magnetisation for CoPt<sub>3</sub> nanocrystals of different sizes stabilised with HDA and ACA dissolved in dodecane.

At low temperature (e.g. 5-10 K), CoPt<sub>3</sub> nanocrystals of all investigated sizes are ferromagnetic (Figure 5.7, 5.8a). Coercivity (the field required to reverse the magnetisation) decreases with decreasing nanocrystal size, as seen in M versus H loops measured at 5 K (Figure 5.8a). Increasing thermal energy helps the nanoparticles reorient with the applied field H, reducing hysteresis and leading to superparamagnetic behaviour above the blocking

temperature (Figure 5.8b), where hysteresis drops to zero [3] (Figure 5.7). As expected, increase of particle size leads to higher values of the blocking temperature (Figure 5.8b).

Significantly higher values of saturation magnetisation and coercivity were observed for the PLMA composites of CoPt<sub>3</sub> nanocrystals (Figure 5.9). Thus 4 nm CoPt<sub>3</sub> nanocrystals dispersed in polymer matrix have at 5K saturation magnetisation  $\sim 5.5$  emu/g and coercivity  $\sim 670$  Oe. while nanocrystals of the same size being dissolved in dodecane have  $M_s \sim 1.6$  emu/g and  $H_c \sim 255$  Oe. These observation can serve as another example illustrating the significance of surface effects for magnetic nanocrystals.

At the surface, the coordinative number of each surface atom is smaller than within the bulk. *d*-band of a collection of transition metal atoms at the surface is narrower than in the bulk, leading to a high density of states and hence enhanced magnetisation [1]. Thus, the surface magnetic moments can be enhance by 10-30 % over their bulk values [1]. However, electron donation of *d*-band by ligands can partially fill the unpaired hole and suppress the magnetic moment in a straightforward manner [1]. Thus we can assume that if capping agents are electron donors their presence at the surface of magnetic nanocrystals can result in a decrease of the magnetisation of the sample. The difference between these two samples is the different concentration of HDA at the surface of nanocrystals. To prepare polymer magnetic composite, the surface of CoPt<sub>3</sub> nanocrystals was modified by laurylmethacrylate (LMA) by the following surface-exchange procedure: CoPt<sub>3</sub> nanocrystals were thoroughly washed to remove surface ligands (washing with *i*-PrOH was repeated till the full precipitation of CoPt<sub>3</sub> nanocrystals); then LMA was added to dry powder of nanocrystals and CoPt<sub>3</sub> nanocrystals slowly re-dissolved in LMA forming a clear solution. We assume that HDA is object of a reversible, dynamic surface equilibrium and by this way significant amount of HDA can be removed from the surface of nanocrystals. CoPt<sub>3</sub> nanocrystals dissolved in dodecane, on the other hand, probably, contain much more HDA serving as an electron donor. Also magnetic measurements carried out on the precipitated and thoroughly washed nanocrystals revealed significantly higher values of the coercivity and saturation magnetisation. However, whether such a significant increase of  $M_s$  and  $H_c$  can be explained only by surface effect is still not clear.

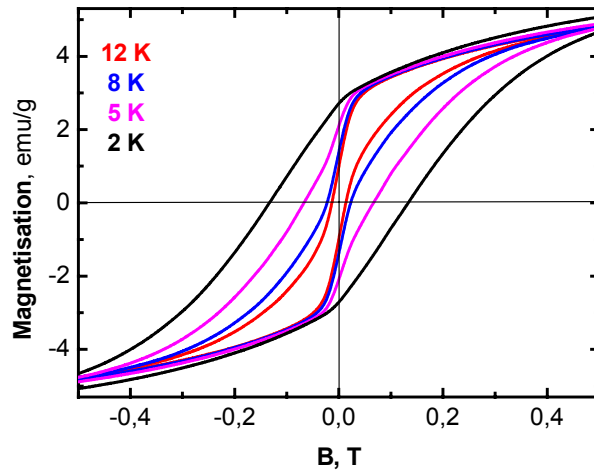


**Figure 5.9.** Experimental hysteresis curves measured at different temperature for non-interacting 4.0 nm  $\text{CoPt}_3$  nanocrystals dissolved in the polymer matrix (PLMA). ( $1T \sim 10000$  Oe).

In the case of high nanoparticles concentration dipolar interactions between particles strongly affect the behaviour of the dispersion [8]. Interparticle interactions in 2D and 3D assemblies of magnetic nanoparticles result in a shift of the blocking temperature to higher values. Such an increase of  $T_b$  was observed in the case of 2D arrays formed from 4 nm  $\text{CoPt}_3$  nanoparticles (Figure 5.10).

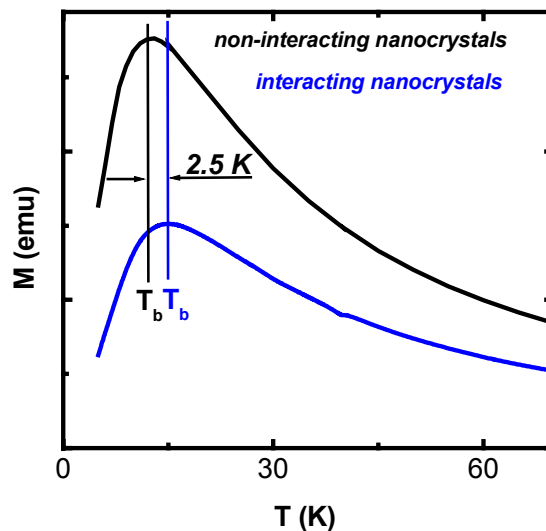


**Figure 5.10.** Temperature dependence low-field magnetization, measured at 100 Oe (ZFC) for 4 nm  $\text{CoPt}_3$  nanoparticles: (a) non-interacting nanocrystals (1.5 wt.% in PLMA matrix  $\approx 0.08$  vol.%) -  $T_b = 12.6$  K; (b) interacting nanoparticles deposited on a Si substrate -  $T_b = 15.1$  K.

The blocking temperature was found to be higher for interacting nanoparticles due to interparticle magnetic dipolar interactions. ZFC scan of 4 nm CoPt<sub>3</sub> nanoparticles dispersed in PLMA reveals a sharp maximum at 12.6 K. The same 4 nm CoPt<sub>3</sub> nanoparticles precipitated on a silicon substrate and self-assembled into 2D and 3D structures exhibit higher blocking temperature of ~ 15.1 K and their ZFC scan is broader (Figure 5.10).

These results are in a good agreement with previously reported results for other magnetic materials. Thus increase of  $T_b$  by 5 K was observed for 5.8 nm cobalt particles arranged in a 2D network in comparison with isolated non-interacting particles [4]. The shift and broadening of ZFC/FC scans were also observed in the case of closely packed assemblies of monodisperse nickel and cobalt nanoparticles [1,3]. Moreover, further decrease\* of the interparticle distance in the self-assembled array of nickel nanoparticles lead to further shift of  $T_b$  [3]. In turn, diluting of the close-packed arrays of 9 nm cobalt particles ( $T_b$  165 K) with 1-octadecylamine was reported to reduce the magneto-static coupling of particles and result in a sharper transition at 105 K [12].

To form stable colloidal solution, concentration of ~ 4 nm CoPt<sub>3</sub> nanocrystals in dodecane should be below ~11 wt.% (for larger nanocrystals these values are smaller: ~5 wt.% for 9 nm CoPt<sub>3</sub> nanocrystals). At relatively high concentration of magnetic nanocrystals in solution, surface ligands can not prevent the attractive magnetic interactions between nanocrystals and hence an overall stability of magnetic colloids tends to decrease. The limit concentration of nanocrystals in colloidal solution strongly depends not only on the nanocrystal size but also on the solvent. Thus, a ~21 wt.% solution of 6.5 nm CoPt<sub>3</sub> nanocrystals can be prepared in polylaurylmethacrylate. No visible shift of the maxima and no broadening of ZFC curves were observed and, hence, no interactions between the nanocrystals were found (Figure 5.11).

---

\* The decrease of the interparticle distance was achieved by annealing under vacuum which lead to the partial desorbtion of surfactant from surface of nanoparticles.

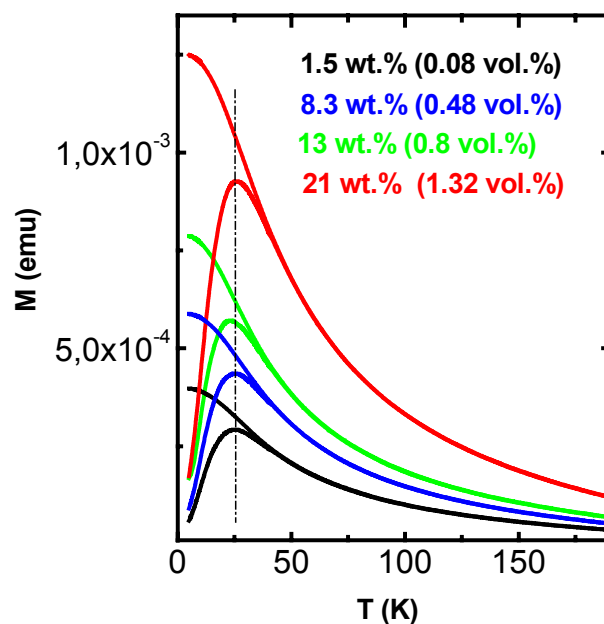


**Figure 5.11.** ZF/ZFC scans measured at 100 Oe for 6.5 nm  $\text{CoPt}_3$  nanoparticles in PLMA matrix for various concentration as it is shown in the figure.

### 5.3. Conclusions

Magnetic properties of non-interacting magnetic nanocrystals can be investigated either in a dilute colloidal solution or on the magnetic nanocrystals immersed into a polymer matrix. Nanocrystal - polymer composites have some advantages because of their higher stability against oxidation and improved passivation of the nanocrystal surface by a polymer matrix. Additionally, polymer matrix prevents the coagulation of nanocrystals and the properties of such samples are constant for a long period of time. The magnetic measurements (hysteresis loops and ZFC/FC scans) revealed a superparamagnetic behaviour of  $\text{CoPt}_3$  nanocrystals. The blocking temperature and coercivity strongly depend on the nanocrystal size. The nature of capping ligands affects the magnetic behaviour of  $\text{CoPt}_3$  nanocrystals. Dipolar interactions between magnetic nanoparticles packed into 2D and 3D assemblies lead to an increase of the blocking temperature.

## 5.4. References

1. Kenneth J. Klabunde, *Nanoscale Materials in Chemistry*, John Wiley & Sons, Inc. **2001** (Sorensen, C.M. *Magnetism* pp. 162-221).
2. Leslie-Pelecky, D.L.; Rieke, R.D. *Chem. Mater.* **1996**, *8*, 1770.
3. Murray, C.B.; Sun, S.; Doyle, H.; Betley, T. *MRS Bulletin* **2001**, 985.
4. Petit, C.; Taleb, A.; Pileni, M.P. *Adv. Mater.* **1998**, *10*, 259.
5. Kittel, C. *Introduction to solid state physics*, New York, Singapore, John Wiley & Sons, 1996.
6. Meiklejohn, W.H.; Bean, C.P. *Phys. Rev.* **1957**, *105*, 904.
7. van Leeuwen, D. A.; van Ruitenbeek, J. M.; de Jongh, L. J.; Ceriotti, A.; Pacchioni, G. *Phys. Rev. Lett.* **1994**, *73*, 1432–1435.
8. Held, G.A.; Grinstein, G.; Doyle, H.; Sun, S.; Murray C.B. *Phys. Rev. B* **2001**, *64*, 012408.
9. Russier, V; Petit, C.; Legrand, J.; Pileni M. P. *Phys. Rev. B* **2000**, *62*, 3910-3916.
10. Bødker, F.; Mørup, S.; Linderøth, S. *Phys. Rev. Lett.* **1994**, *72*, 282–285.
11. Rooney, P.W.; Shapiro, A.L.; Tran, M.Q.; Hellman, F. *Phys. Rev. Lett.* **1995**, *75*, 1843.
12. Sun, S.; Murray, C. B. *J. Appl. Phys.* **1999**, *85*, 4325.



## 6. Self-assembly of magnetic alloy nanocrystals

---

*Monodisperse highly crystalline PtFe and CoPt<sub>3</sub> can organise themselves into ordered one- (1D), two- (2D) and three-(3D)-dimensional structures. Ordered structures of nanocrystals were characterized by TEM, HRTEM, SEM, HRSEM and AFM methods. The proposed technique of controlled oversaturation of a colloidal solution leads to the formation of macroscopic (~tens micrometers) colloidal crystals consisting of monodisperse nanocrystals as building blocks. Engineering of the size-ratio of CoPt<sub>3</sub> nanocrystals induced nanoparticle samples with two different mean sizes to the formation of AB<sub>5</sub> type superlattice isostructural to the intermetallic compound CaCu<sub>5</sub>. Self-assembly of magnetic nanocrystals in an external magnetic field results in the formation of glassy-like structures with preferably short-range ordering of nanocrystals.*

---

### 6.1. Introduction

The nanocrystals synthesised by methods of colloidal chemistry consist of an inorganic crystalline core capped with a shell of organic surface ligands. The ligand shell prevents agglomeration of nanocrystals in a colloidal solution and determines the interparticle spacing in their ordered one-(1D), two-(2D) and three-(3D) dimensional superstructures. The assembly of monodisperse magnetic particles into superstructures is considered as an important step toward fabrication of functional devices made from individual nanocrystals as building blocks. The organisation of magnetic nanocrystals into ordered structures occurs due to attractive interactions of van der Waals or their magnetic nature [1-3]. However, too strong interparticle interactions can disturb self-assembly of nanocrystals. Usually slow destabilisation of a colloidal solution (for example, slow evaporation of a highly boiling solvent) results in the formation of an ordered superstructure. On the other hand, too fast destabilisation or strong dipole-dipole interactions between nanocrystals lead to the formation of mainly dis-ordered structures or structures with only local ordering of nanocrystals [1,4].

Potentially, self-assembly of colloidal nanocrystals can reach the precision of lithographically produced arrays on the nanometer length scale. Assemblies of metal and semiconductor nanoparticles can also be considered as a model system for investigating

collective transport and optical phenomena in ordered structures [5-7]. However, magnetostatic particle interactions in the close-packed arrays can result in a broad transition from superparamagnetic to ferromagnetic behaviour [8].

In this Chapter the formation of 1D, 2D and 3D superstructures of magnetic alloy nanocrystals is discussed. The method of controlled oversaturation allows to obtain 3D ordered regular-shaped colloidal “supercrystals” with the size of ~10 – 30  $\mu\text{m}$ . Binary nanocrystal mixtures lead to the formation of ordered bimodal assemblies.

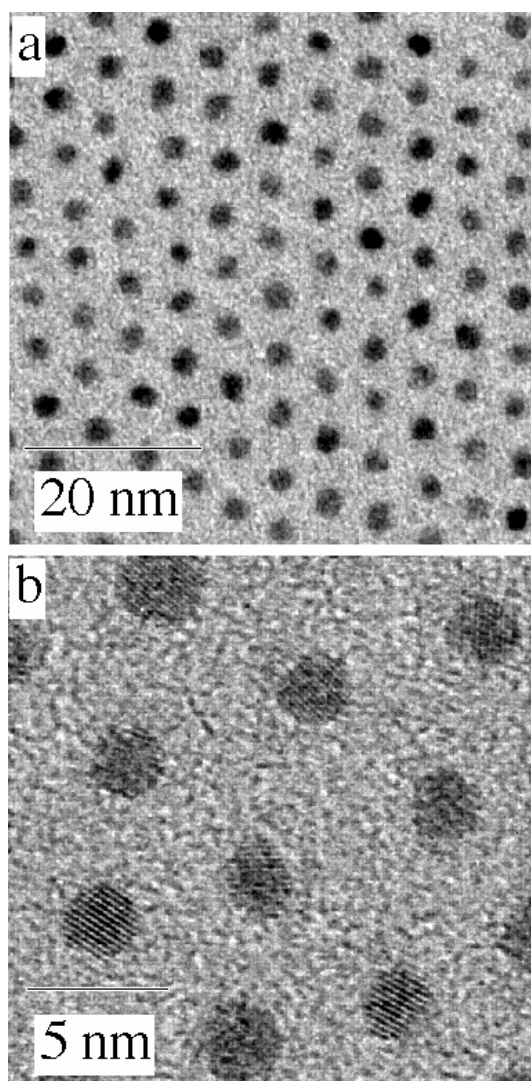
## **6.2. Formation of 2D and 3D superlattices from monodisperse magnetic nanocrystals**

Self-assembly of monodisperse nanocrystals under different conditions of destabilisation of a colloidal solution can result in the formation of either close-packed glassy films or long-range ordered superlattices. Close-packed glassy films possessing a short-range order can be formed if the evaporation rate of a solvent is relatively high [1]. Superlattices with low concentration of lattice defects and a long-range order of nanocrystal arrangement are formed if the particles are mobile enough and have enough time to find their lowest energy sites in the superstructure. Thus, slow evaporation of a highly boiling carrier solvent at increased temperatures (50-60°C) is favourable for the formation of ordered superstructures [1]. In addition to 2D and 3D superstructures known for monodisperse semiconductor nanocrystals and latex spheres, some specific self-organised structures inherent only to magnetic nanocrystals were reported. Thus, spherical Co nanocrystals can organise themselves into pearl-like aggregates and even form bracelet-like rings in order to minimise the magnetostatic energy [9,10].

The wetting properties of the substrate can influence the superlattice morphology [11]. If a colloidal solution of nanoparticles wets the substrate, the 2D superlattice grows preferably forming a monolayer. As the surface coverage increases, the nanocrystals adsorb to the edges and kinks of the growing structure, forming terraces that extend laterally across the substrate. If the colloidal solution does not wet the substrate, a 3D superlattice preferably grows, with facets reflecting the packing symmetry.

FePt nanocrystals with narrow size distributions prepared by the OA-oleyl amine method of Sun et al [12] tend to organise themselves into ordered arrays whose quality strongly depends on the deposition conditions [3,13]. Figure 6.1 shows an image of a

hexagonal 2D array of 2.5 nm large FePt nanoparticles self-assembled on a TEM grid. The regular interparticle spacing of  $\sim 40$  Å is determined by the capping ligands (OA – oleyl amine). The ligands maintain the interparticle distance within self-assembled superstructures and determine the spacing between the nearest neighbors. Thus, the possibility of exchange of OA and oleyl amine with shorter ligands allows to tune the interparticle distances within a superlattice as has been demonstrated in Ref. [12].



---

**Figure 6.1.** A hexagonal close-packed 2D array of FePt nanocrystals on a TEM grid.

Depending on the preparation conditions, different types of films of FePt nanocrystals can be formed. Figure 6.2 shows the X-ray diffraction (XRD) patterns of two films, measured in the small-angle and the wide-angle regions. Film A was obtained by evaporating a concentrated solution of 4.5 nm FePt nanoparticles in hexane (boiling point is 69°C and hence

the evaporation rate of solvent is high), whereas film B was prepared from a dilute solution of the same nanoparticles in toluene (boiling point is 110°C and hence slower evaporation rate). The XRD data confirm the tendency of nanocrystals to form organized structures, as it is seen from the pronounced reflexes in the small-angle region of both films. The appearance of up to 6 equidistant reflexes with a monotonic decrease of their intensities in the small-angle XRD pattern of sample B might be evidence of a layered structure of the film. Preferential orientation of the nanocrystals inside film B was confirmed by a strong enhancement of the (200) fcc peak in the wide-angle XRD spectrum of this sample. This enhancement is not observed in sample A whose diffraction pattern is consistent with randomly oriented nanocrystals of the fcc FePt phase.

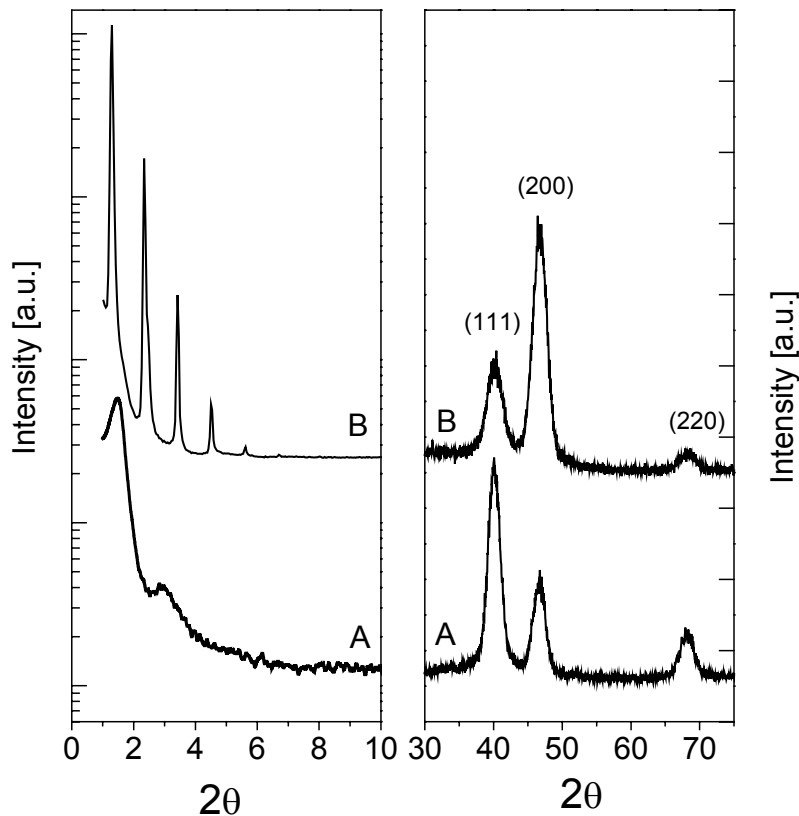


**Figure 6.2.** XRD patterns of two different films composed of FePt nanocrystals (samples A and B) measured in the small-angle and the wide-angle region.

Owing to their narrow particle size distributions and the uniform spherical shape, the CoPt<sub>3</sub> nanocrystals also have a strong tendency to self-organise into 2D and 3D superstructures [3,14]. Spontaneous self-assembly was observed when colloidal solutions of

CoPt<sub>3</sub> nanocrystals were spread onto a substrate with subsequent slow evaporating of the carrier solvent. Usually nanoparticles tend to organise themselves into 3D dense structures. In such structures nanoparticles play the role of artificial atoms. The highest density of nanoparticle package (the fill factor is ~ 74 %) is achieved for the face centred cubic and hexagonal lattices. If the surface coverage with nanocrystals is only one or two monolayers there is no difference between cubic and hexagonal arrangements of nanoparticles (Figure 6.3, *left image*). The difference between these two types of package originates from the arrangement of the nanoparticles of the third layer relatively to the first one. If nanoparticles of the third layer prefer to occupy the spatial positions above the nanoparticles in the first monolayer, a hexagonal 3D lattice of nanoparticles is formed (Figure 6.3, *low right image*). If nanoparticles of the third layer strike between the particles in the first layer, cubic package is achieved (Figure 6.3, *top right image*). In other words, in the case of hexagonal structure AB arrangement of nanoparticle layers is realised, while the cubic structure is characterised by ABC arrangement of nanoparticles.

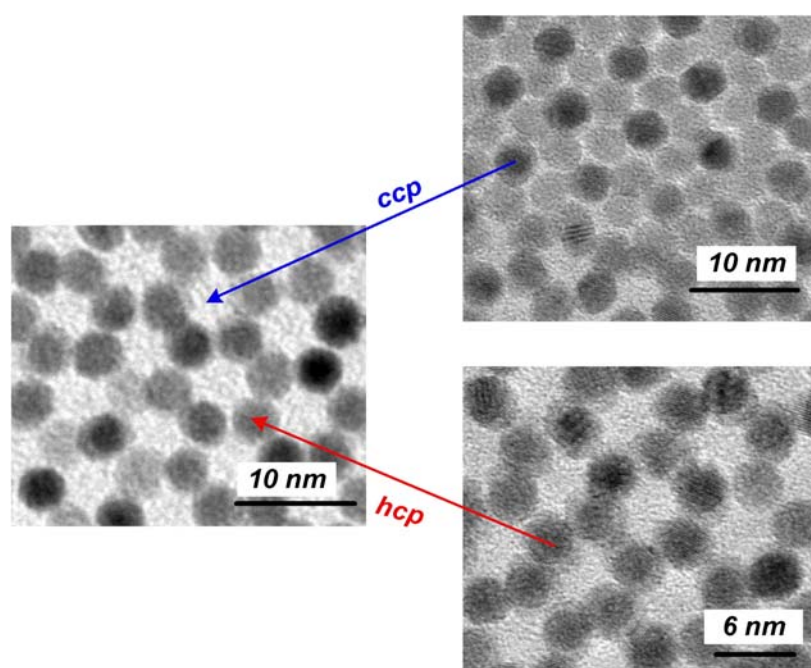


**Figure 6.3.** A series of TEM images demonstrating the formation of two possible dense packed structures of CoPt<sub>3</sub> nanoparticles.: cubic close packed (ccp) (top image) and hexagonal close packed (hcp) (low image)

Figure 6.4 illustrates step by step the transition from 2D to 3D cubic superstructure of CoPt<sub>3</sub> nanocrystals. Figure 6.4a shows a TEM overview image of a closely packed monolayer of 4.8 nm CoPt<sub>3</sub> nanocrystals. If the surface coverage with nanocrystals was higher than one monolayer, nanocrystals of the 2<sup>nd</sup> layer occupied positions between the nanocrystals in the 1<sup>st</sup> layer (Figure 6.4b, 6.46c). CoPt<sub>3</sub> nanocrystals are separated by large interparticle spacing of

~2.5 nm maintained by the bulky ACA and HDA capping ligands. The nanocrystals of the 3<sup>rd</sup> layer occupied the positions typical for cubic close packing ccp structure (Figure 6.4d, 6.4e). Figure 6.4e gives a magnified image of a three layered assembly of ~4.0 nm CoPt<sub>3</sub> nanocrystals. The difference in phase contrast between two underlying layers and darker third layer allows to attribute each nanocrystal to the layer it is placed in and permits us to conclude that CoPt<sub>3</sub> nanocrystals are packed into ccp-like superlattice where the nanocrystals are separated from each other by thick (2.5 nm) organic shells. Figure 6.4f presents a TEM image of multilayer 3D superlattice where the 4.5 nm CoPt<sub>3</sub> nanocrystals are arranged in a nearly defect-free 3D structure exhibiting long-range order. Graphical illustration shown in Figure 6.4g clarifies the three-layer arrangement of CoPt<sub>3</sub> nanocrystals observed in Figure 6.4e.

The assembly of nanocrystals with bimodal size distributions represent a very interesting aspect of self-organisation. Binary assemblies of submicron colloidal particles have been investigated theoretically and experimentally. Bimodal assemblies of latex globules lead to the formation of phases such as AB<sub>2</sub>, AB<sub>13</sub> and AB<sub>5</sub> [15,16]. The first examples of binary assembly of nanometer sized particles were observed for thiol stabilised gold and silver nanocrystals. Mixtures of Au [17] or Au and Ag [18] nanoparticles of two different sizes formed nanoscale colloidal alloy (2D superlattices). Formation of both AB and AB<sub>2</sub> alloy phases is possible and depends on the size and the particle number ratio. The experimental data obtained by Shiffrin *et al.* [17,18] for the mixed AB and AB<sub>2</sub> phases of bimodal ensembles of nanoparticles agreed well with the previously derived geometrical rules for micrometer-size particles [19] governing the formation of either AB ( $0.27 < R_A/R_B < 0.425$ ) or AB<sub>2</sub> ( $0.482 < R_A/R_B < 0.624$ ) phases from monodisperse hard spheres of radii R<sub>A</sub> and R<sub>B</sub>. When two monodisperse colloids of CoPt<sub>3</sub> nanocrystals (4.5 nm and 2.6 nm diameter) were mixed together and the solvent was slow evaporated, an AB<sub>5</sub>-type superlattice analogous to the structure of CaCu<sub>5</sub> intermetallic compound [20] was obtained (Figure 6.5a). A similar structure was observed for binary mixtures of latex spheres of two different sizes: 550 nm and 310 nm [16]. In the first plane of this lattice (Figure 6.5c), each 4.5 nm CoPt<sub>3</sub> nanocrystal is surrounded with a hexagon formed by 2.6 nm nanocrystals. The second plane consists only of hexagons of small particles which are, however, rotationally shifted by 30° relative to the first plane, and the third plane repeats the first one.

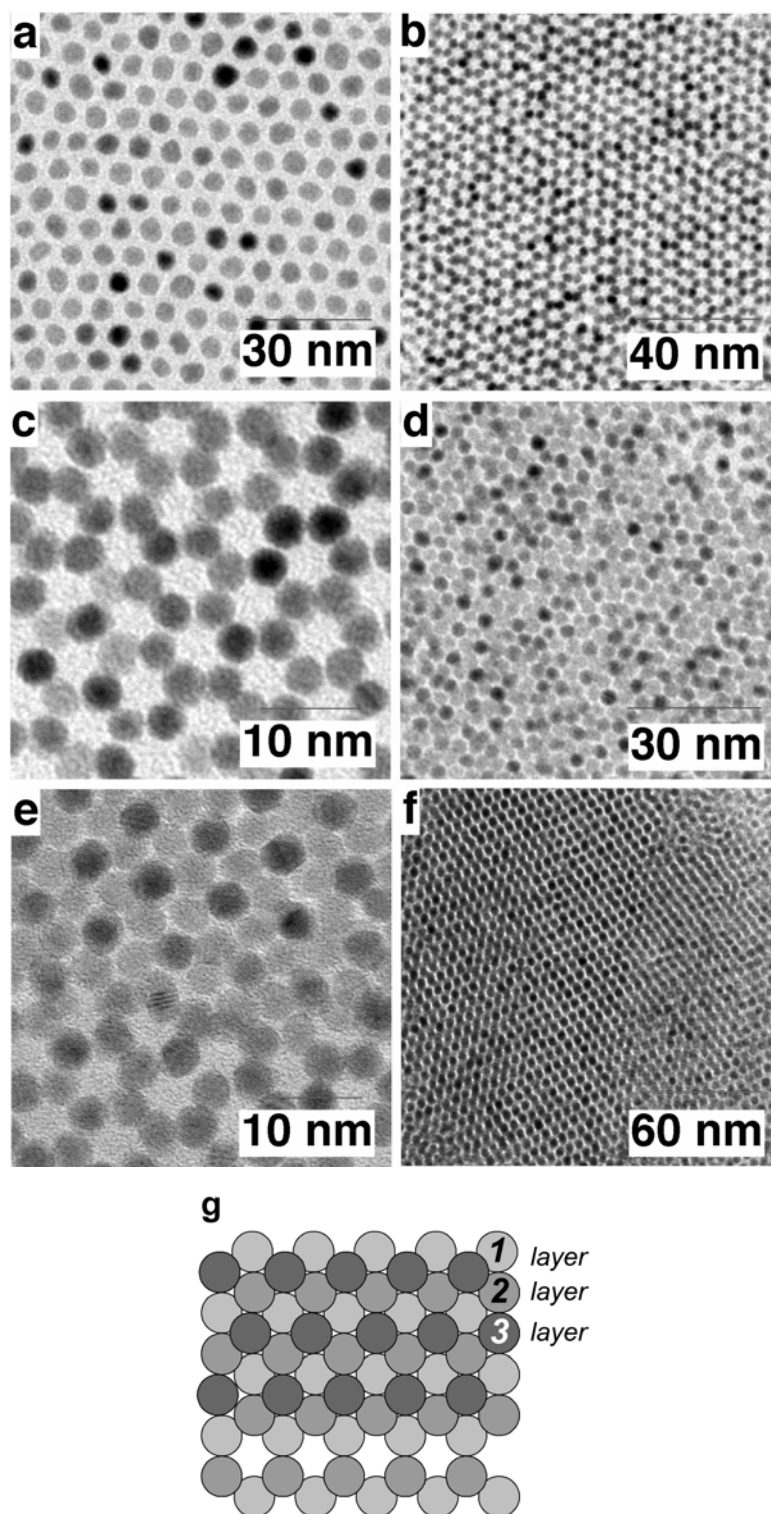


**Figure 6.4.** TEM images of (a) a monolayer of 4.8 nm  $\text{CoPt}_3$  nanoparticles; two layers of 3.6 (b) and 4.0 (c) nm  $\text{CoPt}_3$  nanoparticles; (d) three layers of 3.6 nm  $\text{CoPt}_3$  nanoparticles; (e) three layers of 4.0 nm  $\text{CoPt}_3$  nanoparticles; (f) more than five layers of 4.5 nm  $\text{CoPt}_3$  nanoparticles; (g) graphical illustration of a three-layer arrangement of  $\text{CoPt}_3$  nanocrystals

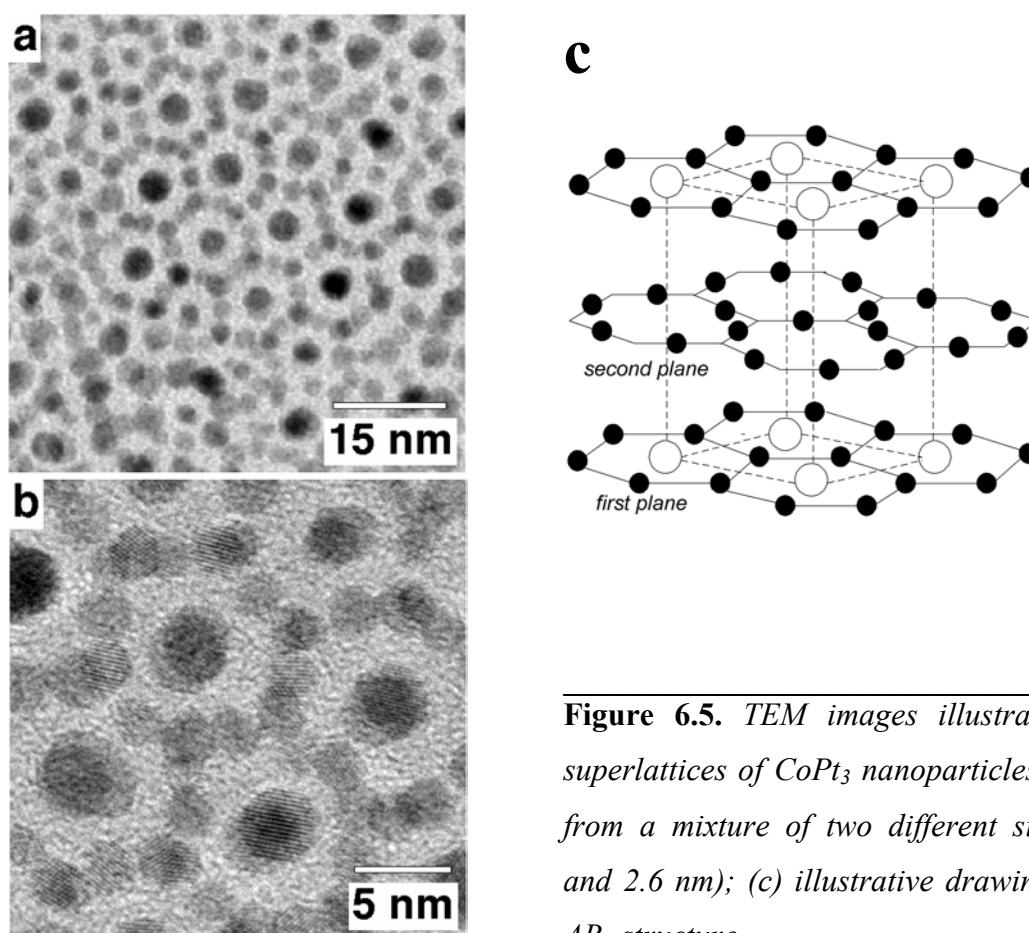


**Figure 6.5.** TEM images illustrating 3D superlattices of  $\text{CoPt}_3$  nanoparticles formed from a mixture of two different sizes (4.5 and 2.6 nm); (c) illustrative drawing of the  $\text{AB}_5$  structure.

Ordered superlattices formed from nanocrystals with different chemical composition are of a great interest because of the possibility to combine different (e.g. magnetic and semiconductor) properties in the resulting material. For example, 2D or 3D superstructures constructed from magnetically hard and soft materials are promising for advanced permanent magnets. Thus, self-assembly of  $\text{FePt}$  and  $\text{Fe}_3\text{O}_4$  nanocrystals was used to build the exchange-coupled nanocomposite magnets with high energy product. The binary assemblies of  $\text{FePt}$  and  $\text{Fe}_3\text{O}_4$  nanocrystals were further converted into  $\text{FePt-FePt}_3$  nanocomposite by annealing at  $\sim 650$  °C under flow of argon containing 5% hydrogen [21]. Ordered structures of magnetic and luminescent semiconductor nanoparticles are expected to exhibit an interesting behaviour arising from the influence of the local magnetic fields on the optical properties. In order to obtain such bimodal structures, differently-sized spherical  $\text{CoPt}_3$  and  $\text{CdSe}$  nanocrystals were co-precipitated from a toluene solution. Figure 6.6 shows an example of assembly of  $\sim 6.5$  nm  $\text{CoPt}_3$  nanocrystals stabilised by ACA and HDA and  $\sim 4.0$  nm  $\text{CdSe}$  nanocrystals stabilised by TOP and HDA. The TEM image of formed bimodal assemble revealed  $\text{AB}_2$  structure (compare Figure 6.6, bottom left and right images).  $\text{AB}_2$  arrangement is typical for the mixture of large (A) and small (B) hard spheres with a radii ratio between  $0.482 < R_B/R_A <$

0.624 [17].  $R_{\text{CdSe}}/R_{\text{CoPt}_3}$  ratio of our nanoparticles is  $\sim 0.615$  (or  $\sim 0.622$  if take into account the ligands shells) and the formation of the  $\text{AB}_2$  structure can be expected. However, magnetic and semiconductor nanoparticles are separated by a shorter distance than the width of particle stabilising shells. As it is concluded from TEM investigation of arrays consisting from only magnetic or semiconductor nanoparticles, HDA and ACA capping molecules form  $\sim 1.2 - 1.3$  nm thick organic shell around the  $\text{CoPt}_3$  nanoparticles whereas CdSe nanoparticles are surrounded by a shell of  $\sim 0.8$  nm.

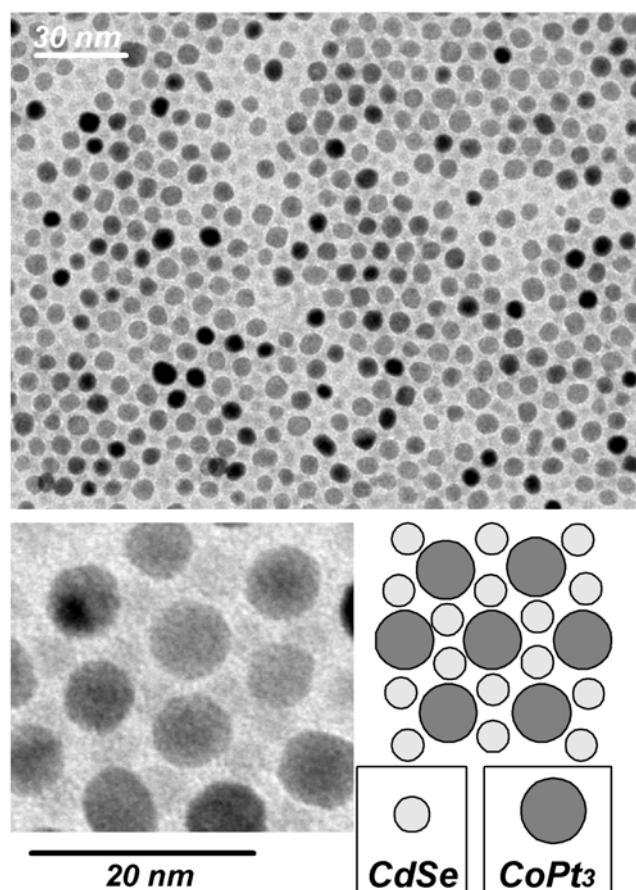
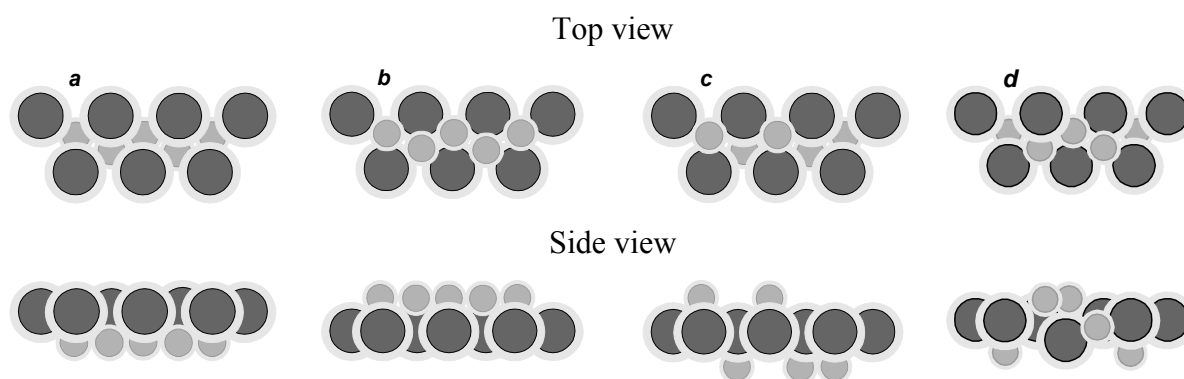


**Figure 6.6.** An ordered array comprising  $\text{CoPt}_3$  nanoparticles of  $\sim 6.5$  nm and CdSe nanoparticles of  $\sim 4$  nm.

This means that  $\text{CoPt}_3$  and CdSe nanoparticles should be separated by the distance of  $\sim 2$  nm. This disagrees with the TEM image (Figure 6.6). The distances between  $\text{CoPt}_3$  nanoparticles in the bimodal array are  $\sim 3$  nm, while in the monolayer consisting only of  $\text{CoPt}_3$  nanoparticles, the nanoparticles are separated by  $\sim 2.5$  nm. Graphical sketch 6.1 schematically demonstrates the possible arrangements of nanoparticles: (a) CdSe nanoparticles are in the first layer; (b)  $\text{CoPt}_3$  nanoparticles are in the first layer; (c) CdSe nanoparticles occupy the positions in the first and in the third layers; (d) CdSe and  $\text{CoPt}_3$  nanoparticles are mixed in the layers. Analysis of the TEM images allows us to assume that CdSe and  $\text{CoPt}_3$  nanoparticles

are located in different layers. Arrangement of nanoparticles depicted at the graphical sketch 6.1c agrees well with the TEM images. At the TEM images CdSe nanoparticles have much lower contrast as compared with CoPt<sub>3</sub> nanoparticles that makes difficult more precise analysis of the TEM data.



**Graphical sketch 6.1.** *The schematic arrangement of nanoparticles in the first and in the second layers. Large dark grey and small grey circles represent CoPt<sub>3</sub> and CdSe nanoparticles, respectively. Organic shell of nanoparticles is depicted by bright grey colour.*

The shape of individual nanocrystals can strongly affect the morphology of self-assembled structures. An example of shape-driven self-assembly of magnetic nanocrystals are long ribbons of the hcp-Co nanodisks stacked face-to-face and lying on the edge [22]. In the case of spherical particles the crystalline lattices of individual nanocrystals are randomly oriented within a superstructure, as a rule.

Moreover, in the case of spherical particles the crystalline lattices of individual nanocrystals are randomly oriented within a superstructure. However, faceted and, in particular, cubic nanocrystals can form “lattice matched superstructures” where each nanocrystal has the same orientation as its neighbors (Figure 6.7). Such superstructures are of intriguing interest for materials with high magnetic anisotropy constant because of the possibility to align the easy magnetization axes of individual nanocrystals. The magnetic anisotropy of CoPt<sub>3</sub> nanocrystals makes them, probably, superior candidates for realising this new kind of artificial solids.

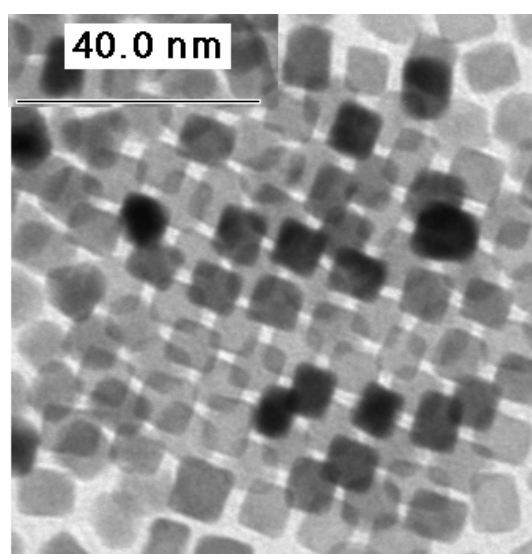


**Figure 6.7.** *TEM images of self-assembled structures of cubic CoPt<sub>3</sub> nanocrystals.*

### 6.3. Template self-assembly of CoPt<sub>3</sub> nanocrystals\*

The ability to manipulate with nanocrystals and assemble them into robust intergrated structures will be essential for future technological applications [1]. Controlled self-assembly of magnetic nanocrystals is of great interest due to potential application of such system as nanodevices. Devices that exploit the novel electronic properties of nanocrystals will require fabrication of nanocrystal assemblies with precise spatial control [1]. Many efforts including Langmuir-Blodgett (LB) technique [23] (where monolayers are formed on a water surface and then transferred onto a solid support) and layer-by-layer (LBL) technique have been applied to fabricate ordered structures of nanocrystals with controllable thickness and dimensions. The major advantages of LBL adsorption from solution are that many different materials can be incorporated in individual multilayer films and that the film architectures are completely determined by the deposition sequence [24]. LBL technique was successfully used to fabricate 2D and 3D ordered structures of semiconductor, metal and oxide nanoparticles. Thus poly(ethylenimine)-functionalized FePt nanocrystals were packed into uniform film using the layer-by-layer deposition technique [25]. Polymer mediated self-assembly of magnetic PtFe nanocrystals allowed to control assembly thickness and dimensions [25]. Also the LBL method was used to form closely packed films of Fe<sub>3</sub>O<sub>4</sub> nanoparticles [26]. However, controllable formation of one-dimensional arrays of nanocrystals is more difficult to be achieved [27]. Only in a few reports the realisation of 1D arrangement of nanocrystals was shown. Thus Schmid et al. demonstrated arrangement of gold nanocrystals into 1D by the modified LB technique [27]: single gold cluster rows were formed at the boundary between water and dichloromethane in the case of very diluted solution of gold clusters and polymer. When polymer supports the formation of monolayer of smaller dimensions the better result with respect to 1D structures was observed [27]. Spreading of the amyl acetate solution of some polymers (nitrocellulose, octyl-sulphoxy poly(p-phenylenevinylene (PPV) and etc.) on the surface of cold water (~3 – 5 °C) leads to the self-organized formation of a low-dimensional network structure over extended area [28,29]. This peculiarity of the nitrocellulose film on water surface has been used in the investigation of template self-assembly of CoPt<sub>3</sub> nanocrystals.

---

\* This work was done in collaboration with Dr. L.Govor (University of Oldenbugr, Germany).

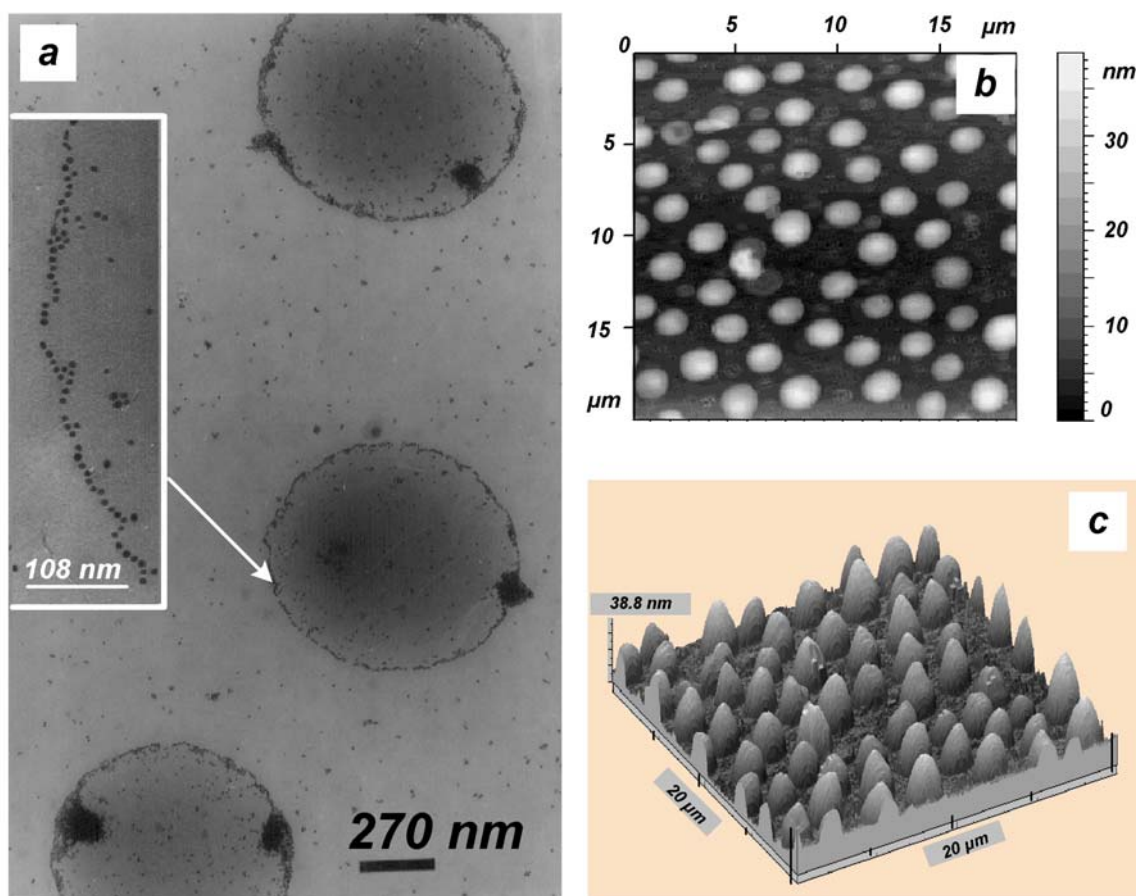


**Figure 6.8.** TEM overview of the composite nitrocellulose –  $\text{CoPt}_3$  nanocrystals film (a), closer look onto the arrangement of nanocrystals in the ring (a, inset); two-dimensional (b) and three-dimensional AFM images of the nitrocellulose –  $\text{CoPt}_3$  nanocrystals film.

Self-organised composite (nitrocellulose - magnetic nanocrystals) network structures were fabricated in two steps: (i) a hexane solution of 6.3 nm  $\text{CoPt}_3$  nanocrystals stabilised by HDA (24 mg/mL) and 1 wt.% nitrocellulose amyl acetate solution were mixed with the 1:2 volume ratio; (ii)  $\sim 3 \mu\text{L}$  of this solution were dropped onto a clean water surface forming  $\sim 520 \text{ nm}$  thick film over  $\sim 86 \text{ mm}$  in diameter. Elemental analysis of 6.3 nm  $\text{CoPt}_3$  nanocrystals showed that  $\sim 30 \text{ wt.}\%$  of the total weight of the sample is HDA. It means that the concentration of HDA is  $\sim 0.7 \text{ mg/mL}$ . The carrier solvents (hexane and amyl acetate) evaporated during  $\sim 5$  seconds and thin polymer film was transferred from the water surface onto the appropriate substrate. TEM was performed to investigate the distribution of nanocrystals into the polymer film. Figure 6.8a shows the overview TEM image of typical nitrocellulose –  $\text{CoPt}_3$  nanocrystals composite film. Nearly uniform rings of preferably 1D-ordered nanocrystals are clearly seen (Figure 6.8a, inset). The diameters of these rings are  $\sim 800 - 1500 \text{ nm}$ . Some  $\text{CoPt}_3$  nanocrystals are randomly distributed inside and outside of these

rings. Each ring also contains one or two small spots of 2D ordered nanocrystals. Topography of the composite film was analysed by atomic force microscopy (AFM) in the contact mode regime (Figure 6.8b and 6.8c). AFM analysis revealed droplets with a quasi periodic structure at the surface of film. It was found that these droplets consisted from HDA. HDA can be easily removed from the surface of the composite film by washing the film with hexane. CoPt<sub>3</sub> nanocrystals are strongly fixed in the polymer matrix and removing of the HDA does not lead to the degradation of 1D arrangement of nanocrystals. Such structures can be of interest of the investigation of the electron transport mechanism in 1D chains of metal nanocrystals.

### 6.4. Colloidal crystals of nanocrystals

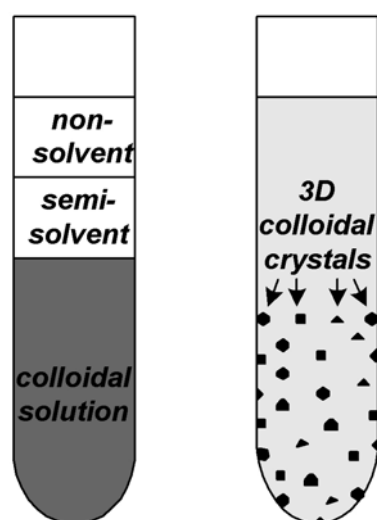
Crystallisation of monodisperse nanocrystals into macroscopic solids (colloidal crystals) is the next step in preparation of ordered superstructures. In such colloidal structures monodisperse nanocrystals can be considered as artificial atoms in the next level of hierarchy. Monodisperse CoPt<sub>3</sub> nanocrystals have a strong tendency to form 3D superlattices, as evidenced from Figure 6.4. The main points of superlattice formation are:

- (i) When a colloidal solution becomes unstable the particles aggregate and precipitate from the solution.
- (ii) The structure of the precipitated aggregates depends on the rate of destabilisation of colloidal solution.
- (iii) Slow destabilisation of colloidal solution results in the homogeneous nucleation of ordered nanoparticle aggregates in the colloidal solution.
- (iv) Slow destabilisation provides sufficient time for colloidal particles to find equilibrium superlattice sites.

The destabilisation of colloidal solution can be achieved by evaporation of the solvent, addition of a non-solvent, high-speed centrifugation, cooling a colloidal solution, *etc.* We found an easy way leading to the formation of 3D ordered “superlattices”. Crystallisation of nanoparticles into 3D “superlattices” can be induced by slow diffusion of a non-solvent (methanol) into a solution of FePt or CoPt<sub>3</sub> nanocrystals dissolved in toluene through a “semi-solvent” layer of propanol-1 (or propanol-2) (Scheme 6.1) which plays the role of buffer layer. The thickness of buffer layer regulates the rate of the destabilisation of nanocrystal solution. The presence of mediate layer of propanol-1 was necessary to form the regular-

shaped  $\sim 100 \mu\text{m}$  colloidal “supercrystals” of CdSe nanocrystals since methanol precipitated CdSe nanocrystals too fast and mainly irregular-shaped precipitates were formed [30]. However, destabilisation of colloidal solution of magnetic nanocrystals (where attractive dipole-dipole interactions are strong enough) results in the formation of colloidal crystals in a reasonable time window ( $\sim 1$ -2 weeks) even without addition of the methanol layer.

Slow destabilization of a colloidal dispersion of nanoparticles in toluene resulted in nucleation of colloidal crystals of nanocrystals, preferentially on the walls of a glass tube. Thicker black and thinner brownish coloured colloidal crystals visible by eye were formed in approx. 2 weeks. Thus applying the technique of controlled oversaturation [30], micrometer-size colloidal “supercrystals” consisting from monodisperse FePt [13] and  $\text{CoPt}_3$  [14] nanoparticles were grown.



**Scheme 6.1.** *Schematic outline illustrating the concept of the oversaturation technique used for the crystallization of monodisperse FePt and  $\text{CoPt}_3$  nanocrystals.*

Figure 6.9a,b shows optical micrographs of FePt colloidal crystals adhering to the glass. The crystals grew preferably in the form of faceted triangular or hexagonal platelets of  $\sim 10$ - $30 \mu\text{m}$  on the glass walls of the crystallisation tube (Scheme 6.1, *right image*). The colloidal crystals of PtFe nanocrystals with pyramide-like shape were also observed. Scanning electron microscopy (SEM) provides a closer look on the morphology of colloidal crystals. In the case of FePt, faceted triangular platelets, incomplete hexagonal platelets, and tetrahedral colloidal crystals with imperfect sides showing terraces and cleaved ledges were clearly distinguished (Figure 6.9c-e). Figure 6.10 presents SEM images of well-faceted hexagonal, triangular and pyramid-like colloidal crystals built from  $\text{CoPt}_3$  nanocrystals.

The arrangement of nanocrystals at the surface of colloidal crystals can be studied using TEM and HRSEM techniques (Figure 6.11). TEM images were taken from small fragments of

the FePt colloidal crystals obtained by mechanical grinding and treatment in an ultrasonic bath. Hexagonal arrangements of nanocrystals, i.e. the building blocks of the colloidal crystals, are clearly seen at the edges of the crystalline pieces and in HRSEM image (Figure 6.11).

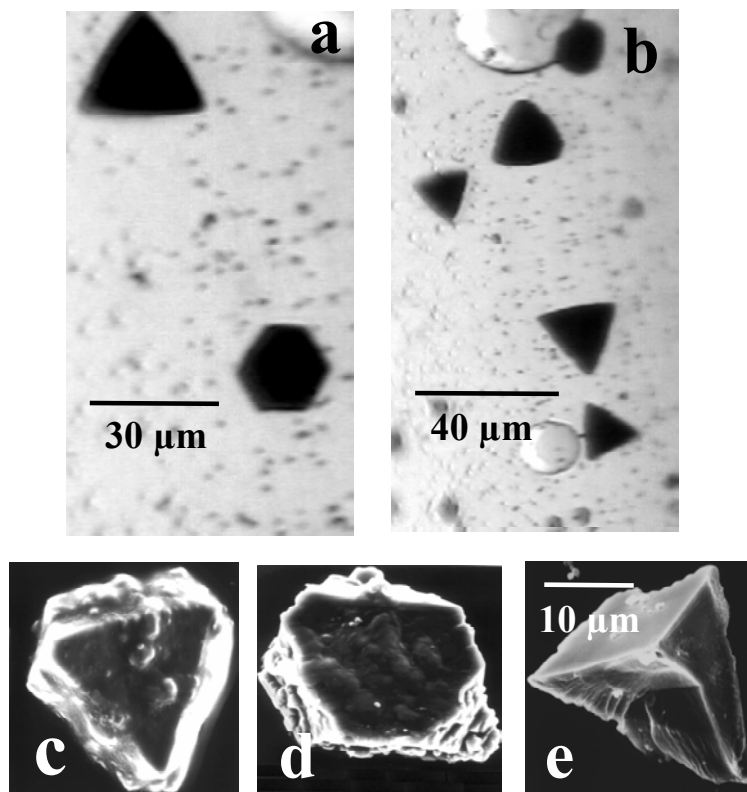


**Figure 6.9.** (a,b) Optical micrographs and (c,d,e) SEM images of colloidal crystals of 4.5 nm FePt nanocrystals illustrating their different shapes.

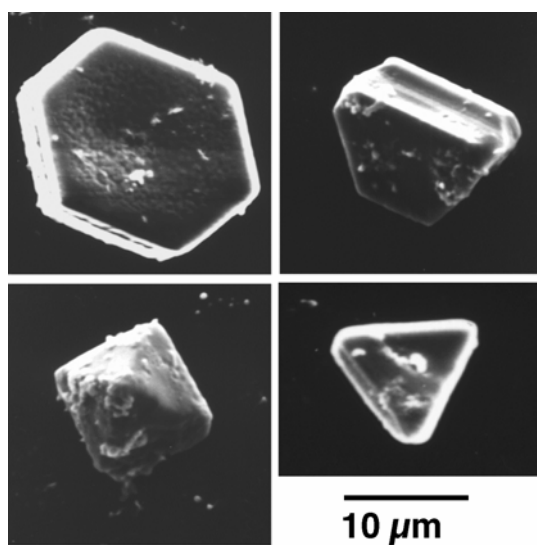


**Figure 6.10.** SEM images of colloidal crystals of 4.0 nm CoPt<sub>3</sub> nanoparticles.

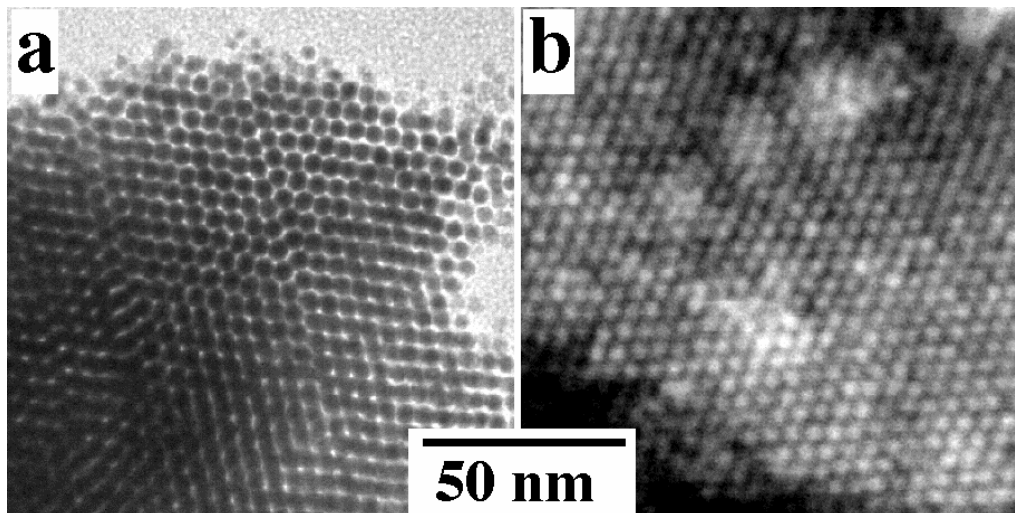


**Figure 6.11.** (a) TEM image of the fragment of a FePt colloidal crystal. (b) HRSEM image of the surface of a FePt colloidal crystal.

### 6.5. Magnetic properties of PtFe colloidal crystals\*

The study of the magnetic properties of FePt colloidal supercrystals has been performed using standard zero-field-cooling (ZFC) and field-cooling (FC) procedures and field-dependent magnetization measurements. The temperature dependent magnetization between 5 K and 350 K was measured in a field of 200 Oe. FePt nanoparticles exhibited superparamagnetic behaviour which was blocked for temperatures below 14 K as it is seen from the ZFC curve (Figure 6.12a). The magnetic anisotropy constant  $K$  was deduced from the blocking temperature  $T_B$  using the equation  $K=25k_bT_B/V$  [31] ( $k_b$  – the Boltzman constant,  $V$  – the volume of a single nanoparticle).  $K$  was calculated to be  $1.0 \times 10^6$  ergs/cm<sup>3</sup> assuming spherical 4.5 nm FePt particles. The FC curve rises monotonically with decreasing temperature below the ZFC cusp, as it was observed in systems containing randomly oriented magnetic nanoparticles [32,33]. In the field dependent magnetization measurements, a hysteretic behaviour and an increase of coercivity were observed below the blocking temperature with decreasing temperature, which is typical for the region of ferromagnetism (Figure 6.12b).

\* This work was done in collaboration with F. Wiekhorst and Prof. Dr. J. Kötzler (University of Hamburg, Germany).

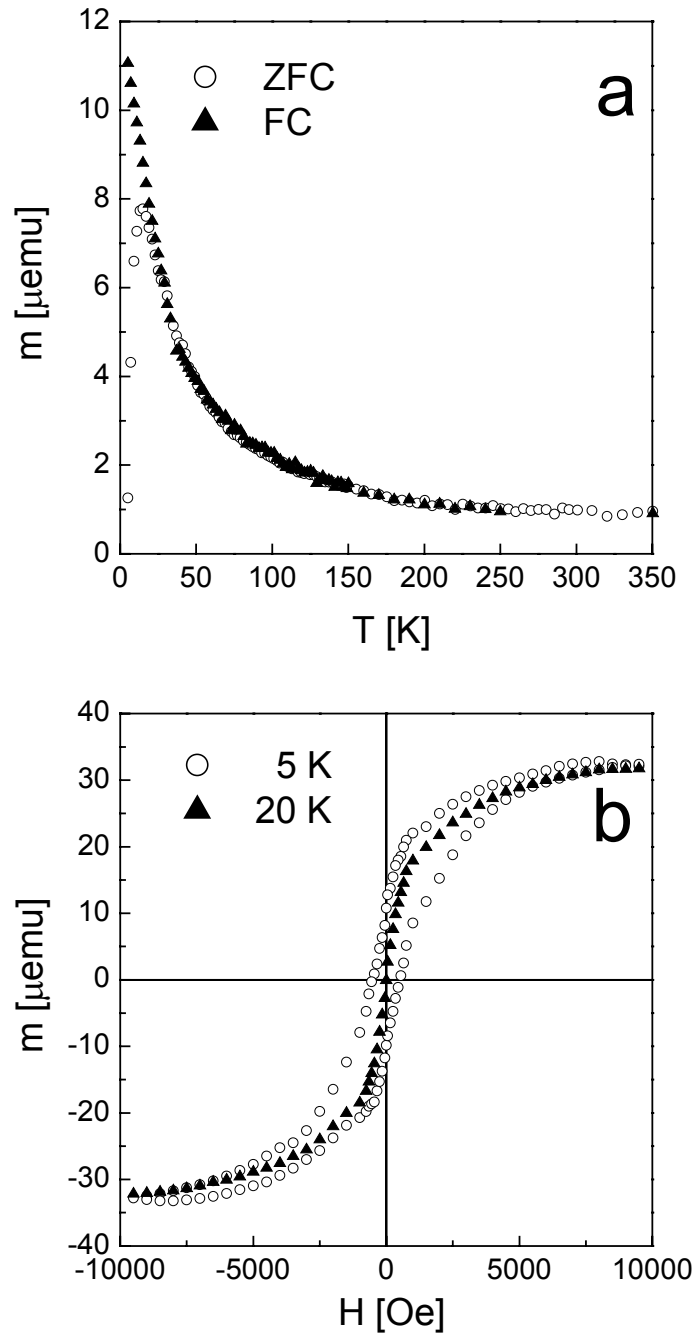


**Figure 6.12.** (a) Zero-field-cooled (circles) and field-cooled (triangles) temperature dependencies of the magnetization in a field of 200 Oe measured on FePt colloidal crystals. The maximum of the ZFC curve at 14 K marks the transition from superparamagnetic to ferromagnetic behaviour. (b) Magnetization-vs-field measurements on FePt colloidal crystals at different temperatures: 5 K (circles), 20 K (triangles).

## **6.6. Self-assembly of magnetic nanocrystals in external magnetic field**

The self-assembly of colloidal magnetic nanocrystals can also be affected by applying an external magnetic field. The influence of the magnetic field on the self-assembly of magnetic nanocrystals are of a great fundamental and practical interest [11,34,36]. Deposition in a magnetic field introduces anisotropy in the assembly of magnetic nanocrystals and thus in magnetic properties of their films [11]. The strength and the direction of the applied external magnetic field strongly influences the morphology of self-assembled structures of magnetic nanocrystals [34-36]. The influence of the magnetic field was observed in the case of nanometer structures as well as at the microscopic level. Thus, spindle-shaped deposits from multi-twinned-fcc Co nanocrystals with their long axes aligned along the external magnetic field [11] and 2D ordered nanostructures [35] were formed when a magnetic field was applied in the plane of the substrate during the deposition of the cobalt dispersion. Wen et al. [37] demonstrated the evolution of planar magnetic lattices using glass micro spheres coated with nickel in an external magnetic field. A stable hexagonal lattice was formed when a perpendicular magnetic field was applied. Tilting the magnetic field at an angle of  $60^\circ$  transformed the hexagonal lattice into straight chains aligned along the field direction under. Also, Pileni et al. observed a large extent of corrugation of cobalt nanocrystals with quasi-periodic structure along the field. The ordering and the compacity of the corrugated film markedly increased with the strength of the applied field [36]. When the magnetic field was applied perpendicular to the substrate a well-defined hexagonal network of dots consisting of cobalt nanoparticles was observed [36].

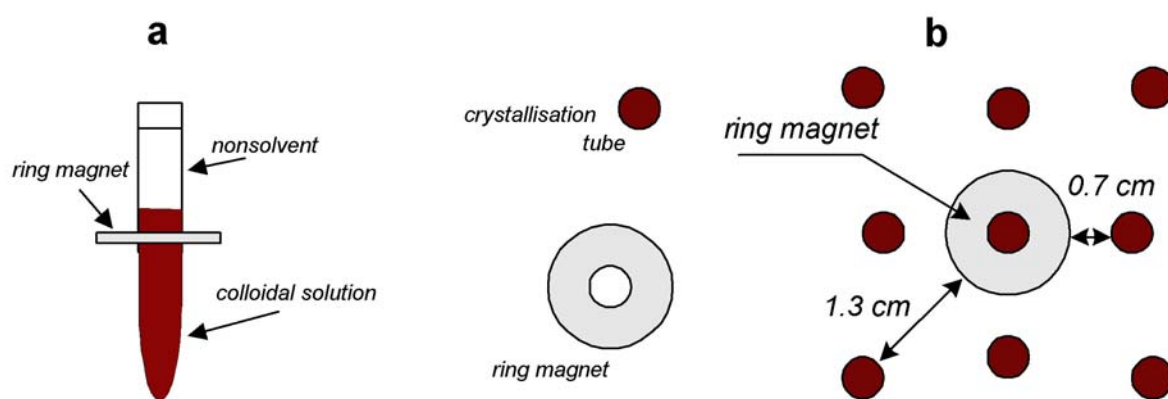
However, the lack of the systematic investigations and some contradictions of the published results can be noticed. A lot of studies on the influence of the magnetic field on the nanocrystal arrangement was performed with water soluble iron oxide nanocrystals having rather broad size distribution. Since the magnetic properties depend on the nanocrystal size, the nanocrystals in a polydisperse sample “feel” the applied magnetic field differently. In its turn, the different susceptibility of magnetic nanocrystals to the magnetic field can considerably influence on the arrangement and ordering of nanocrystal assemblies in external magnetic fields.

We investigated the influence of the magnetic field on the crystallisation of monodisperse different-sized  $\text{CoPt}_3$  nanocrystals into 3D colloidal “supercrystals”. As the method of controlled oversaturation allows us to prepare the superlattices coherent over tens of micrometers (Figure 6.9; 6.10), we investigated the destabilisation of a colloidal solution of

the magnetic nanocrystals in parallel or perpendicular magnetic fields of different strengths. Monodisperse samples of  $\text{CoPt}_3$  nanocrystals of different size were synthesised via the ACA approach in HDA – diphenyl ether coordinating mixture (see *Chapter 2* and *Chapter 3*) and re-dissolved in toluene. Crystallisation of  $\text{CoPt}_3$  nanocrystals has been carried out in vertically positioned glass tubes (see *Chapter 6.4*). Neodymium-iron-boron permanent magnets of different shapes and sizes were used as sources of the magnetic field. Precipitation of colloidal nanoparticles in the presence of magnetic field occurs much faster than in the absence of an external field. Precipitation of nanocrystals in an external magnetic field was observed in  $\sim 1$ -3 days. Complete crystallisation of nanocrystals usually requires approx. one week.

Crystallisation of nanocrystals under the influence of a magnetic field has at least two driving forces: slow destabilisation of colloidal solution as a result of diffusion of the non-solvent into the colloidal solution and the interaction of nanocrystals with the external magnetic field. Depending on the precipitation conditions (non-solvent, strength of the magnetic field, direction of the magnetic field, *etc.*) several types of self-assembled structures composed of  $\text{CoPt}_3$  nanocrystals were observed.

*Crystallisation of  $\text{CoPt}_3$  nanocrystals in magnetic fields applied parallel to the substrate.* Toluene solution of  $\sim 9$  nm  $\text{CoPt}_3$  nanocrystals was destabilised by *i*-PrOH. The central crystallisation tube was placed inside the ring magnet (25 $\times$ 10 $\times$ 3, mm) (Scheme 6.2a). The ring magnet was fixed below the interface “colloidal solution – non-solvent” as depicted in Scheme 6.2a. The direction of the magnetic field ( $\sim 0.89$  T) was *parallel* to the walls of the crystallisation tubes (substrate). The strength of the magnetic field was varied by changing the distance from the magnet to the tubes (Scheme 6.2b) in order to test the influence of its strength of the magnetic field on the assembly of nanocrystals.

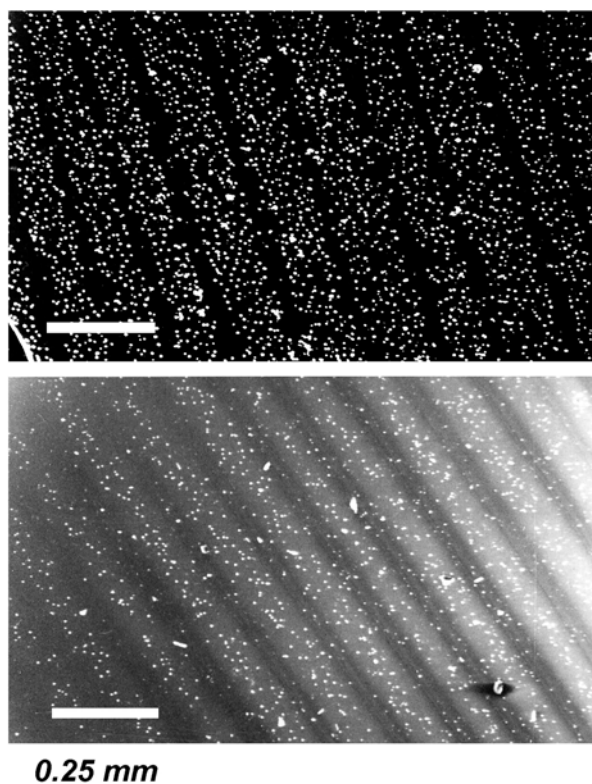


**Scheme 6.2.** (a) Sketch of central crystallisation tube (side view); (b) arrangement of glass tubes containing colloidal solution of  $\text{CoPt}_3$  nanocrystals (top view).

Crystallisation of magnetic nanocrystals in external parallel magnetic field did not result in the formation of colloidal “supercrystals”. Precipitated  $\text{CoPt}_3$  nanocrystals formed relatively thick films at the glass walls of the crystallisation tube. SEM investigation of these films revealed their periodic structure. Figure 6.13 demonstrates micrometer-sized periodic stripes of  $\text{CoPt}_3$  nanocrystals. Further SEM investigation and data of the elemental analysis (EDX) showed that the film consisted of regions with different concentration of precipitated nanocrystals - concentration stripes. The regions of high-concentration of  $\text{CoPt}_3$  nanoparticles are sharply separated from low-concentration regions.

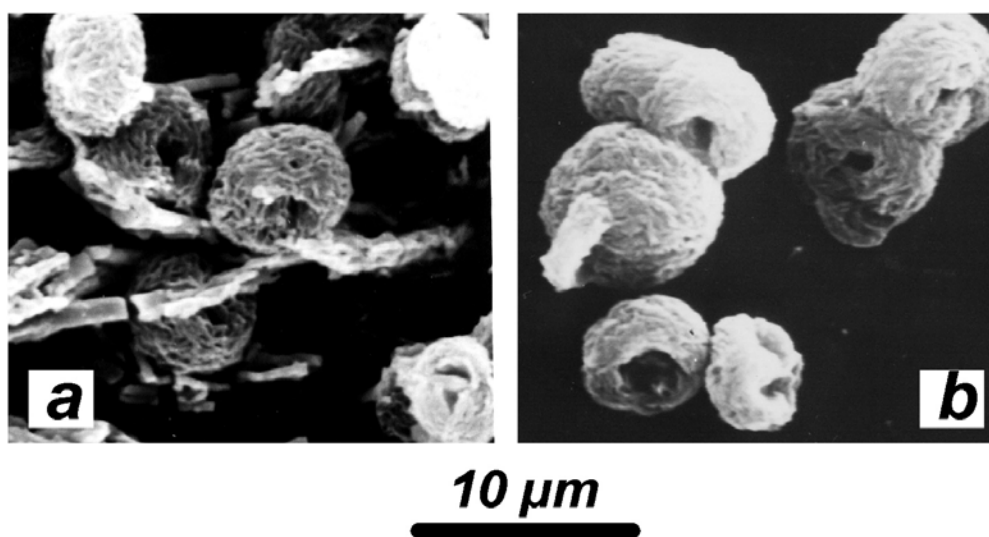
High-concentration regions as well as low-concentration regions have a granular structure. Within the stripes,  $\text{CoPt}_3$  nanocrystals organised themselves into rather uniform  $\sim 5$   $\mu\text{m}$  microballs (Figure 6.14; 6.15). In the area exposed to the highest magnetic field, it was also possible to find some amount of elongated microaggregates together with microballs (Figure 6.14a). The stripes formed in weaker magnetic field (for examples in the case of tubes arranged at  $\sim 1.3$  cm from the magnet or in the bottom part of other tubes) consisted of smaller  $1.5$   $\mu\text{m}$  microballs (Figure 6.15). The formation of these spherical aggregates in external magnetic fields is surprising and unexpected because of the strong orientation influence of the magnetic field.

The widths of high-concentration ( $L_{\text{HC}}$ ) and low concentration regions ( $L_{\text{LC}}$ ) depend strongly on distance between the magnet and crystallisation tube. A clear tendency of decreasing  $L_{\text{HC}}$  and increasing  $L_{\text{LC}}$  with increasing distance between the magnet and tube were observed (Table 6.1). However, the period  $L = L_{\text{HC}} + L_{\text{LC}}$  is nearly the constant in all three cases.



---

**Figure 6.13.** Concentration stripes of  $\sim 9.0$  nm  $\text{CoPt}_3$  nanocrystals formed in the tubes arranged at the distance of 0.7 and 1.3 cm from the ring magnet, respectively.



---

**Figure 6.14.** “Large” spherical aggregates of  $\sim 9$  nm  $\text{CoPt}_3$  nanoparticles

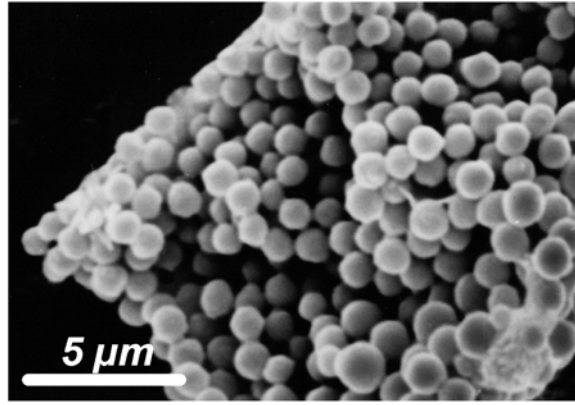


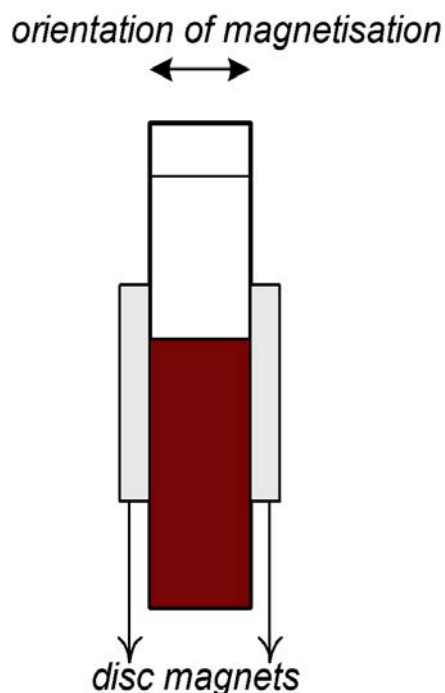
**Figure 6.15.** *The fragment of high –concentration stripe consisting of “small” spherical aggregates of CoPt<sub>3</sub> nanocrystals self-assembled in an external magnetic field.*

Similar results were also observed in a corresponding set of experiments with CoPt<sub>3</sub> particles of 6.3 nm.

The formation of periodic structures of magnetic nanoparticles in parallel magnetic field was previously reported [38,39]. Thus Wirtz et al. [38] reported that the formation of macroscopic one-dimensional periodic pattern composed of high-concentration regions of magnetic particles. The formation of these periodic patterns was achieved only in an oscillating magnetic field. In contrast, Wang et al. succeeded the formation of very similar periodic branched structures under constant magnetic field [39]. Unfortunately, the internal structure of their concentration stripes is unknown. Understanding of the mechanism governing the self-assembly of magnetic nanoparticles into spherical aggregates in external parallel magnetic field requires further careful investigation

**Table 6.1.** *Characterisation of the stripes of CoPt<sub>3</sub> nanocrystals obtained under magnetic field.*

Position of tubes relatively to the ring magnet	$L_{HC}$ , $\mu\text{m}$	$L$ , $\mu\text{m}$	Remarks
Inside	137	145	The stripes are arranged very close to each other
0.7 cm	121	146	The distance between the stripes becomes larger
1.3 cm	84.3	140	



**Scheme 6.3.** Crystallisation of magnetic nanocrystals in quartz cuvette in perpendicular magnetic field.

*Crystallisation of  $\text{CoPt}_3$  nanocrystals in magnetic fields applied perpendicular to the substrate.* When the crystallisation process occurred in the cuvette arranged between two strong magnets ( $\sim 0.68$  T) (Scheme 6.3) magnetic field was perpendicular oriented to the substrate (walls of cuvette). The crystallisation of  $\sim 4$  nm  $\text{CoPt}_3$  nanoparticles continued  $\sim$ one week. After that the supernatant solution was removed and two walls of the cuvette were investigated by SEM. (Figure 6.16). SEM investigation revealed the formation microneedles at the walls of cuvette.

These microneedles are strongly fixed at the quartz substrate. They have no tendency to crack under evaporation of supernatant solution. Improved mechanical stability of our needles allows to isolate them from the substrate without destroying.

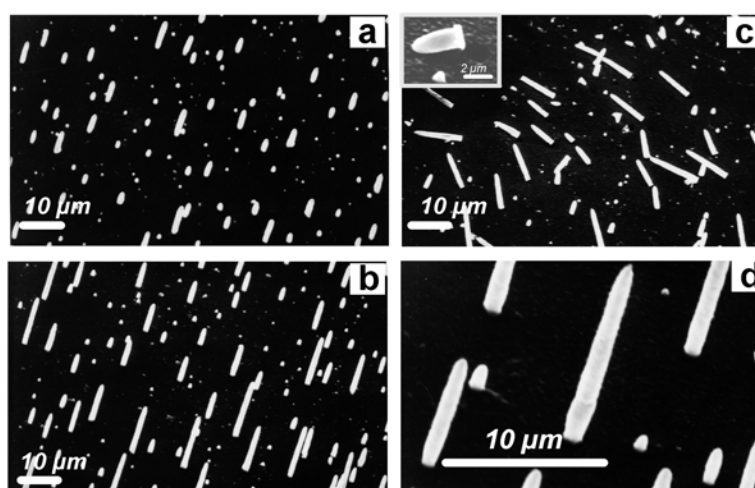


**Figure 6.16.** (a) Needles composed of 4.0 nm  $\text{CoPt}_3$  nanocrystals deposited in the magnetic field applied perpendicular to the walls of crystallisation cuvette; (b, d) – the images were acquired after tilting of the substrate by  $40^\circ$ ; (c) microneedles isolated from the substrates.

Further SEM investigation allows us to assume perpendicular orientation of needles to the walls of cuvette. SEM image (Figure 6.17) acquired at  $0^\circ$  tilt of the substrate represents the top projection of the microneedles. As expected perpendicular orientated microneedles look like spheres as compared with isolated microneedles. This means that  $\text{CoPt}_3$  nanocrystals organise themselves into microneedles aligned along the magnetic field. This result is in agreement with the observation of Pileni [37] who demonstrated the formation of column along the magnetic field during the drying of the colloidal solution of cobalt nanoparticles under magnetic fields.

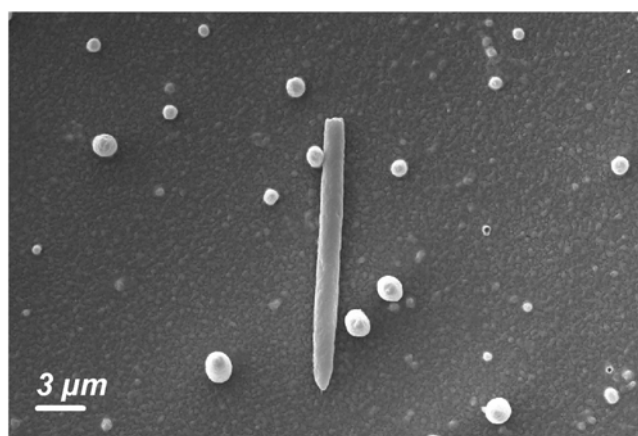


**Figure 6.17.** Image of the needles consisted of 4.0 nm  $\text{CoPt}_3$  nanocrystals measured at  $0^\circ$  tilt of the substrate demonstrates the perpendicular grows of microneedles with respect to cuvette wall (view from top).

The needles have different lengths:  $\sim 2 - 25 \mu\text{m}$  (mean length is  $\sim 7 - 10 \mu\text{m}$ ) and width ( $1-2 \mu\text{m}$ ) (Figure 6.16c). Analysis of the individual needles by HRSEM revealed the only locally ordered arrays of  $\text{CoPt}_3$  nanocrystals. In addition to the needles, the hollow tubes were also found (Figure 6.18, *left* and *inset*) in the samples.

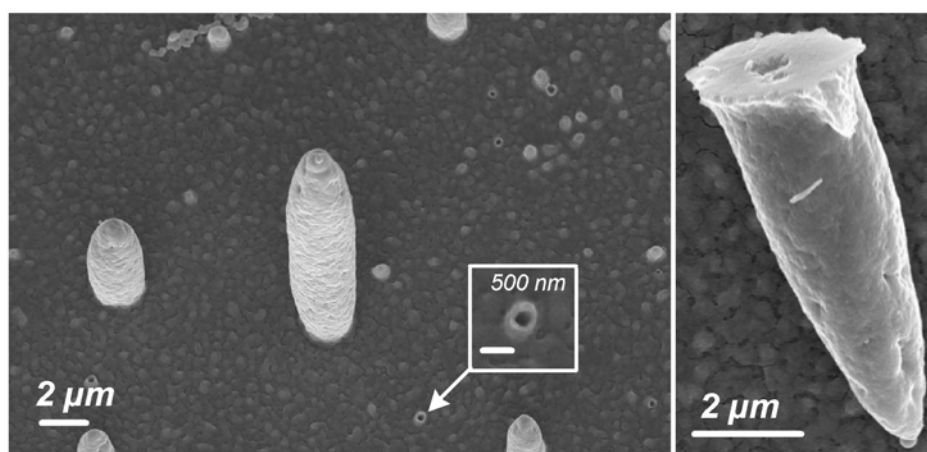


**Figure 6.18.** Needles consisted of 4.0 nm  $\text{CoPt}_3$  nanocrystals deposited in the magnetic field applied perpendicular to the walls of crystallisation cuvette the images were acquired at  $20^\circ$  tilt of the substrate.

These hollow tubes are  $\sim 100 - 200$  nm long and have the diameter  $\sim 400 - 500$  nm. The values of the hole diameters inside the tube lie between  $\sim 300 - 350$  nm. Tilting investigation of the isolated microneedle also shown the presence of empty cavities with the diameters  $\sim 400$  nm at their base (Figure 5.21, *right*). Probably, similar values of diameters of holes in hollow tubes and cavities in the base of the needles can indicate that the hollow tubes are the previous stage of growing microneedles.

Similar results were also observed in the sets of experiments with  $\text{CoPt}_3$  particles of other sizes or in the experiments where the strength of the magnetic field was varied. Thus destabilisation of colloidal solution of 7.5 nm  $\text{CoPt}_3$  nanoparticles by applying external perpendicular magnetic field ( $\sim 0.9$  T) also lead to the formation of microneedles. HRSEM analysis of microneedle did not reveal long-range ordering of  $\text{CoPt}_3$  nanocrystals at the surface (Figure 5.19, *top inset*). In order to investigate internal structure of the needle, a fragment of microneedle was investigated by TEM. TEM investigation also revealed only locally ordered nanocrystals (Figure 5.19, *low insert*). Therefore, we can attribute the needles to glassy solids where each nanocrystal remains separated from the neighbours by the shell of organic ligands.

Isolated from the substrate microneedles can be easily magnetised by applying the magnetic field. Figure 6.20 demonstrates the arrangement of  $\text{CoPt}_3$  microneedles taken from the cuvette and re-dispersed in *i*-PrOH dried in zero magnetic field and under magnetic field of  $\sim 0.89$  T. In the case of microneedles dried in zero magnetic field no preferential orientation of needles was observed (Figure 6.20b). However microneedles dried under magnetic field aligned along the magnetic field (Figure 6.20b). Pileni et al. reported that magnetic moments of the nanocrystals are oriented and ferromagnetic domains appear in the film during the deposition process in a magnetic field the. Their size increases with the strength of the applied magnetic field and the domains remain stable when the magnetic field is turned off. The stability of the ferromagnetic domain is controlled by the dipolar interactions between adjacent particles in the 3D structure. Increase of the strength of the magnetic field applied during the deposition process favours the formation of the ferromagnetic domains [36].

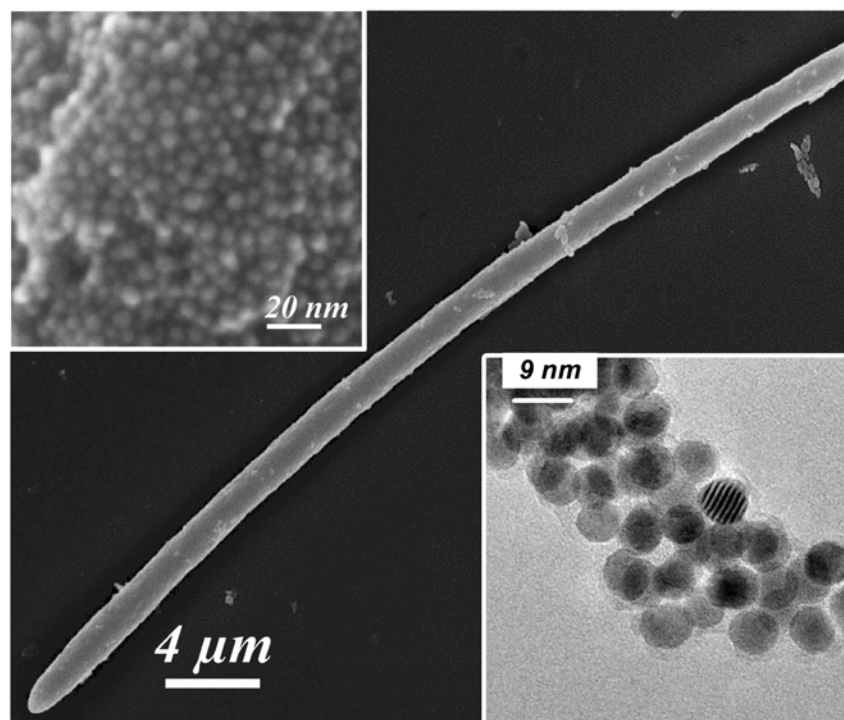


**Figure 6.19.** SEM overview image of a typical needle consisting of  $\sim 7.5$  nm  $\text{CoPt}_3$  nanocrystals. Upper inset demonstrates HRSEM image of the microneedle surface. Bottom inset shows HRTEM image of the microneedle fragment.

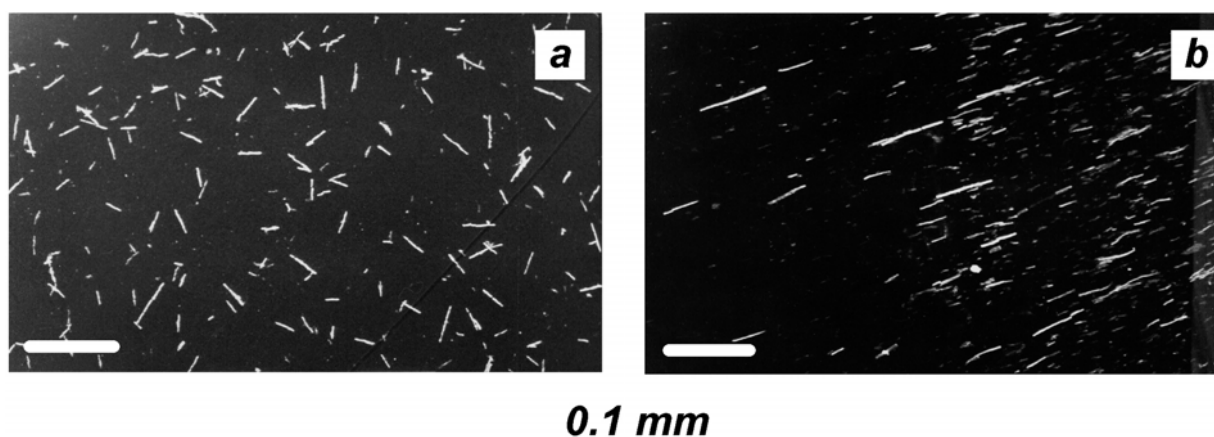
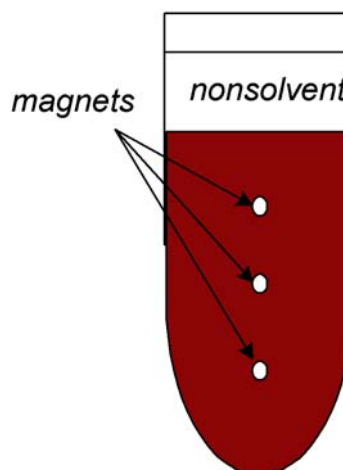


**Figure 6.20.** Arrangement of the microneedles consisting of  $\sim 7.5$  nm  $\text{CoPt}_3$  particles at room temperature in (a) zero field and in (b) external magnetic field ( $\sim 0.89$  T).

Relying on our experimental data we can conclude that nanocrystals in 3D structures formed under strong magnetic field (applied either parallel or perpendicular to the substrate) have only local ordering. Magnetic field induces fast destabilisation of colloidal solution of nanocrystals and as a result, glassy solids are formed while crystallisation of nanocrystals by controlled oversaturation of a colloidal solution in zero external magnetic field results in the

formation of perfectly faceted 3D supercrystals. How does the magnetic field strength influence the arrangement of magnetic nanocrystals? Is it possible to observe the crystallisation of magnetic nanocrystals into highly ordered 3D superstructures in a magnetic field? To answer these questions we performed the following set of experiments.

Small magnets were arranged at the glass walls of a crystallisation tube (Scheme 6.4) and the colloidal solution of 6.3 nm  $\text{CoPt}_3$  nanocrystals was destabilised by *i*-PrOH. The magnetic field ( $\sim 0.15$  T) strength gradually decreases with increasing the distance from the magnet. Thus the magnetic field strength is different at different spatial places of the crystallisation tube and hence the influence of the magnetic field on the crystallisation process can be probed in one crystallisation tube. The crystallisation process continued for  $\sim 3$ -6 days. After that the supernatant solution was removed from the glass tubes and the surface of crystallisation tube was analysed by the optical microscopy. Figure 6.21 represents the gallery of optical micrographs obtained at different distances from the magnet.



**Scheme 6.4.** Arrangement of the small circular disc magnets ( $\varnothing 1.5$  mm  $\times$  2 mm,  $H \sim 0.15$  T.) at the glass crystallisation tube. The magnetic field is perpendicular to the substrate (walls of the crystallisation tube). The distance between the magnets is  $\sim 1.5$  cm.

The most of particles precipitated in the area close to the magnets in the form of irregular-shaped plates (Figure 6.21). SEM analyse shows that these deposits consist mainly of a large number of microspheres closely attached to each other (Figure 6.22a). Investigation of these microspheres by HRSEM (Figure 6.23b,c) revealed only local nanocrystals ordering of microspheres of any size, so they can be considered as glassy solids. Moving away from the magnet the evolution of shape was observed. Nanocrystal aggregates with pronounced facets are formed with increasing distance from the magnet (Figure 6.21).

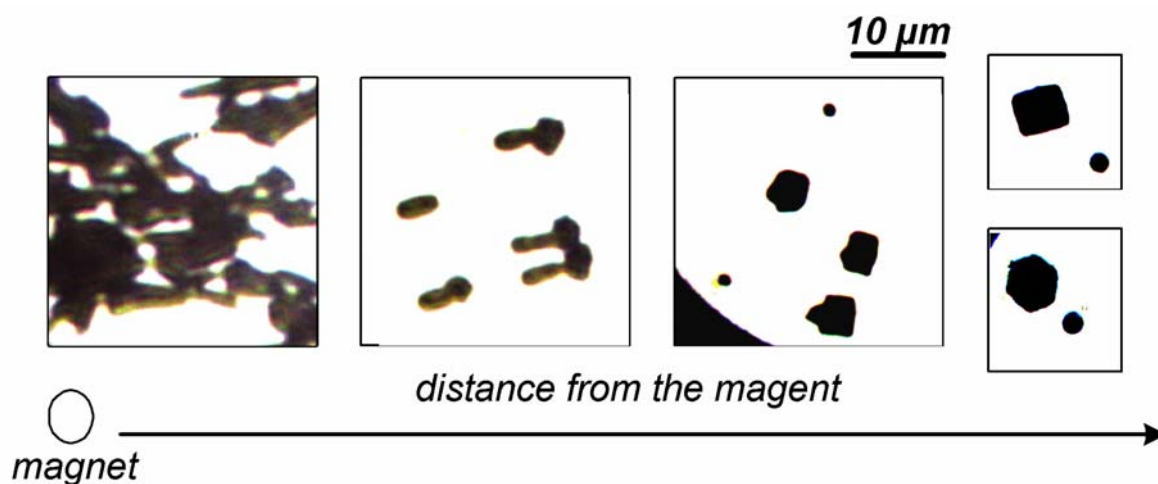


**Figure 6.21.** Optical micrographs demonstrating the shape evolution of nanocrystal assemblies.

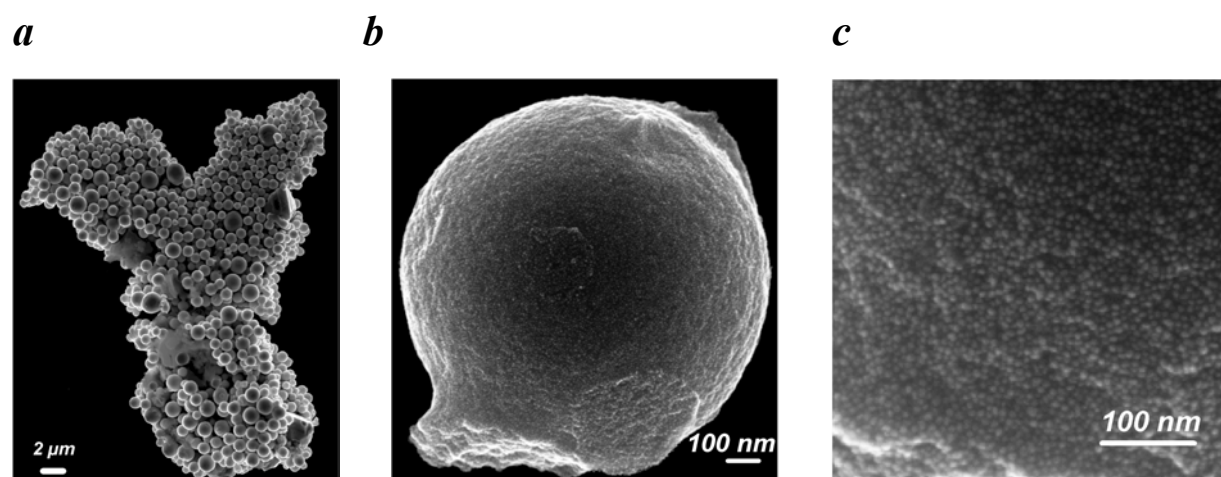


**Figure 6.22.** Spherical aggregates of 6.3 nm  $\text{CoPt}_3$  nanocrystals found in the area close to the magnet: (a) – overview SEM image and (b,c) HRSEM images

The most interesting cases of nanocrystal assemblies (elongated aggregates) are represented at the second and third photos of Figure 6.21. In one assembly it is conceivable to retrace the influence of the magnetic field on the ordering of nanocrystals. Elongated aggregates found by SEM consisted either of several microspheres or of elongated “tail” and a relatively faceted “head” part. Elongated “tail” of such nanocrystal aggregates always oriented to magnet. Figure 6.23a provides a closer look on such aggregate. Preliminary investigation by HRSEM revealed the transition from locally ordered  $\text{CoPt}_3$  nanocrystals in the tail part of the assemble to well ordered nanocrystals in faceted part.

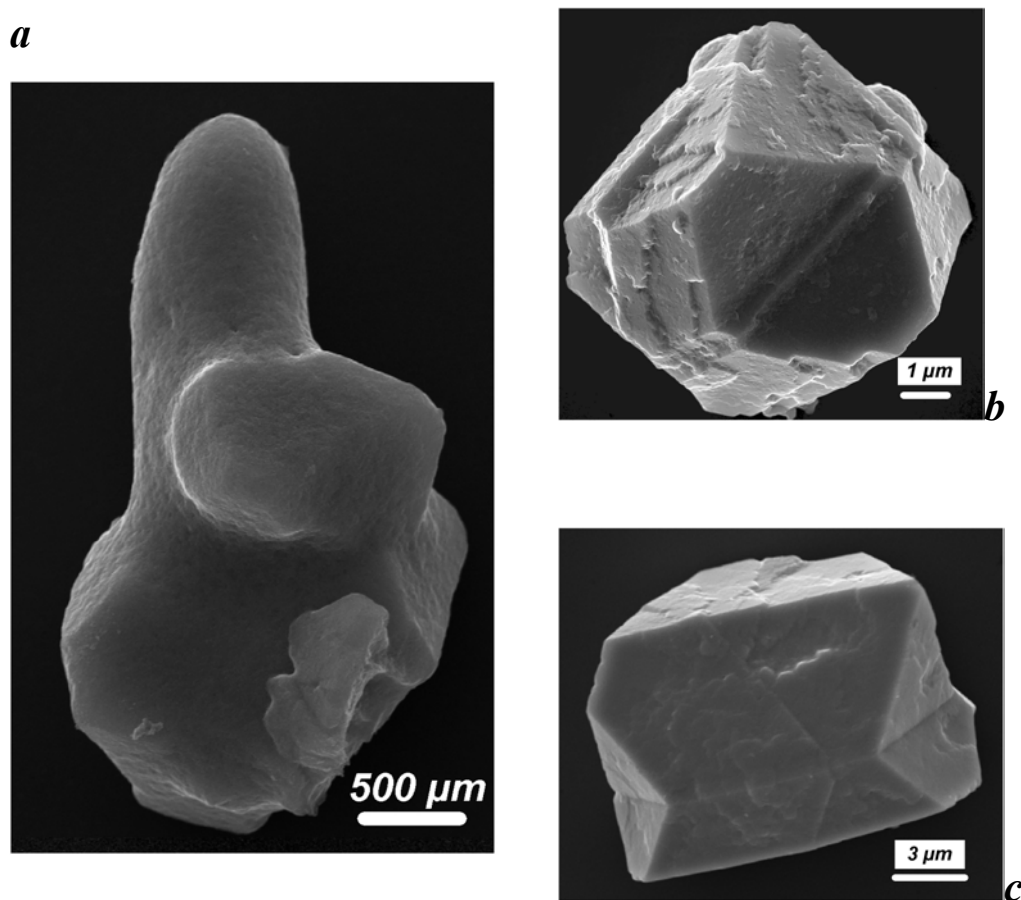
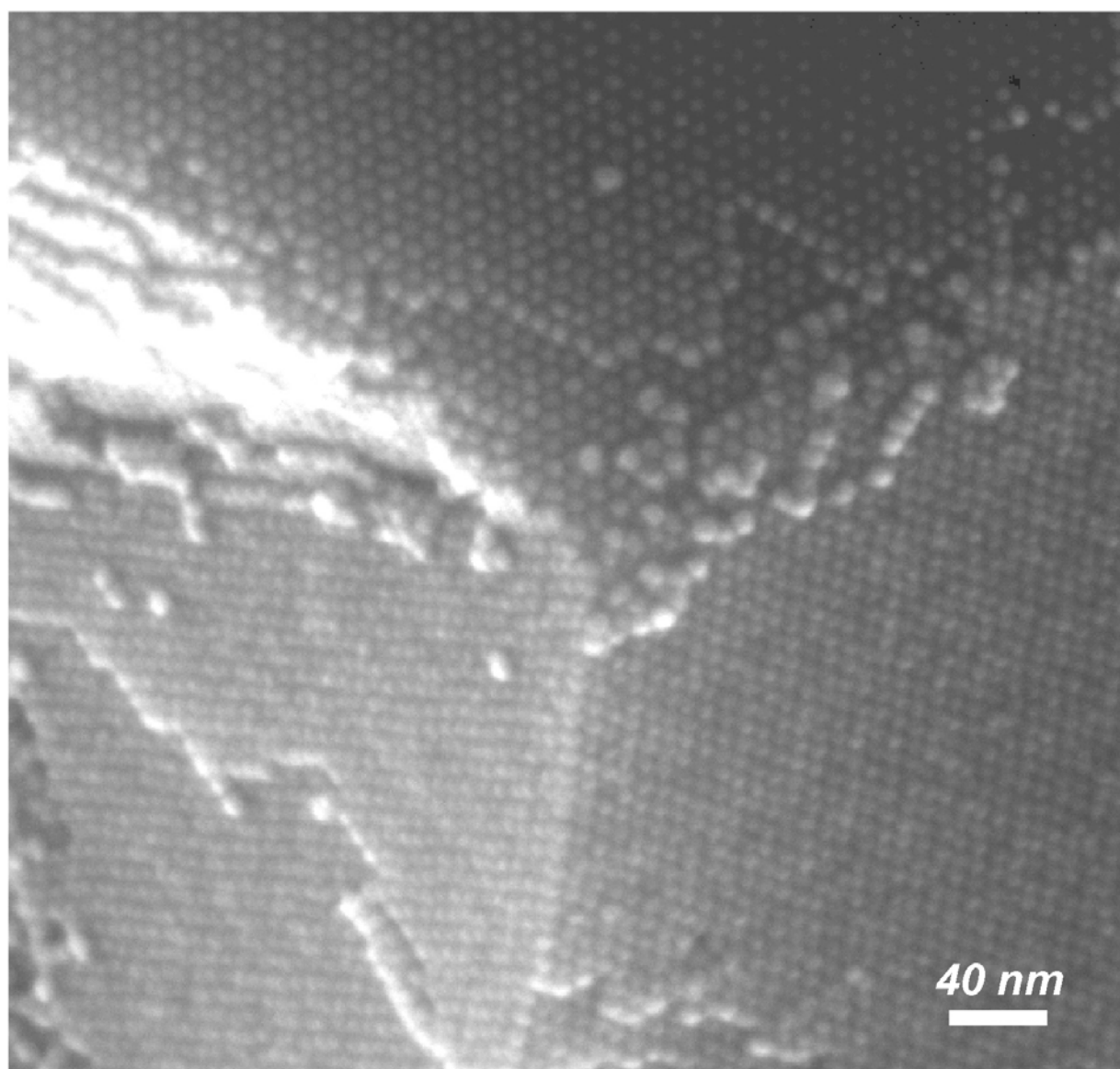


**Figure 6.23.** SEM images of elongated aggregates (a) and “supercrystals” (b, c) of 6.3 nm  $\text{CoPt}_3$  nanocrystals.

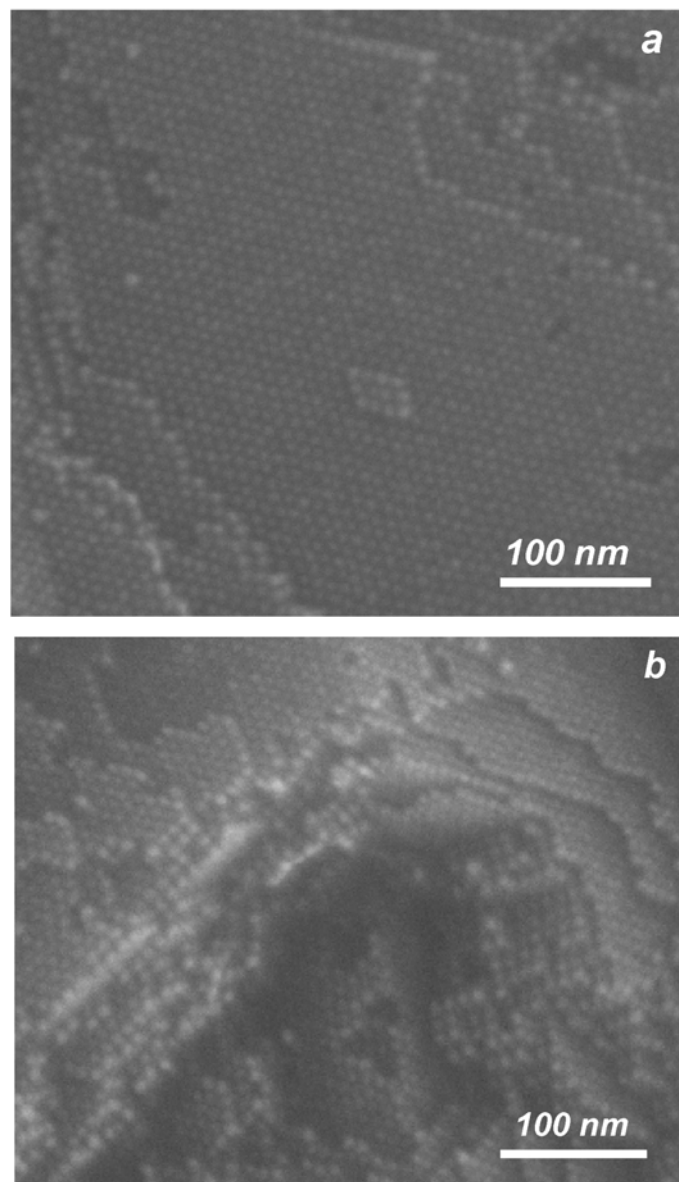
Faceted nanocrystals were found by optical microscope at the distance from the magnet where the strength of the magnetic field was  $\sim$  ten times lower ( $\sim 0.015\text{T}$ ) than that in the area close to the magnet. SEM investigation confirmed the faceting of these nanocrystal assemblies (Figure 6.23b,c). The surface of these assemblies was also examined by HRSEM. Figure 6.24 represents the facets of colloidal  $\text{CoPt}_3$  “supercrystal”. A perfect 3D ordered arrangement of  $\text{CoPt}_3$  nanocrystals coherent over the whole colloidal crystals was found (Figure 6.25). Analysis of HRSEM images allows to assume that 3D alignment of  $\text{CoPt}_3$  nanocrystals has the *fcc*-structure: images of different planes are consistent with those expected for (111), (100) and (110) projections of the *fcc* superlattice.

So, the magnetic fields can induce the crystallisation of magnetic nanocrystals into bulk structures different from those formed in the absence of the external magnetic fields. However, when strong magnetic field is applied to the crystallisation tube, too fast destabilisation of the colloidal solution resulting in the formation of preferably 3D glassy solids. Destabilisation of colloidal solution by only the magnetic fields leads to the precipitation of a part of magnetic nanoparticles in the form of film. However investigation of such films is complicated because of dissolution of films after removing the magnet from the crystallisation tube.



---

**Figure 6.24.** *HRSEM image demonstrating the facets of the CoPt<sub>3</sub> “supercrystals”*



---

**Figure 6.25.** HRSEM images demonstrating the ordering of 6.3 nm  $\text{CoPt}_3$  nanocrystals at the surface and inside the 'supercrystals'.

### 6.7. Inverse opals from PtFe nanocrystals

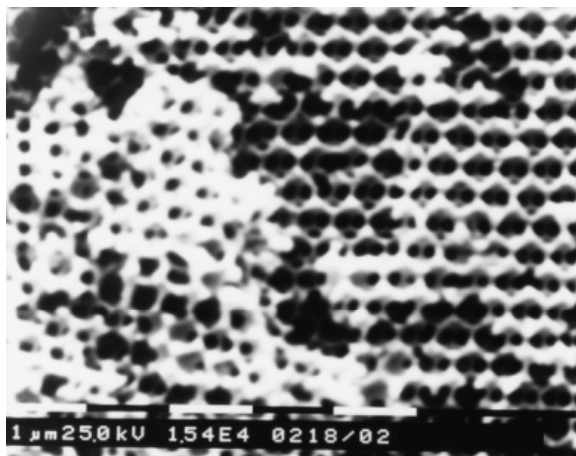


**Figure 6.26.** SEM image of an inverse colloidal crystal made from PtFe nanocrystals.

Chemical self-assembly (bottom-up) methods have been utilized for making 3D photonic crystals (so called artificial opals) from colloidal silica or polymer micrometer size spheres. Using artificial opals as templates, so called “inverse opals” possessing pronounced photonic bandgap can be prepared by impregnation of voids with different materials following by subsequent removal of the opal template by annealing or dissolution.

From the moment of the introduction of the photonic bandgap concept by Jablonovitch and John [41,42], materials possessing a three-dimensional periodicity of the dielectric constant have attracted increasing attention. The periodically varying index of refraction in photonic crystals causes a redistribution of the density of photonic states due to Bragg diffraction which is associated with stopbands for light propagation. It is expected that high ordered structures consisting from the materials with high refractive index difference (for example, metals and air) can possess the complete photonic bandgap [43]. This means that such a structure will selectively absorb the light with wavelength depending on the periodicity of its structure [44]. Additionally, magnetic nanocrystals can be used for fabrication of metal-dielectric inverse opals addressable through an external magnetic field [45]. Figure 6.26 shows a SEM image of an inverse FePt photonic crystal obtained by complete impregnation of a 3D template of monodisperse latex microspheres with FePt nanocrystals, following by dissolution of polymer spheres in toluene. 3D ordered opal structure consisting from ~503 nm monodisperse polystyrene spheres was infiltrated by an aqueous solution of 4.5 nm PtFe nanoparticles by several times. Nanoparticles strike into the opal structure forming their own ordered network. After that the sample was heated at ~90 °C and treated by toluene. Toluene slowly dissolves the polystyrene spheres. The ordered voids at the SEM image (Figure 6.26) indicates the full dissolution of polymer matrix and hence the formation of inverse opal is achieved.

## 6.8. Conclusions

Monodisperse magnetic alloy nanocrystals readily organise themselves in different 1D, 2D and 3D superstructures. Mixing differently sized nanocrystal sample with an appropriate ratio in size and packing fraction lead to the formation of mixed superlattices with high packing densities. Controllable destabilisation of colloidal solutions of magnetic nanocrystals resulted in the formation of colloidal “supercrystals” with the 3D ordered arrangement of nanocrystals coherent over tens micrometers. External magnetic field has the strong influence on the arrangement of magnetic nanocrystals into 2D or 3D superstructures and can be considered as the strongest driving force of the self-organisation process of magnetic nanocrystals under the experimental conditions described above. Amazing and novel superstructures of magnetic nanocrystals were prepared in external magnetic field. The formation of periodic concentration stripes of CoPt<sub>3</sub> nanocrystals was observed when the magnetic field was applied parallel to the substrate, whereas different types of needle-like assemblies were obtained when the field was applied perpendicular to the substrate. In relatively strong magnetic fields (~0.1 – 1 T) mainly glassy solids of magnetic nanocrystals are formed while in the weak magnetic fields (~0.01 – 0.02 T) also the formation of colloidal “supercrystals” can be observed.

## 6.9. References:

1. Murray, C.B.; Kagan, C.R.; Bawendi, M.G. *Annu. Rev. Mater. Sc.* **2000**, *30*, 545.
2. Collier, C.P.; Vossmeier, T.; Heath, J.R. *Ann. Rev. Phys. Chem.* **1998**, *49*, 371.
3. Rogach, A.L.; Talapin, D.V.; Shevchenko, E.V.; Kornowski, A.; Haase, M.; Weller, H. *Adv. Func. Mater.* **2002**, *12*, 653.
4. Puentes, V.F.; Krishnan, K.; Alivisatos, A.P. *Appl. Phys. Lett.* **2001**, *78*, 2187.
5. Kim, S.H.; Medeiros-Ribeiro, G.; Ohlberg, D.A.A.; Williams, R.S.; Heath, J.R. *J. Phys. Chem. B* **1999**, *103*, 10341.
6. Black, C.T.; Murray, C.B.; Sandstrom, R.L.; Sun, S. *Science* **2000**, *290*, 1131.
7. Markovich, G.; Collier, C.P.; Heath, J.R. *Phys. Rev. Lett.* **1998**, *80*, 3807.
8. Sun, S.; Murray, C.B. *J. Appl. Phys.* **1999**, *85*, 4325.
9. Puentes, V.F.; Krishnan, K.; Alivisatos, A.P. *Science* **2001**, *291*, 2115.
10. Tripp, S.L.; Pusztay, S.V.; Ribbe, A.E.; Wie, A. *J. Am. Chem. Soc.* **2002**, *124*, 7914.

11. Murray, C.B.; Sun, S.; Doyle, H.; Betley, T. *MRS Bulletin* 2001, 985-991.
12. Sun, S.; Murray, C.B.; Weller, D.; Folks, L.; Moser A. *Science* **2000**, 287, 1989.
13. Shevchenko, E.; Talapin, D.; Kornowski, A.; Wiekhorst, F.; Kötzer, J.; Haase, M.; Rogach, A.; Weller, H. *Adv. Mater.* **2002**, 14, 287.
14. Shevchenko, E.V.; Talapin, D.V.; Rogach, A.L.; Kornowski, A.; Haase, M.; Weller, H. *J. Am. Chem. Soc.* **2002**, 124, 11480.
15. Hachisu, S.; Youshimura, S. *Nature* **1980**, 283, 188.
16. Youshimura, S.; Hachisu, S. *Prog. Colloid Polym. Sci.* **1983**, 68, 59.
17. Kiely, C.J.; Fink, J.; Brust, M.; Bethell, D.; Schiffrin, D.J. *Nature* **1998**, 396, 444.
18. Kiely, C.J.; Fink, J.; Zheng, J.G.; Brust, M.; Bethell, D.; Schiffrin, D.J. *Adv. Mater.* **2000**, 12, 640.
19. Sanders, J.V.; Murray, M.J. *Phil. Mag. A* **1980**, 42, 705; *ibid.*, 721.
20. Pearson, W. B. *Crystal Chemistry and Physics of Metals and Alloys*, Wiley-Interscience, London **1972**.
21. Zeng, H.; Li, J.; Liu, J.P.; Wang, Z.L.; Sun, S. *Nature* **2002**, 420, 395.
22. Puentes, V.F.; Zanchet, D.; Erdonmez, C.K.; Alivisatos, A.P. *J. Am. Chem. Soc.* **2002**, 124, 12874.
23. Mayya, K.S.; Patil, V.; Sastry, M. *Langmuir*; **1997**; 13, 2575.
24. Cecher, G. *Science*, **1997**, 277, 1232.
25. Sun, S.; Anders, S.; Hamann, H.F.; Thiele, J.U.; Baglin, J.E.E.; Thomson, T.; Fullerton, E.E.; Murray, C.B.; Terris, B.D.; *J. Am. Chem. Soc.* **2002**, 124, 2884.
26. Aliev, F.G.; Correa-Duarte, M.A.; Mamedov, A.; Ostrander, J.W.; Giersig, M.; Li-Marzan, L.M.; Kotov, N. *Adv. Mater.* **1999**, 11, 1006.
27. Wyrna, D.; Beyer, N.; Schmid, G. *Nano Lett.* **2002**, 2, 419.
28. Govor, L.V.; Bashmakov, I.A.; Kaputski, F.N.; Pientka, M.; Parisi, J. *Macromol. Chem. Phys.* **2000**, 201, 2721.
29. Bashmakov, I.A.; Govor, L.V.; Solovieva, L.V.; Parisi, J. *Macromol. Chem. Phys.* **2002**, 203, 544.
30. Talapin, D.V.; Shevchenko, E.V.; Kornowski, A.; Gaponik, N.; Haase, M.; Rogach, A.L.; Weller, H. *Adv. Mater.* **2001**, 13, 1868.
31. Chen, Q.; Zhang, Z. *J. Appl. Phys. Lett.* **1998**, 73, 3156.
32. Leslie-Pelecky, D.L.; Rieke, R.D. *Chem. Mater.* **1996**, 8, 1770.
33. Hansen, M.F.; Moerup, S. *J. Magnet. Mater.* **1999**, 203, 214.
34. Russier, V.; Petit, C.; Legrand, J.; Pileni M. P. *Phys. Rev. B* **2000**, 62, 3910-3916.

35. Giersig, M.; Hilgendorff, M. *Colloids and Surfaces A: Physicochemical and Engineering Aspects* **2002**, *202*, 207.
36. Petit, C.; Taleb, A.; Pileni, M.P. *Adv. Mater.* **1998**, *10*, 259.
37. Pileni, M.P. *J. Phys. Chem. B* **2001**, *105*, 3358.
38. Wen W.; Zhang, L.; Sheng, P. *Phys. Rev. Lett.* **2000**, *85*, 5464.
39. Wirtz, D.; Fermigier, M. *Phys. Rev. Lett.* **1994**, *72*, 2294.
40. Wang, H.; Zhu, Y.; Boyd, C.; Luo, W.; Cebers, A.; Rosensweig, R.E. *Phys. Rev. Lett.* **1994**, *72*, 1929.
41. Yablonovitch, E. *Phys. Rev. Lett.* **1987**, *58*, 2059.
42. John, S. *Phys. Rev. Lett.* **1987**, *58*, 2486.
43. Blanco, A.; Chomski, E.; Grabtchak, S.; Ibisate, M.; John, S.; Leonard, S.W.; Lopez, C.; Meseguer, F.; Miguez, H.; Mondia, J.P.; Ozin, G.A.; Toader, O.; van Driel, H.M. *Nature* **2000**, *405*, 437.
44. Gu, Z.Z.; Kubo, S.; Qian, W.; Einaga, Y.; Tryk, D.A.; Fujishima, A.; Sato, O. *Langmuir* **2001**, *17*, 6751.
45. Gates, B.; Xia, Y. *Adv. Mater.* **2001**, *13*, 1605.



## 7. Summary

This thesis deals with the development of novel colloidal synthetic approaches for various magnetic alloy nanocrystals as well as with the theoretical understanding of phenomena governing the nanocrystal nucleation and growth. Highly crystalline particles of platinum – iron,  $\text{CoPt}_3$  and  $\text{CoPd}_2$  magnetic alloys can be prepared in a predictable and reproducible manner via high temperature synthetic routes. The key point of the synthesis is the use of the novel bulky stabiliser 1-adamantancarboxylic acid. All samples were synthesised in the form of stable colloids. The possibility of the shape control of nanocrystals, e.g. controllable formation of spherical, cubic  $\text{CoPt}_3$  nanocrystals and  $\text{CoPt}_3$  nanowires was demonstrated. Elemental analysis, powder XRD, TEM, and HRTEM and SAXS data were used to characterised magnetic alloy nanocrystals. Detailed investigation of the effect of various reaction conditions (reaction temperature, concentration of the precursors and stabilisers) on the size of forming nanocrystals revealed the purely kinetic nature of the nanocrystals growth and the absence of the Ostwald ripening stage. The turning of the nanocrystal size in this case can be achieved via control over the balance between the nucleation and growth rates. To the best of our knowledge, this is the first attempt of a systematic experimental study of the “hot” organometallic synthesis of metal nanocrystals and the mechanism of homogenous nucleation of metal alloy nanocrystals. The experimental results indicate that nucleation of alloy nanocrystals occurs through the formation of some clusters from the precursor of transition metal playing the role of nucleation seeds for further growth of the alloy. The formation of these clusters is the rate-limiting step for the whole nucleation process whereas the concentration of platinum or palladium precursors does not affect the nucleation rate.

The development of novel effective and predictable methods of precise size control of  $\text{CoPt}_3$  nanocrystals allowed the investigation of their size-dependent magnetic properties. The magnetic measurements (hysteresis loops and ZFC/FC scans) revealed a superparamagnetic behaviour of these magnetic alloy nanocrystals at room temperature. The blocking temperature, coercivity and saturation magnetisation strongly depend on the nanocrystals sizes.

The monodisperse magnetic alloy nanocrystals can be organised in one-, two- and three-dimensional superstructures. Mixing different size nanocrystal sample with an appropriate ratio in size and packing fraction lead to the formation of mixed superlattices with high

## 7. Summary

---

packing densities. Crystallisation of monodisperse magnetic alloy nanocrystals in ordered three-dimensional superlattices is achieved via controllable destabilisation of toluene solution of nanocrystals. Perfectly faceted macroscopic ( $\sim 20 - 30$  nm) colloidal crystals of magnetic alloy nanocrystals ( $\text{CoPt}_3$  and  $\text{PtFe}$ ) have been obtained for the first time. HRSEM investigation showed the long range ordered nanocrystals with coherence over ten of microns. An external magnetic field has the strong influence on the arrangement of magnetic nanocrystals into 2D or 3D superstructures. Novel superstructures consisted of magnetic nanocrystals were prepared in an external magnetic field. Formation of periodic concentration stripes of  $\text{CoPt}_3$  nanocrystals was observed in the parallel external magnetic field. When the external magnetic field was applied perpendicular to the substrate different types of needle-like nanocrystal assemblies were obtained. In relatively strong magnetic fields ( $\sim 0.1 - 1$  Tesla) mainly glassy solids with short-range ordering of magnetic nanocrystals were found while in weak magnetic fields ( $\sim 0.01 - 0.02$  Tesla) colloidal “supercrystals” can be formed.

## Experimental Section

**Chemicals.** Toluene, methanol, n-hexane, propanol-2 (all anhydrous, Aldrich), diphenyl ether (99%, Alfa Aesar), n-tetradecylphosphonic acid (n-TDPA, 98%, Alfa Aesar), 1,2-hexadecandiol (90%, Fluka), 1-adamantanecarboxylic acid (ACA, 99%, Fluka), 1,2-dichlorobenzene (99%, Acros Organics), cobalt carbonyl ( $\text{Co}_2(\text{CO})_8$ , stabilised with 1–5% of hexane, Strem), iron pentacarbonyl ( $\text{Fe}(\text{CO})_5$ , 97%, Fluka), palladium (II)-acetylacetonate ( $\text{Pd}(\text{acac})_2$ , 99%, Strem) and platinum(II)-acetylacetonate ( $\text{Pt}(\text{acac})_2$ , 98%, Strem), octadecyl amine (ODA, Merck), dodecylamine (DDA, Merck), tri-*n*-octylphosphine oxide (TOPO, 90%, Aldrich), 1-hexadecanol (Fluka, 97%) were of the highest purity available and used as received. Hexadecylamine (HDA) (Merck) and tri-*n*-octylphosphine (TOP, Fluka) were purified by a vacuum distillation.

**Apparatus.** Optical microscopy, powder X-ray diffraction (XRD), Small-angle X-ray scattering measurements, transmission electron microscopy (TEM and high-resolution TEM (HRTEM)), scanning electron microscopy (SEM and HRSEM) and elemental analysis were used to characterise the nanocrystals. Magnetic measurements have been done using a commercial superconducting quantum interference device (*SQUID*) magnetometer (MPMS2, Quantum Design).

*Optical micrographs* of colloidal crystals were obtained with an Axiovert S 100 microscope (Zeiss).

*UV-Vis absorption spectra* were taken on Cary 500 (Varian) spectrometer.

*XRD* measurements were performed on a Philips X'Pert diffractometer ( $\text{Cu K}_\alpha$ -radiation, variable entrance slit, Bragg-Brentano geometry, secondary monochromator). Samples for these measurements were prepared by dropping colloidal solutions of  $\text{CoPt}_3$  nanocrystals in toluene on standard single crystal Si supports and evaporating the solvent. XRD data reveal the internal structure of the average nanocrystals core and permits measurement of nanocrystal size and shape [1-3]. The width of the diffraction peaks is considerably broadened and decreases with increasing particle size. By using the Debye – Sherrer formula, the mean sizes of the nanocrystals can be calculated from the peak width at half-maximum [4].

*SAXS* measurements were conducted with a modified Kratky compact camera equipped with an imaging-plate detector system (Fuji BAS MS 2525 obtained from Raytest GmbH in

Straubenhardt/Germany). The light source was a standard X-ray tube with a fixed copper target operating at 40 mA and 30 kV. The light was monochromatized (wavelength = 0.1542 nm) by using a Goebel mirror from Bruker AXS. The scattering functions were transformed into size-distribution functions using an updated version of program ORT [5] that allows for the desmearing of slit-width and slit-length broadening as described by Glatter [6,7].

*TEM* and *HRTEM* images were obtained using a Philips CM-300 microscope operated at 300 kV. Samples for these measurements were prepared by depositing a droplet of nanocrystal solution in toluene or hexane onto carbon-coated copper grids. The excess of solvent was wicked away with a filter paper, and the grids were dried in air.

*SEM* images were obtained either on Philips 515 or on Leo 1550 scanning electron microscopes. For these measurement a thin film of gold (~5 – 15 nm) was sputtered on the substrate with the investigated sample. *HRSEM* measurements were performed at a Leo 1550 scanning electron microscopes with a spatial resolution ~1nm. Indium tin oxides (ITO) glasses were used as a substrate for HRSEM analysis.

The elemental composition of the nanocrystals was investigated by *inductively coupled plasma-atomic emission spectroscopy* (ICP AES). For these measurements, CoPt<sub>3</sub> nanocrystals were thoroughly washed to remove most of the organic ligands and subsequently dissolved in the standard HCl/HNO<sub>3</sub> digesting solution.

*SQUID* supplier yields the information on blocking temperature, coercivity, remanent and saturation magnetisation. The device is cooled with liquid helium and the sample can be studied at near liquid helium temperature or up to well above room temperature [8].

**Synthesis of CoPt<sub>3</sub> nanocrystals.** CoPt<sub>3</sub> nanocrystals were formed via a modified ‘polyol’ process [9] in a high-boiling coordinating solvent. The synthesis was carried out using standard Schlenk line technique under dry argon.

*Cobalt stock solution* was freshly prepared before synthesis by dissolving 0.043 g of Co<sub>2</sub>(CO)<sub>8</sub> in 0.4 mL of 1,2-dichlorobenzene at room temperature under airless conditions.

In a typical synthesis, 0.033 g of Pt(acac)<sub>2</sub>, 0.13 g of 1,2-hexadecandiol and 0.084 g of 1-adamantancarboxylic acid were dissolved in a mixture of coordinating solvents and heated to 65°C in a three-neck flask until a clear solution was formed. Three types of coordinating mixtures were used: (i) *diphenyl ether (2.0 mL) and HDA (4.0 g)*, (ii) *diphenyl ether (6.0 mL) and TDPA (0.04 g)* and (iii) *HDA (0.04 g) and 1-hexadecanol (6.0 g)*. To produce CoPt<sub>3</sub> nanocrystals, the reaction mixture was heated either to 100°C or to 170°C and cobalt stock solution was injected into the flask under vigorous stirring. CoPt<sub>3</sub> nanocrystals of 2.6 nm

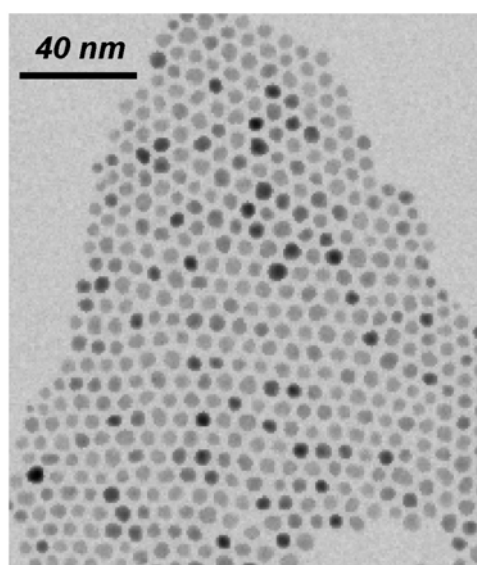
diameter were prepared by injection of a mixture of the cobalt stock solution, 1,2-hexadecandiol and 1.5 ml of diphenylether into HDA-diphenyl ether coordinating mixture at 220°C. Different temperatures and duration of further heating were tested to control the size and the shape of CoPt<sub>3</sub> nanocrystals. The yield of the reaction was ~0.030 of properly washed CoPt<sub>3</sub> nanocrystals for all co-ordinating mixtures and temperatures regimes.

**Additional injections of the precursors.** The method described above allows the preparation of CoPt<sub>3</sub> particles with sizes ranging from ~1.5 to 5.5 nm depending on reaction conditions and the compositions of coordinating mixture. To prepare larger CoPt<sub>3</sub> nanocrystals (up to ~10 nm), additional injections of cobalt and platinum precursors into the reaction mixture were required. We used a solution of precursors prepared by mixing of relevant amounts of Co<sub>2</sub>(CO)<sub>8</sub> (0.0225 g), Pt(acac)<sub>2</sub> (0.0164 g), 1,2-hexadecandiol (0.065 g), 1,2-dichlorobenzene (0.4 mL) and diphenyl ether (3.0 mL). This solution of precursors was dropwise introduced into the reaction mixture at 155°C. After injection, the temperature was slowly (~2 grad/min) increased up to 230°C and heating was continued at this temperature for 40 min. All subsequent injections were carried out at the same conditions.

**Post-preparative procedures.** After cooling the reaction mixture to 50°C all subsequent steps were performed in air. The crude solution of CoPt<sub>3</sub> nanoparticles was mixed with 5 mL of chloroform. Subsequently, 20 mL of ethanol (or propanol-2) were added, resulting in a black precipitate which was isolated by centrifugation. The almost colorless supernatant was discarded. The precipitate was re-dissolved in chloroform (~5 mL) and filtered through a PTFE 0.2 µm filter. To wash out the excess of stabilisers, the nanocrystals were precipitated again by addition of ~20 mL of ethanol and centrifuged. The resulting black precipitate containing CoPt<sub>3</sub> nanocrystals can be re-dissolved in various nonpolar solvents (toluene, hexane, chloroform, etc.). The colour of the solution was changed from black-brown to brown in accordance with the concentration of CoPt<sub>3</sub> nanocrystals. Small amount (~0.1 mg) of HDA can be added to nanocrystals prepared in TDPA - diphenyl ether coordinating mixture to improve their solubility.

When the synthesis described above yielded monodisperse samples, no further size selection was applied. If a distribution of nanocrystals size was observed, the conventional solvent/nonsolvent size selective precipitation technique [36,38] was applied. Hexane and ethanol were used as solvent and non-solvent, respectively.

**Size histograms of different size fractions of as –prepared  $\text{CoPt}_3$  nanocrystals.** Size distributions of nanocrystals were calculated by the computer processing TEM images using the commercial software *NIH image*. Metal nanocrystals look like highly contrast “dark spots” at the TEM images. The program calculates the amount of pixels in highly contrast objects and hence the their area. Assuming the spherical shape of nanocrystals one can find the diameter of nanocrystals. Usually  $\sim 370 - 2000$  nanoparticles were taken into account to estimate the dispersity of the samples.



Minimal size, nm	1.3
Maximal size, nm	7.2
The amount of nanocrystals	741
Mean size, nm	4.79
Standard deviation, nm	0.68
Standard deviation, %	14.2

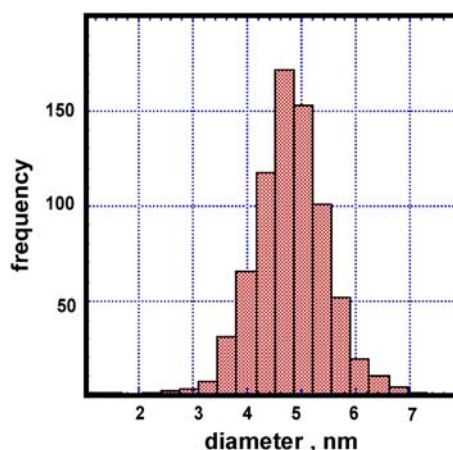
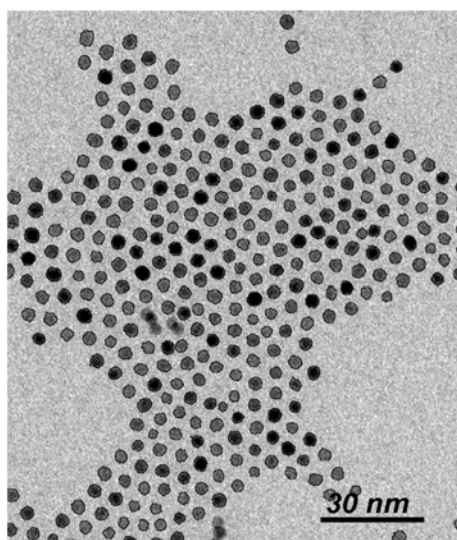


**Figure ES.1.** *Size histogram of  $\text{CoPt}_3$  nanocrystals by injection of cobalt stock solution at  $100^\circ\text{C}$  into HDA-diphenyl ether coordinating mixture.*



Minimal size, nm	2.5
Maximal size, nm	5.0
The amount of nanocrystals	798
Mean size, nm	3.8
Standard deviation, nm	0.34
Standard deviation, %	8.9

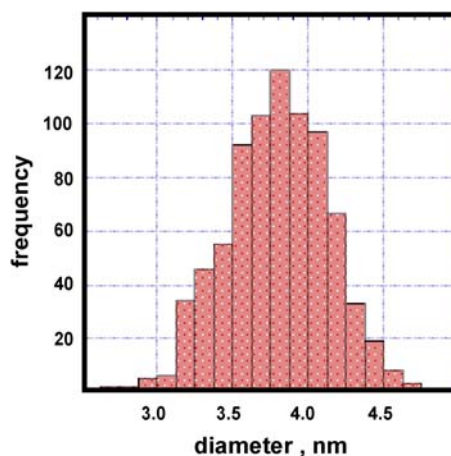
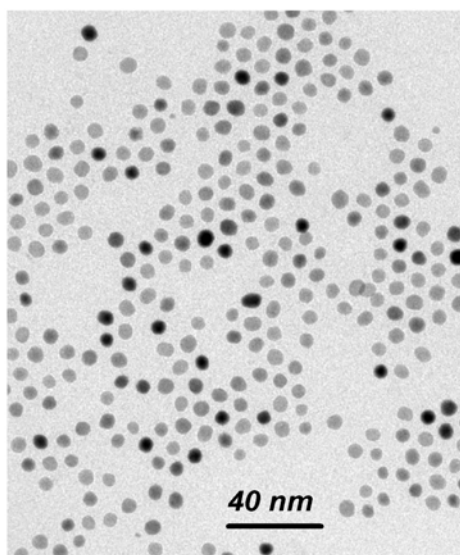


**Figure ES.2.** Size histogram of as-prepared  $\text{CoPt}_3$  nanocrystals by injection of cobalt stock solution at  $170^\circ\text{C}$  into HDA-diphenyl ether coordinating mixture.



Minimal size, nm	1.63
Maximal size, nm	8.07
The amount of nanocrystals	375
Mean size, nm	6.18
Standard deviation, nm	0.74
Standard deviation, %	12

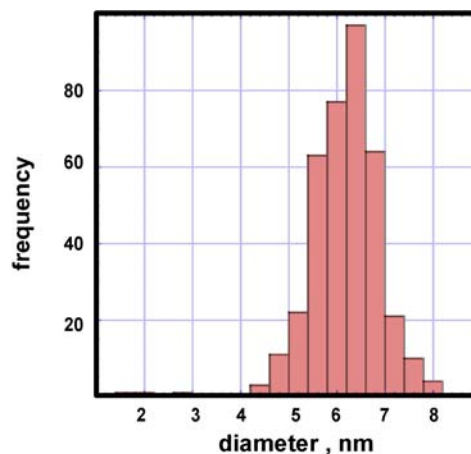


**Figure ES.3.** Size histogram of as-prepared 6.2 nm  $\text{CoPt}_3$  nanocrystals obtained by additional injection of platinum and cobalt precursors from 4.0 nm  $\text{CoPt}_3$  nanocrystals.

**Post-preparative size selective fractionation.** Size distribution of polydisperse nanocrystals can be narrowed by dividing of the initial solution into a series of fractions. This technique is widely applied to colloids of semiconductor particles [10,11]. Size selective precipitation based on stepwise addition of a nonsolvent into a solution of nanocrystals. Adding a nonsolvent results in gentle destabilisation of colloidal solution and aggregation of nanocrystals. Since larger nanocrystals exhibit greater attractive van der Waals forces [12], the addition of a nonsolvent results in the aggregation of the largest particles in a given sample, while the particles with smaller sizes are still stable. Sequential precipitation of fractions and collection them by centrifugation allows the isolation of particles with different sizes with a narrowed size distribution. If the nanoparticles are sensitive to oxidation, all steps of size-selective precipitation have to be carried out under inert atmosphere. For magnetic nanocrystals, the size-selective precipitation technique can also be performed by applying an external magnetic field as larger particles usually exhibit stronger attractive magnetic forces and precipitate in the magnetic field before smaller nanocrystals [13,14].

To narrow size distribution of CoPt<sub>3</sub> or PtFe nanoparticles ~20 mg of washed nanoparticles were dissolved in ~20 mL of chloroform. After each addition of 5 mL of propanol-2 the solution was centrifuged. Precipitated nanocrystals were collected and redispersed in appropriate solvent like toluene, chloroform or hexane. By this way the starting colloidal solution can be divided into ~ 5 –7 fraction with size distribution ~ 5 – 7 %. In the case of relatively large nanocrystals (9–10 nm) isolation of the largest nanocrystals of the sample was performed by the application of external magnetic field (~0.68 T).

**Investigation of the nucleation and growth of CoPt<sub>3</sub> nanocrystals.** CoPt<sub>3</sub> nanocrystals were synthesised in a high-boiling hexadecylamine - diphenyl ether coordinating mixture. The synthesis was carried out using standard Schlenk line technique under dry argon. In a typical synthesis, relevant amounts of 1,2-hexadecandiol (0.13g, 0.5 mmol), Pt(acac)<sub>2</sub> (0.0328 g, 0.083 mmol) and 1-adamantancarboxylic acid (0.25 g, 1.4 mmol) were dissolved in a mixture of 4 g HDA and 2 ml of diphenyl ether and heated to 65°C in a three-neck flask until a clear solution was formed. Then, the solution was heated to a certain temperature in the range from 140°C to 220°C and the cobalt stock solution was swiftly injected into the hot reaction mixture under vigorous stirring. Note that the volume of the cobalt stock solution is much smaller than the total volume of the reaction mixture and injection does not considerably change the temperature of the reaction mixture. The temperature of injection of the stock solution is referred to as “reaction temperature”. After

injection the colour changes from pale yellowish to black indicating the formation of CoPt<sub>3</sub> nanocrystals. Further heating usually continued for 1 h at the injection temperature and was followed by annealing at refluxing temperature (~275-285°C) for 1 h. The cobalt stock solution has to be freshly prepared before the synthesis by dissolving 0.043 g (0.125 mmol, a typical recipe, all other cases are summarized in Table 3.1) of Co<sub>2</sub>(CO)<sub>8</sub> in 0.6 – 0.7 mL of 1,2-dichlorobenzene at ~35 °C under airless conditions. The molar ratio of 1,2-hexadecandiol to Pt(acac)<sub>2</sub> was always kept as 6 to 1. The detailed conditions for the preparation of colloidal CoPt<sub>3</sub> nanocrystals ranging from ~3 to 18 nm are summarised in Table ES.1 and are discussed in more detail in the text of this chapter. The nanocrystal sizes could be reproduced from run to run (within a ~10 % deviation).

**Table ES.1.** Experimental conditions for the preparation of CoPt<sub>3</sub> nanocrystals.\*

Pt(acac) <sub>2</sub> , g	Co <sub>2</sub> (CO) <sub>8</sub> , g	ACA, g	Molar ratio Pt-to-Co-to-ACA	T <sub>injection</sub> , °C	XRD-size, nm
0.033	0.043	0.25	1 : 3 : 6	220	3.7
				215	3.9
				200	4.9
				170	6.3
				145	9.3
0.033	0.086	0.25	1 : 6 : 6	200	3
	0.022		1 : 1.5 : 6		6.6
	0.014		1 : 1 : 6		9.1
	0.009		1 : 0.6 : 6		10.5
0.066	0.014	0.25	2 : 1 : 6	200	10.2
0.017			0.5 : 1 : 6		7.5
0.011			0.33 : 1 : 6		6.6
0.007			0.2 : 1 : 6		5.7
0.033	0.009	0.25	1 : 0.6 : 6	145	17
	0.014		1 : 1 : 6		14
	0.065		1 : 4.5 : 6		6.7
0.033	0.022	0.25	1 : 1.5 : 6	160	9.1
	0.016		1 : 1.1 : 6	170	9.3
	0.014		1 : 1 : 6	180	9.0
	0.009		1 : 0.6 : 6	190	8.9
0.033	0.043	0.025	1 : 3 : 0.6	170	2.9
		0.083	1 : 3 : 2		3.8
		0.415	1 : 3 : 10		7.5

- \* Amounts of the other chemicals were chosen as follows: 1,2-hexadecandiol - 0.13g; of HDA - 4 g and diphenyl ether - 2 ml.

### **Synthesis of PtFe nanocrystal:**

*OA-Oleyl amine approach.* FePt nanocrystals have been synthesized by the method of Ref. [3]. Under airless conditions, platinum acetylacetonate (0.25 mmol) and 1,2-hexadecandiol (0.75 mmol) were dissolved in 10 mL of dioctylether and heated to 100°C. Oleic acid (0.25 mmol), oleyl amine (0.25 mmol), and Fe(CO)<sub>5</sub> (0.5 mmol) were added to the mixture, which was subsequently heated for 30 min at 300 °C and cooled to room temperature. Post-preparative washing and size-selective precipitation were carried out under air using hexane and ethanol as a solvent and non-solvent, respectively.

*TDPA-ACA approach.* Under airless conditions, platinum acetylacetonate (0.033 g), ACA (0.3 g), TDPA (0.04 g) and 1,2-hexadecandiol (0.13 g) were dissolved in 6 mL of di-phenyl ether at 65 °C, heated to 190 °C and Fe(CO)<sub>5</sub>\* (0.2 mL) was added. The reaction mixture was kept at 190 °C during ~30 min and after that the reaction mixture was heated at 230 °C for ~40 min and cooled to room temperature. Post-preparative washing of nanoparticles was carried out in air using hexane and ethanol as a solvent and non-solvent, respectively.

*ACA-primary amine approach.* Under airless conditions, platinum acetylacetonate (0.033 g), ACA (0.3 g), 1,2-hexadecandiol (0.13 g) and primary amine (either DDA, or HDA, or ODA) (4g) were mixed with di-phenyl ether (2 mL) at 65 °C, heated to injection temperature (170, 200 or 214 °C) and Fe(CO)<sub>5</sub>\* (0.2 mL) was added. Reaction mixture was heated at 190 °C during ~30 min and after that the reaction mixture was heated at 230 °C for ~40 min and cooled to room temperature. Post-preparative washing of nanoparticles was carried out in air using hexane and ethanol as a solvent and non-solvent, respectively.

---

\* *The solution of cyclopentadienyliron dicarbonyl dimer (0.06g) in dichlorobenzene (1mL) can be used as an iron precursor instead of Fe(CO)<sub>5</sub>.*

**Synthesis of CoPd<sub>2</sub> nanocrystals.** Under airless conditions, palladium acetylacetonate (0.025 g), ACA (0.083 g), 1,2-hexadecandiol (0.13 g), HDA (4g) and di-phenyl ether (2 mL) were mixed at 65 °C. Freshly prepared cobalt stock solution (0.062 g of Co<sub>2</sub>(CO)<sub>8</sub> in 0.8 mL of dichlobenzene) was injected to the reaction mixture at 125 °C or at 100 °C. After that reaction mixture was heated to 230 °C and kept at 230 °C during ~1 h and cooled to room temperature. Post-preparative washing of nanoparticles was carried out in air using hexane and ethanol as a solvent and non-solvent, respectively.

Post-preparative procedures of as-prepared platinum-iron and cobalt-palladium alloy nanocrystals were performed to remove the excess of organic.

**Preparation of CoPt<sub>3</sub> nanocrystals – polylaurylmethacrylate composite.** CoPt<sub>3</sub> nanocrystals were formed as described above. The synthesised nanocrystals were isolated from the growth solution, washed from the stabilisers (ACA and HDA) and re-dispersed into laurylmethacrylate monomer. Then, ethylenecycol dimethacrylate crosslinker was added to the solution of nanocrystals in monomer with 1:4 volume ratio of cross-linker to monomer. After addition of azobisisobutyronitrile (AIBN) (~1 wt.%) the solution was transferred to a glass tube and radical polymerisation was initiated by heating of the sample at 75 - 80 °C under argon and continued for ~3 - 4 h. Concentration of nanocrystals in composites materials can be easily varied from ~0.01% up to 21 % by dissolving of appropriate amount of nanocrystals in monomer solution.

**Growing the colloidal crystals of CoPt<sub>3</sub> and PtFe nanoparticles.** Monodisperse CoPt<sub>3</sub> or PtFe nanocrystals prepared in HDA - diphenyl ether or in OA – oleyl amine coordinating mixture respectively were thoroughly washed from the excess of stabilising agents and re-dissolved in toluene in a concentration of about 2 mg/mL. PtFe and CoPt<sub>3</sub> 3D colloidal supercrystals were grown from their colloidal solution using the recently introduced three-layer technique of controlled oversaturation [15]. Glass tubes (30 cm in length and 0.5 cm in diameter) were filled with colloidal solutions of CoPt<sub>3</sub> or PtFe nanocrystals to a height of 15 cm. Then the layers of propanol-2 (7 cm) and methanol (7 cm) were carefully added on top of the CoPt<sub>3</sub> colloidal solution. The crystallisation of nanoparticles into 3D colloidal crystals continued for app. 2 - 3 weeks. The decolouration of the colloidal solution of nanocrystals was used as an indicator of the end of crystallisation process. After crystallisation the supernatant solution was carefully removed from the crystallisation tubes

and the formed aggregates were analysed by methods of optical microscopy, SEM and TEM. To obtain high resolved images of 3D supercrystals, they were transferred from the crystallisation tubes to conductive substrates (indium tin oxide (ITO) glass) and analysed by HRSEM.

### References:

1. Murray, C.B.; Norris, D.J.; Bawendi, M.G. *J. Am. Chem. Soc.* **1993**, *115*, 8706.
2. Bawendi, M.G.; Kortan, A.R.; Stegerwald, M.L.; Brus, L.E. *J. Chem. Phys.* **1989**, *91*, 7282.
3. Hall, B.D.; Monot R. *Comput. Phys.* **1991**, *5*, 414.
4. Lanriat, J.P. *Introduction a la cristallographie et a la diffraction*. Rayons X. Paris Onze Ed. K150, 1998, p.134.
5. Schnablegger H.; *Appl. Optics* **1991**, *30*, 4889.
6. Glatter, O. *J. Appl. Cryst.* **1977**, *10*, 415.
7. Glatter, O. *J. Appl. Cryst.* **1980**, *13*, 7.
8. Klabunde, K. *Nanoscale in Chemistry* **2001**, John Wiley & Sons, Inc.
9. Sun, S.; Murray, C.B.; Weller, D.; Folks, L.; Moser, A. *Science* **2000**, *287*,1989.
10. Chemseddine , A.; Weller, H. *Ber. Bunsenges. Chem.* **1993**, *97*, 636.
11. Murray, C.B.; Norris, D.J.; Bawendi, M.G. *J. Am. Chem. Soc.* **1993**, *115*, 8706.
12. Murray, C.B.; Kagan, C.R.; Bawendi M.G. *Annu. Rev. Mater. Sci.* **2000**, *30*, 545.
13. Murray, C.B.; Sun, S.; Doyle, H.; Betley, T. *MRS Bulletin* **2001**, 985.
14. Puentes, V.F.; Zanchet, D.; Erdonmez, C.K.; Alivisatos, A.P. *J. Am. Chem. Soc.* **2002**, *124*, 12874.
15. Talapin, D.V.;Shevchenko, E.V.; Kornowski, A.; Gaponik, N.; Haase, M.; Rogach, A.L.; Weller, H. *Adv. Mater.* **2001**, *13*, 1868.

## Safety precaution information on the used chemicals

Substance	R-phrases	S-phrases	Hazard signs
Acetone	11-36-66-67	9-16-26	[F][Xi]
Adamantanecarboxylic acid	1	26-24/25	
Adamantylacetic acid	1	22-24/25	
Cobalt acetylacetonate	22-40	7-22-26-37/39	[Xn]
1,2-dichlorobenzene	22-36/37/38-50/53	23-60-61	[Xn][N]
Dicobalt octacarbonyl	11-22-26-40- 48/20-52/53-62- 65-67	16-28-36/37-45-62	[F][T]
Dioctylether	1	23-24/25	
Dodecylamine	22-35	26-28.1-36/37/39-45	[C]
di-phenyl ether	51/53	60-61	[Xn]
Ethanol	11	7-16	[F]
1,2-Hexadecandiol	1	22-24/25	
1-Hexadecanol	36/37/38	22-24/25	
Hexadecylamine	34	26-36/37/39-45	[C]
Hexane	11-48/20	9-16-24/25-29-51	[F][Xn][N]
Iron pentacarbonyl	11-26/27/28	16-26-28-45-36/37/39	[F][T]
Isopropanol	11	7-16	[F][Xi]
Methanol	11-23/25	7-16-24-45	[F][T+]
Octadecylamine	36/37/38	26-37	[Xi]
Palladium(II)- acetylacetonate	36/37/38	26-36	[Xn]
Platinum(II)-acetylacetonate	20/21/22- 36/37/38-63	26-36/37/39	[Xn]
Toluene	11-20	16-25-29-33	[F][Xn]
Tri-n-butylphosphine	17-34	16-26-27-36/37/39	[C][Xi]
Trioctylphosphine	36/37/38	26-36	[Xi]
Trioctylphosphine oxide	34-50/53	26-36/37/39-45-60-61	[C][Xi]

**Risk (R-) and safety precaution (S-) phrases** used in the classification, packaging, labelling and provision of information on dangerous substances

**Risk phrases (R-Phrases)**

- R1: Explosive when dry
- R2: Risk of explosion by shock, friction fire or other sources of ignition
- R3: Extreme risk of explosion by shock friction, fire or other sources of ignition
- R4: Forms very sensitive explosive metallic compounds
- R5: Heating may cause an explosion
- R6: Explosive with or without contact with air
- R7: May cause fire
- R8: Contact with combustible material may cause fire
- R9: Explosive when mixed with combustible material
- R10: Flammable
- R11: Highly flammable
- R12 : Extremely flammable
- R13: Extremely flammable liquefied gas
- R14: Reacts violently with water
- R15: Contact with water liberates highly flammable gases
- R16: Explosive when mixed with oxidising substances
- R17: Spontaneously flammable in air
- R18: In use, may form flammable/explosive vapour-air mixture
- R19: May form explosive peroxides
- R20: Harmful by inhalation
- R21: Harmful in contact with skin
- R22: Harmful if swallowed
- R23: Toxic by inhalation
- R24: Toxic in contact with skin
- R25: Toxic if swallowed
- R26: Very toxic by inhalation
- R27: Very toxic in contact with skin
- R28: Very toxic if swallowed
- R29: Contact with water liberates toxic gas
- R30: Can become highly flammable in use
- R31: Contact with acids liberates toxic gas
- R32: Contact with acids liberates very toxic gas
- R33: Danger of cumulative effects
- R34: Causes burns
- R35: Causes severe burns
- R36: Irritating to eyes
- R37: Irritating to respiratory system
- R38: Irritating to skin
- R39: Danger of very serious irreversible effects
- R40: Possible risk of irreversible effects
- R41: Risk of serious damage to eyes
- R42: May cause sensitisation by inhalation
- R43: May cause sensitisation by skin contact
- R44: Risk of explosion if heated under confinement
- R45: May cause cancer
- R46: May cause heritable genetic damage
- R47: May cause birth defects
- R48: Danger of serious damage to health by prolonged exposure
- R49: May cause cancer by inhalation
- R50: Very toxic to aquatic organisms
- R51: Toxic to aquatic organisms

R52: Harmful to aquatic organisms  
R53: May cause long-term adverse effects in the aquatic environment  
R54: Toxic to flora  
R55: Toxic to fauna  
R56: Toxic to soil organisms  
R57: Toxic to bees  
R58: May cause long-term adverse effects in the environment  
R59: Dangerous to the ozone layer  
R60: May impair fertility  
R61: May cause harm to the unborn child  
R62: Possible risk of impaired fertility  
R63: Possible risk of harm to the unborn child  
R64: May cause harm to breastfed babies

**Combination of risks**

R14/15: Reacts violently with water, liberating highly flammable gases  
R15/29: Contact with water liberates toxic, highly flammable gas  
R20/21: Harmful by inhalation and in contact with skin  
R20/21/22: Harmful by inhalation, in contact with skin and if swallowed  
R20/22: Harmful by inhalation and if swallowed  
R21/22: Harmful in contact with skin and if swallowed  
R23/24: Toxic by inhalation and in contact with skin  
R23/24/25: Toxic by inhalation, in contact with skin and if swallowed  
R23/25: Toxic by inhalation and if swallowed  
R24/25: Toxic in contact with skin and if swallowed  
R26/27: Very toxic by inhalation and in contact with skin  
R26/27/28: Very toxic by inhalation, in contact with skin and if swallowed  
R26/28: Very toxic by inhalation and if swallowed  
R27/28: Very toxic in contact with skin and if swallowed  
R36/37: Irritating to eyes and respiratory system  
R36/37/38: Irritating to eyes, respiratory system and skin  
R36/38: Irritating to eyes and skin  
R37/38: Irritating to respiratory system and skin  
R42/43: May cause sensitisation by inhalation and skin contact.  
R48/20: Harmful: danger of serious damage to health by prolonged exposure  
R48/20/21: Harmful: danger of serious damage to health by prolonged exposure through inhalation and in contact with the skin  
R48/20/21/22: Harmful: danger of serious damage to health by prolonged exposure through inhalation, in contact with skin and if swallowed  
R48/20/22: Harmful: danger of serious damage to health by prolonged exposure through inhalation, and if swallowed  
R48/21: Harmful: danger of serious damage to health by prolonged exposure in contact with skin  
R48/21/22: Harmful: danger of serious damage to health by prolonged exposure in contact with skin and if swallowed  
R48/22: Harmful: danger of serious damage to health by prolonged exposure if swallowed  
R48/23: Toxic: danger of serious damage to health by prolonged exposure through inhalation  
R48/23/24: Toxic: danger of serious damage to health by prolonged exposure through inhalation and in contact with skin  
R48/23/24/25: Toxic: danger of serious damage to health by prolonged exposure through inhalation, in contact with skin and if swallowed  
R48/23/25: Toxic: danger of serious damage to health by prolonged exposure through inhalation and if swallowed  
R48/24: Toxic: danger of serious damage to health by prolonged exposure in contact with skin  
R48/24/25: Toxic: danger of serious damage to health by prolonged exposure in contact with skin and if swallowed  
R48/25: Toxic: danger of serious damage to health by prolonged exposure if swallowed

R50/53: Very toxic to aquatic organisms, may cause long term adverse effects in the aquatic environment

R51/53: Toxic to aquatic organisms, may cause long term adverse effects in the aquatic environment

R52/53: Harmful to aquatic organisms, may cause long-term adverse effects in the aquatic environment

**Safety precaution phrases (S-Phrases)**

S1: Keep locked up

S2: Keep out of reach of children

S3: Keep in a cool place

S4: Keep away from living quarters

S5: Keep contents under . . . (appropriate liquid to be specified by the manufacturer)

S6: Keep under . . . (inert gas to be specified by the manufacturer)

S7: Keep container tightly closed

S8: Keep container dry

S9: Keep container in a well ventilated place

S12: Do not keep the container sealed

S13: Keep away from food, drink and animal feeding stuffs

S14: Keep away from . . . (incompatible materials to be indicated by the manufacturer)

S15: Keep away from heat

S16: Keep away from sources of ignition-No Smoking

S17: Keep away from combustible material

S18: Handle and open container with care

S20: When using do not eat or drink

S21: When using do not smoke

S22: Do not breathe dust

S23: Do not breathe gas/fumes/vapour/spray (appropriate wording to be specified by manufacturer)

S24: Avoid contact with skin

S25: Avoid contact with eyes

S26: In case of contact with eyes, rinse immediately with plenty of water and seek medical advice

S27: Take off immediately all contaminated clothing

S28: After contact with skin, wash immediately with plenty of . . (to be specified by the manufacturer)

S29: Do not empty into drains

S30: Never add water to this product

S33: Take precautionary measures against static discharges

S34: Avoid shock and friction

S35: This material and its container must be disposed of in a safe way

S36: Wear suitable protective clothing

S37: Wear suitable gloves

S38: In case of insufficient ventilation, wear suitable respiratory equipment

S39: Wear eye/face protection

S40: To clean the floor and all objects contaminated by this material use (to be specified by the manufacturer)

S41: In case of fire and/or explosion do not breath fumes

S42: During fumigation/spraying wear suitable respiratory equipment (appropriate wording to be specified by the manufacturer)

S43: In case of fire, use ... (indicate in the space the precise type of fire fighting equipment. If water increases the risk, add "never use water")

S44: If you feel unwell, seek medical advice (show the label where possible)

S45: In case of accident or if you feel unwell, seek medical advice immediately (show the label where possible)

S46: If swallowed, seek medical advice immediately and show the container or label

S47: Keep at temperature not exceeding ... °C (to be specified by the manufacturer)

S48: Keep wetted with ... (appropriate material to be specified by the manufacturer)

S49: Keep only in the original container  
S50: Do not mix with ... (to be specified by the manufacturer)  
S51: Use only in well ventilated areas  
S52: Not recommended for interior use on large surface areas  
S53: Avoid exposure - obtain special instructions before use  
S54: Obtain the consent of pollution control authorities before discharging to waste-water treatment plants  
S55: Treat using the best available techniques before discharge into drains or the aquatic environment  
S56: Do not discharge into drains or the environment, dispose to an authorised waste collection point  
S57: Use appropriate containment to avoid environmental contamination  
S58: To be disposed of as hazardous waste  
S59: Refer to manufacturer/supplier for information on recovery/recycling  
S60: This material and/or its container must be disposed of as hazardous waste  
S61: Avoid release to the environment. Refer to special instructions / safety data sheet  
S62: If swallowed, do not induce vomiting: seek medical advice immediately and show the container or label

**Combined safety phrases**

S1/2: Keep locked up and out of reach of children  
S3/9: Keep in a cool, well ventilated place  
S3/7/9: Keep container tightly closed in a cool, well ventilated place  
S3/14: Keep in a cool place away from ... (incompatible materials to be indicated by the manufacturer)  
S3/9/14: Keep in a cool, well ventilated place away from ... (incompatible materials to be indicated by the manufacturer)  
S3/9/49: Keep only in the original container in a cool, well ventilated place  
S3/9/14/49: Keep only in the original container in a cool, well ventilated place away from (incompatible materials to be indicated by the manufacturer)  
S3/9/49: Keep only in the original container in a cool, well ventilated place  
S3/14: Keep in a cool place away from...(incompatible materials to be indicated by the manufacturer)  
S7/8: Keep container tightly closed and dry  
S7/9: Keep container tightly closed and in a well ventilated place  
S7/47: Keep container tightly closed and at a temperature not exceeding...°C (to be specified by manufacturer)  
S20/21: When using do not eat, drink or smoke  
S24/25: Avoid contact with skin and eyes  
S29/56: Do not empty into drains, dispose of this material and its container to hazardous or special waste collection point  
S36/37: Wear suitable protective clothing and gloves  
S36/37/39: Wear suitable protective clothing, gloves and eye/face protection  
S36/39: Wear suitable protective clothing, and eye/face protection  
S37/39: Wear suitable gloves and eye/face protection  
S47/49: Keep only in the original container at temperature not exceeding...°C (to be specified by the manufacturer)



# CURRICULIM VITAE



**Elena V. Shevchenko**

**DATE AND PLACE OF BIRTH:**  
March, 3, 1977; Korma, USSR

## EDUCATION

- 1998                      Diploma (honors), Chemistry, Belarusian State University, Minsk, Belarus  
1993                      Diploma (honors), Secondary School, Minsk, Belarus

## PROFESSIONAL EXPERIENCE

- 2000–2003              Ph. D. student, Institute of Physical Chemistry, University of Hamburg, Hamburg, Germany, with Prof. Dr. Horst Weller  
July 1998                Probationer Researcher, Institute of General and Inorganic Chemistry, Belarusian National Academy of Sciences, (Minsk)  
October 1998            Junior Research Scientist & Postgraduate Student, Institute of General and Inorganic Chemistry, Belarusian National Academy of Sciences, (Minsk).  
Since November 1998-2000

## TEACHING EXPERIENCE

- 2001-2002              Practical experiments in physical chemistry (BET, polarography and kinetic), University of Hamburg

## AWARDS

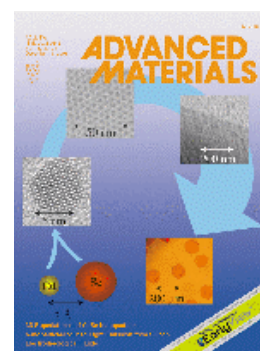
- 2002                      Poster Prize, Gertner Symposium in Chemistry on Ascending the Materials Hierarchy, Potsdam  
2000                      Poster Prize, Highly organised catalytic systems, Moscow.  
1997                      Diploma of the Ministry of Education of Belarus

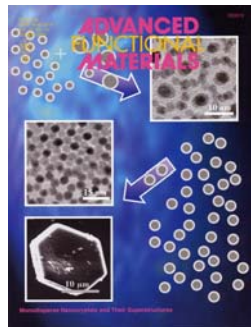
## RESEARCH PROJECTS

- 2000/2002              EU project – Bioand (biomolecule driven assembly of nanoparticles based electronic devices)

**PUBLICATION**

1. **E. Shevchenko**, E. Matiushenkov, D. Kochubey, D. Sviridov, A. Kokorin, A. Kulak. Synthesis of carbon films with diamond-like structure by electrochemical oxidation of lithium acetylide. *Chem. Commun.* **2001**, 317-318.
2. **E. V. Shevchenko**, G.I.Kurnevich, A.I.Kulak, V.V.Sviridov. Electrochemical behaviour of thermal splitted graphite. *Proc. Akad. Sci. Belarusi, Ser Chem. Sci.* **2001**, 45, 67-69.
3. **E. V. Shevchenko**, A.I.Kulak. Electrodes based onto carbon fibres and modified with polyanilin coating to measure pH. *Proc. Akad. Sci. Belarusi, Ser Chem. Sci.* **2001**, 45, 58-60.
4. Dmitry V. Talapin, **Elena V. Shevchenko**, Andreas Kornowski, Nikolai Gaponik, Markus Haase, Andrey L. Rogach, and Horst Weller. A New Approach to Crystallization of CdSe Nanoparticles into Ordered Three-Dimensional Superlattices. *Adv. Mater.* **2001**, 13, 1868- 1871.
5. **Elena Shevchenko**, Dmitry Talapin, Andreas Kornowski, Frank Wiekhorst, Jürgen Kötzler, Markus Haase, Andrey Rogach, and Horst Weller. Colloidal Crystals of Monodisperse FePt Nanoparticles Grown by a Three-Layer Technique of Controlled Oversaturation. *Adv. Mater.* **2002**, 14, 287-289.
6. Dmitry V. Talapin, Andrey L. Rogach, **Elena V. Shevchenko**, Andreas Kornowski, Markus Haase, and Horst Weller Dynamic Distribution of Growth Rates within the Ensembles of Colloidal II-VI and III-V Semiconductor Nanocrystals as a Factor Governing Their Photoluminescence. *J. Am. Chem. Soc.* **2002**, 124, 5782-5790.
7. **Elena Shevchenko**, Dmitry Talapin, Andreas Kornowski, Andrey Rogach, and Horst Weller Colloidal Synthesis and Self-Assembly of CoPt<sub>3</sub> Nanocrystals *J. Am. Chem. Soc.* **2002**, 124, 11480-11485.



8. Nikolai Gaponik, Dmitry V. Talapin, Andrey L. Rogach, Kathrin Hoppe, **Elena V. Shevchenko**, Andreas Kornowski, Alexander Eychmüller, and Horst Weller. Thiol-Capping of CdTe Nanocrystals: An Alternative to Organometallic Synthetic Routes. *J. Phys. Chem. B* **2002**, *106*, 7177-7185.
9. Andrey L. Rogach, Dmitry V. Talapin, **Elena V. Shevchenko**, Andreas Kornowski, and Horst Weller. Organisation of Matter on Different Size Scales: Monodisperse Nanocrystals and their Superstructures. *Adv. Func. Mater.* **2002**, *12*, 653-664.
- 
10. F. Wiekhorst, **E. Shevchenko**, H. Weller, and J. Kötzler. Anisotropic Superparamagnetism of Monodisperse Cobalt-Platinum Nanocrystals. **2003**, *Phys. Rev. B*. *In press*.
11. **Elena Shevchenko**, Dmitry Talapin, Heimo Schablegger, Andreas Kornowski, and Horst Weller. Study of Nucleation and Growth in the “hot” organometallic synthesis of magnetic alloy nanocrystals: the role of nucleation rate in size tuning of CoPt<sub>3</sub> nanocrystals. **2003**, *J. Am. Chem. Soc.* *In press*.
12. **Elena Shevchenko**, Dmitry Talapin, Andrey Rogach and Horst Weller. Monodisperse Magnetic Nanoparticles and Their Superstructures. In “Assemblies and Superstructures of Magnetic Nanoparticles”, edited by N. Kotov. **2003**, Marcel Dekker, Inc., submitted.
13. D. V. Talapin, **E. V. Shevchenko**, H. Weller. Synthesis and characterization of magnetic Nanoparticles. In "Nanoparticles – from Theory to Applications." Ed. G. Schmid, WILEY VCH, submitted.

**PRESENTATION**

1. *Electrocatalytical and photocatalytical systems based on the carbony fibers modified by semiconductor, metal and polymer layers.* **E. Shevchenko**. Highly-organised catalytical systems, Moscow, June, 2000. (poster)
2. *Organisation of matter on different size scales: Monodisperse nanocrystals and their superstructures.* **Elena V. Shevchenko**, Dmitry V. Talapin. Potsdam, April, 2002. (poster)
3. *Self-Assembly of Colloidal Semiconductor and Magnetic Nanoparticles.* **Elena Shevchenko**, Dmitri Talapin, Andreas Kornowski, Nikolai Gaponik, Andrey Rogach, Markus Haase, Horst Weller. 101<sup>th</sup> Bunsentagung, Potsdam, 2002. (poster)
4. *Synthesis and self-assembly of magnetic and semiconductor nanocrystals.* **Elena Shevchenko**, Dmitry Talapin and Horst Weller. Mel-Ari/NID Workshop, Helsinki, Juli, 2002. (poster)
5. *Monodisperse magnetic nanocrystals and their superstructures.* **Elena Shevchenko**. Correlation of Structure and Magnetism in Novel Nanoscale. Workshop, Duisburg, March, 2003. (oral)

## **Declaration**

The materials contained in this thesis is the result of my own work and all sources of information as well as the results obtained in collaboration with other people are pointed out.

This dissertation has not been submitted in whole or in part for the award of a degree at this of any other university.

Hamburg, May 2003

Elena V. Shevchenko



## Zusammenfassung

In der vorliegenden Arbeit wurden neue Methoden für die Synthese verschiedener magnetischer Legierungsnanoteilchen entwickelt. Spezielle Aufmerksamkeit wurde hierbei auf das theoretische Verständnis der Phänomene, welche die Nukleation und das Wachstum der Nanoteilchen regeln, gerichtet.

Hochgradig kristalline Partikel der magnetischen Legierungen sowie der  $Pt_xFe_{1-x}$ ,  $CoPt_3$  und  $CoPd_2$  Teilchen wurden in vorhersagbarer und reproduzierbarer Weise über Hochtemperatursynthese dargestellt. Der Schlüssel zu dieser Synthese ist der Gebrauch des neuen sterisch anspruchsvollen Stabilisators - 1-Adamantancarbonsäure. Alle Proben wurden in Form von stabilen Kolloiden synthetisiert.

Die Kontrollmöglichkeiten der „Formen“ der Nanoteilchen, z.B. die kontrollierbare Synthese der sphärischen und der würfelförmige Nanoteilchen sowie der  $CoPt_3$  Nanodrähte, wurden demonstriert. Elementar-Analyse, Pulver XRD, TEM- und HRTEM und SAXS Daten wurden verwendet, um die magnetischen Legierungsnanoteilchen zu charakterisieren. Ausführliche Untersuchungen der Einflüsse der verschiedenen Reaktionsbedingungen (Reaktionstemperatur, Konzentration der Prekursoren und Stabilisatoren) auf die Größe der Nanoteilchen deckte die ausschließlich kinetische Natur des Nanoteilchenwachstums und das Fehlen der Ostwald-Reifung auf. In diesem Fall kann die Größeneinstellung der Nanoteilchen über die Kontrolle des Verhältnisses zwischen den Nukleations- und Wachstumsraten erzielt werden. Dies ist der erste Versuch einer systematischen experimentellen Studie der "heißen" organometallische Synthese der Metallnanoteilchen und des Mechanismus der homogen Nukleation der Metalllegierungsnanoteilchen. Die experimentellen Ergebnisse zeigen an, daß zunächst entstehende Cluster des Übergangsmetalls eine große Rolle für das Wachstum der Legierung spielen. Die Entstehung dieser Cluster ist der reaktionsbestimmende Schritt für den vollständigen Nukleationsprozeß, weil die Konzentrationen des Platins oder des Palladiums nicht die Nukleationsrate beeinflussen.

Die Entwicklung einer wirkungsvollen Methode zur exakten Kontrolle der Größe der  $CoPt_3$  Nanoteilchen erlaubte die Untersuchung ihrer größenabhängigen magnetischen Eigenschaften. Die magnetischen Messungen (Hystereseschleifen und ZFC/FC Untersuchungen) deckten ein superparamagnetisches Verhalten dieser magnetischen Legierungsnanoteilchen auf. Die Übergangstemperatur zwischen dem ferromagnetischen und

superparamagnetischen Verhalten, Koerzitivfeldstärke und Sättigungsmagnetisierung hängen stark von der Größe der Nanoteilchen ab.

Die monodispersen magnetischen Legierungsnanoteilchen können in ein-, zwei- und dreidimensionale Überstrukturen organisiert werden. Mischungen von Nanoteilchen unterschiedlicher Größe in einem passenden Größen- und Mengenverhältnis führen zur Anordnung in Mischsupergittern mit hohen Packungsdichten. Kristallisation der monodispersen magnetischen Legierungsnanoteilchen in geordnete dreidimensionale Übergitter wird durch kontrollierbare Entstabilisierung der Toluollösung von Nanoteilchen erreicht. Tadellos facettierte makroskopische ( $\sim 20 - 30$  nm) kolloidale Kristalle der magnetischen Legierungsnanoteilchen (CoPt<sub>3</sub> und PtFe) sind zum ersten Mal dargestellt worden. HRSEM-Untersuchungen zeigte eine langreichweitige Ordnung (ca.  $10 \mu\text{m}$ ) der Nanokristalle. Ein angelegtes magnetisches Feld hat einen starken Einfluß auf die Anordnung der magnetischen Nanokristalle in 2D oder in 3D Überstrukturen. Hierdurch konnten neue Überstrukturen der magnetischen Nanoteilchen dargestellt werden. Durch Anlegen eines parallelen externen magnetischen Feldes ordnen sich die CoPt<sub>3</sub> Nanoteilchen in periodischen Konzentrationsstreifen an. Wird das externe magnetische Feld senkrecht zu dem Substrat angelegt, bilden sich nadelförmige Überstrukturen der Nanoteilchen. Während bei verhältnismäßig starker magnetischer Feldstärke ( $\sim 0.1 - 1$  Tesla) nur eine kurzreichweitige Ordnung der Nanokristalle beobachtet wird, bilden sich im schwachen magnetischen Feld ( $\sim 0.01 - 0,02$  Tesla) kolloidale „Superkristalle“.